
Electronic Thesis and Dissertation Repository

7-7-2016 12:00 AM

Quantitative PET-CT Perfusion Imaging of Prostate Cancer

Adam R. Blais

The University of Western Ontario

Supervisor

Ting-Yim Lee

The University of Western Ontario

Graduate Program in Medical Biophysics

A thesis submitted in partial fulfillment of the requirements for the degree in Doctor of Philosophy

© Adam R. Blais 2016

Follow this and additional works at: <https://ir.lib.uwo.ca/etd>



Part of the [Medical Biophysics Commons](#)

Recommended Citation

Blais, Adam R., "Quantitative PET-CT Perfusion Imaging of Prostate Cancer" (2016). *Electronic Thesis and Dissertation Repository*. 3874.

<https://ir.lib.uwo.ca/etd/3874>

This Dissertation/Thesis is brought to you for free and open access by Scholarship@Western. It has been accepted for inclusion in Electronic Thesis and Dissertation Repository by an authorized administrator of Scholarship@Western. For more information, please contact wlsadmin@uwo.ca.

Abstract

Functional imaging of ^{18}F -Fluorocholine PET holds promise for the detection of dominant prostatic lesions. Quantitative parameters from PET-CT Perfusion may be capable of measuring choline kinase activity, which could assist in identification of the dominant prostatic lesion for more accurate targeting of biopsies and radiation dose escalation.

The objectives of this thesis are: 1) investigate the feasibility of using venous TACs in quantitative graphical analysis, and 2) develop and test a quantitative PET-CT Perfusion imaging technique that shows promise for identifying dominant prostatic lesions.

Chapter 2 describes the effect of venous dispersion on distribution volume measurements with the Logan Plot. The dispersion of venous PET curves was simulated based on the arterio-venous transit time spectrum measured in a perfusion CT study of the human forearm. The analysis showed good agreement between distribution volume measurements produced by the arterial and venous TACs.

Chapter 3 details the mathematical implementation of a linearized solution of the 3-Compartment kinetic model for hybrid PET-CT Perfusion imaging. A noise simulation determined the effect of incorporating CT perfusion parameters into the PET model on the accuracy and variability of measurements of the choline kinase activity. Results indicated that inclusion of CT perfusion parameters known a priori can significantly improve the accuracy and variability of imaging parameters measured with PET.

Chapter 4 presents the implementation of PET-CT Perfusion imaging in a xenograft mouse model of human prostate cancer. Image-derived arterial TACs from the left ventricle were

corrected for partial volume and spillover effects and validated by comparing to blood sampled curves. The PET-CT Perfusion imaging technique produced parametric maps of the choline kinase activity, k_3 . The results showed that the partial volume and spillover corrected arterial TACs agreed well with the blood sampled curves, and that $k_{3\max}$ was significantly correlated with tumor volume, while SUV was not.

In summary, this thesis establishes a solid foundation for future clinical research into ^{18}F -fluorocholine PET imaging for the identification of dominant prostatic lesions. Quantitative PET-CT Perfusion imaging shows promise for assisting targeting of biopsy and radiation dose escalation of prostate cancer.

Keywords

Positron emission tomography, kinetic modeling, fluorocholine, Logan plot, graphical analysis, choline kinase, dispersion correction, prostate cancer, functional imaging, CT perfusion, binding rate constant, phosphorylation

Co-Authorship Statement

The contents of Chapter 2 are adapted from an original research manuscript entitled “Simulating the effect of venous dispersion on distribution volume measurements from the Logan plot” published in *Biomedical Physics and Engineering Express*, 2015, 1(4) by A.R. Blais and T.Y. Lee. T.Y. Lee and I were responsible for study design, data collection and analysis, and writing the manuscript.

The contents of Chapter 3 are adapted from an original research manuscript entitled “Noise Study of Linear and Non-Linear Solutions of a DCE-CT/PET Hybrid Imaging Technique” submitted to *Physics in Medicine and Biology* by A.R. Blais and T.Y. Lee. T.Y. Lee and I were responsible for study design, data collection and analysis, and writing the manuscript.

The contents of Chapter 4 are adapted from an original research manuscript entitled “A quantitative hybrid PET-CT Perfusion technique for measuring the binding rate constant of ^{18}F -Fluorocholine in a mouse model of prostate cancer” submitted to *Physics in Medicine and Biology*, by A.R. Blais, C. Crukley, M. Gaed, J. Hadway, L. Keenlside, J. Valliant, G. Bauman and T.Y. Lee. T.Y. Lee and I were responsible for study design, data collection and analysis, and writing the manuscript. C. Crukley performed the immunohistochemistry staining. M. Gaed scored the immunohistochemistry samples. J. Hadway was the veterinary technician responsible for anesthetization of mice prior to the imaging studies and the excision of tumors from mice. L. Keenlside constructed the mouse heart phantom with the 3D printer. J. Valliant oversaw synthesis of the ^{18}F -fluorocholine tracer for the PET imaging study. G. Bauman assisted with manuscript revision.

Acknowledgments

First and foremost, I would like to acknowledge my thesis supervisor, Dr. Ting-Yim Lee. His seemingly endless knowledge of CT Perfusion, PET, and tracer kinetics analysis never ceases to amaze me. Throughout my training, he has taught me to interpret results with cautious optimism and to consider alternate explanations for any given result. He has always afforded me a great deal of independence while subtly guiding me in the most logical direction. It has been a great privilege to work with someone so passionate and dedicated to their field, and the lessons that I have learned from him will no doubt serve me quite well in my future endeavors. For that, I am extremely grateful.

Furthermore, I wish to thank my thesis committee members, Dr. Glenn Bauman and Dr. Len Luyt. These individuals provided me with very valuable advice and guidance throughout the course of my training. Dr. Bauman contributed a valuable clinical perspective and his expertise and leadership abilities have been a very positive influence. Dr. Luyt's profound chemistry expertise was a crucial contribution to the evolution of my work.

I would like to express deep gratitude to Jennifer Hadway. My experiments would not have been possible without her. Her tireless work ethic ensured that any task related to my experiments was completed with the utmost care. She was incredibly generous with her time and was always available to me whenever I needed assistance or had questions in the lab. I would also like to thank Lise Desjardins and Laura Morrison for helping out with experiments. Many thanks go out to Lynn Keenlside for constructing a mouse heart phantom on the 3D printer.

I owe a great deal to the members of the Lee lab for providing valuable insight and discussion over the past several years. Dr. Xiaogang Chen's programming expertise was essential. Thanks to Mark Dekaban for all of the valuable discussions and guidance pertaining to kinetic modeling. Dr. Aaron So and Dr. Errol Stewart contributed very valuable feedback during journal clubs and whenever I had to practice a seminar or conference talk. There are too many others to name here. Thanks to all the Lee lab members for the insightful discussions and for making my time at Robarts enjoyable.

I am indebted to Cathie Crukley, Mena Gaed and the staff of the Pathology Core Lab at Robarts. Cathie and Mena generously donated their time to help with the histology processing and immunohistochemistry analysis.

I wish to thank other Robarts members, past and present, for their help – to Dr. Eli Gibson for showing me the ins and outs of image registration with 3D Slicer, and to Kathryn Manning for the many much-needed lunch/sushi breaks.

I would like to express sincere appreciation to Anne Leaist. Anne was an invaluable resource for all administrative matters. Whether it was printing large documents, submitting conference expenses, stipend issues, or providing afternoon snacks, Anne has been instrumental in the smooth running of the lab. Her care, support and engaging discussions enabled me to focus on my work and prevented me from having to worry about a wide variety of problems.

Thanks are in order to Dr. Jerry Batista and Dr. Rob Stodilka for helping me navigate the intricacies of the CAMPEP program and for providing valuable feedback and preparation for my future endeavors. A big thank you to Wendy Hough for all of the help she provided during my time in the Medical Biophysics program.

I wish to express heartfelt gratitude to my parents Diane & Richard, whose unconditional love and constant support have been essential throughout my graduate studies.

Finally, thank you to my fiancée, Bethany, for her love and support, and for always managing to put a smile on my face when I came home from the lab. Most importantly, I thank her for her patience in dealing with a wide variety of my moods over the last couple of years.

Table of Contents

Abstract	i
Co-Authorship Statement.....	iii
Acknowledgments.....	iv
Table of Contents	vii
List of Tables	xiii
List of Figures	xv
List of Appendices	xix
List of Abbreviations	xx
Epigraph.....	xxii
Chapter 1	1
1 Introduction.....	1
1.1 Prostate Cancer	1
1.1.1 Prevalence	1
1.1.2 Potential Causes	1
1.1.3 Mechanisms	1
1.2 Anatomy of the Prostate.....	2
1.2.1 Zonal Anatomy	3
1.3 Prostate Cancer Screening	4
1.3.1 Digital Rectal Examination.....	4
1.3.2 Prostate Specific Antigen Screening.....	5
1.3.3 Staging: Gleason Grading System	6

1.3.4	Trans-Rectal Ultrasound-Guided Biopsy.....	8
1.4	Prostate Cancer Management	9
1.4.1	Active Surveillance.....	9
1.4.2	Androgen Deprivation Therapy	10
1.4.3	Chemotherapy	10
1.4.4	Radiation Therapy.....	11
1.5	Medical Imaging of Prostate Cancer.....	12
1.5.1	Multi-Parametric MRI	13
1.5.2	Ultrasound Imaging	14
1.5.3	Computed Tomography Imaging.....	15
1.5.4	Positron Emission Tomography.....	20
1.6	Animal Models of Prostate Cancer	21
1.6.1	Transgenic Mouse Model	21
1.6.2	Xenograft Mouse Model.....	22
1.6.3	Rat & Canine Models.....	23
1.7	Imaging of Choline Metabolism	23
1.7.1	The Kennedy Pathway	23
1.7.2	¹⁸ F-Fluorocholine PET Imaging	24
1.8	Quantitative Analysis of PET	25
1.8.1	Standardized Uptake Value.....	25
1.8.2	Kinetics Modeling.....	28
1.8.3	Graphical Analysis.....	32
1.8.4	Kinetics Modeling of FCH PET: Motivation.....	34

1.9 Objectives and Outline.....	36
1.9.1 Hypothesis.....	36
1.9.2 Research Objectives.....	37
1.10References.....	38
Chapter 2.....	51
2 Simulating the effect of venous dispersion on distribution volume measurements from the Logan Plot	51
2.1 Introduction.....	51
2.2 Methods.....	53
2.2.1 Tissue Curve Simulation.....	53
2.2.2 Simulation of Venous Dispersion	56
2.2.3 Digital Phantom	59
2.2.4 Logan Graphical Analysis.....	63
2.2.5 Statistical Analysis.....	64
2.3 Results.....	64
2.3.1 Simulated Venous Curves.....	64
2.3.2 Arterial and Venous Logan Analyses	66
2.4 Discussion.....	71
2.5 Conclusions.....	75
2.6 References.....	76
Chapter 3.....	79
3 Noise Study of Linear and Non-Linear Solutions of a DCE-CT/PET Hybrid Imaging Technique.....	79

3.1	Introduction.....	79
3.2	Methods.....	82
3.2.1	Generation of Simulated Tissue Time Activity Curves.....	82
3.2.2	Linear Solutions of 3-Compartment Model.....	85
3.2.3	Non-Linear Solutions of 3-Compartment Model.....	88
3.2.4	Sensitivity Analysis	89
3.2.5	Identifiability Analysis.....	91
3.2.6	Simulating PET Frames	93
3.2.7	Effect of Omitting Blood Volume Term.....	94
3.2.8	Simulating Noise of Time Activity Curves	94
3.2.9	Linearity of k_3 Estimates.....	95
3.2.10	Effect of Bias in a priori K_1 and k_2	96
3.2.11	Parameter Accuracy and Best Fit.....	97
3.3	Results.....	98
3.3.1	Sensitivity	98
3.3.2	CT Noise Simulation.....	99
3.3.3	k_3 Linearity	99
3.3.4	Model Selection	101
3.3.5	Effect of Omitting Blood Volume Term.....	101
3.3.6	k_3 Accuracy and Variability.....	102
3.4	Discussion	105
3.5	Conclusions.....	110
3.6	Acknowledgments.....	110

3.7 References.....	111
Chapter 4.....	114
4 A quantitative hybrid PET-CT Perfusion technique for measuring the binding rate constant of ^{18}F -Fluorocholine in a mouse model of prostate cancer.....	114
4.1 Introduction.....	114
4.2 Methods.....	116
4.2.1 Mouse Model	116
4.2.2 PET Imaging Protocol.....	116
4.2.3 CT Perfusion Scanning Protocol.....	117
4.2.4 Partial Volume & Spillover Correction of Image-Derived PET TACs ..	118
4.2.5 Dispersion Correction	125
4.2.6 Validation of Partial Volume and Spillover Correction	127
4.2.7 Metabolite and Plasma Fraction Correction	128
4.2.8 Image Registration	128
4.2.9 Kinetic Model	129
4.2.10 Parametric Maps	132
4.2.11 Preliminary Immunohistochemistry.....	134
4.2.12 Statistical Analysis.....	134
4.3 Results.....	135
4.3.1 Validation of Partial Volume and Spillover Correction	135
4.3.2 Selecting the Best Model	140
4.3.3 Parametric Maps	141
4.3.4 Tumor Volume Correlation.....	144

4.3.5 Immunohistochemistry	145
4.4 Discussion	147
4.5 Conclusions.....	154
4.6 References.....	155
Chapter 5.....	159
5 Conclusions and Future Work.....	159
5.1 Summary	159
5.2 Venous TACs for the Logan Plot.....	159
5.3 Robust Measurement of the Binding Rate Constant.....	161
5.4 Hybrid PET-CTP Imaging for Prostate Cancer	161
5.5 Future Work	162
5.5.1 Mean Transit Time in Compartment Models.....	162
5.5.2 Choline Kinase Expression in Prostate Cancer.....	163
5.5.3 Effect of <i>In Vivo</i> Signal to Noise Ratio on k_3	164
5.5.4 Correlation of k_3 from <i>In Vivo</i> PET-CTP with Histopathology.....	165
5.5.5 Clinical Applications	166
5.6 References	167
Appendix A: Coefficients in the 3-Compartment Model	169
Appendix B: Partial Derivatives of $Q(t)$	170
Appendix C: Animal Ethics Approval.....	173
Appendix D: Copyright Agreements	174
Curriculum Vitae	180

List of Tables

Table 2.1: Description of the parameters and parameter values used in the 3-compartment, digital phantom simulation in order to produce simulated tissue TACs.....	56
Table 2.2: Mean percent differences for the Logan distribution volume measurements, shown as mean percent difference (SD) in %. For noisy cases, the difference was calculated as the mean percentage difference over all 100 runs of each parameter set. Values in this table represent the mean of the 343 (7 x 49) individual parameter set differences.	69
Table 3.1: Parameters obtained from fitting of mean ROI TAC in a PC-3 mouse tumour.	85
Table 3.2: Linearized solutions of the 3-Compartment model assuming zero blood volume. Some models assume known parameters from CT Perfusion functional maps. Coefficients of the linearized solutions were solved for using a non-negative least squares algorithm in Matlab and rate constants were calculated from the coefficients. Constraints were used to prevent negative rate constants.	87
Table 3.3: Initial parameter sets and constraints used for the non-linear fitting of the tissue TACs.	89
Table 3.4: Correlation matrix for the 3-Compartment model. Highly correlated parameters are in bold. Values in the upper right triangular region are omitted given that it is a symmetric matrix.	99
Table 3.5: Parameter estimates as well as Akaike information criterion for small samples sizes (AICc) and Akaike weights for the different models in the noiseless case. These data show the effect of frame averaging on the model fitting. The 3C-K1k2 and 3C-LIN-K1k2 solutions had the highest probability of producing the best fit because their SSD's were	

similar to other model solutions and they use the least number of parameters. (SSD = sum of squared deviations between the fit and the tissue TAC)	101
Table 4.1: Linearized solutions of the 3-Compartment kinetic model.	130

List of Figures

Figure 1.1: Zonal anatomy of the prostate. (Reproduced with permission [18]).....	4
Figure 1.2: Standard drawing illustrating different Gleason grades. (Reprinted by permission from Macmillan Publishers Ltd: Modern Pathology [37], copyright (2004).).	7
Figure 1.3: Johnson and Wilson model for solute exchange between capillaries and the interstitial space. Symbols are defined in the text.....	18
Figure 1.4: The blood-flow scaled impulse residue function based on the Johnson and Wilson model. Symbols are defined in the text.	19
Figure 1.5: ATP-dependent phosphorylation of choline by choline kinase.....	24
Figure 1.6: Sample TAC's from two different regions with different kinetics.	27
Figure 1.7: The 2-compartment model for an inert solute. Symbols defined in text.	29
Figure 1.8: 3-Compartment model for metabolized tracers.....	31
Figure 2.1: Kinetic model used to produce the simulated tissue curves. Tracer flows from the arterial end to the venous end of the capillaries and leaks by passive diffusion into the interstitial space of tissue and then exchange with the tissue bound pool.	54
Figure 2.2: Digital phantom used to produce tissue TACs.	62
Figure 2.3: a) Measured radial artery along with measured and fitted median cubital vein TDCs from the DCE-CT forearm study. Curves were smoothed using a moving average filter. b) Measured FCH PET arterial TAC from the iliac artery along with simulated venous curves for PET tracers of 157.6 and 18 Daltons.....	65
Figure 2.4: Results for $k_4 = 0.05 \text{ min}^{-1}$ and $E_{av} = 8.4\%$ (FCH) noiseless case. The first two rows show maps of the V_d 's calculated for the arterial (A) and venous (V) methods as well	

as the true V_d values in ml/g. The blood flow F is in ml/min/g and the vascular mean transit time MTT is in seconds.....	67
Figure 2.5: Results for the $k_4 = 0.05 \text{ min}^{-1}$ and $E = 8.4\%$ (FCH) noise case, with $\langle f_N^Q \rangle_{N,t} = 0.19$. Setup is the same as in Figure 2.4.	68
Figure 2.6: Noiseless case. (top) Linear regressions for the a) $k_4 = 0.05 \text{ min}^{-1}$, b) $k_4 = 0.1 \text{ min}^{-1}$ and c) $k_4 = 0.3 \text{ min}^{-1}$, $E = 8.4\%$ (FCH). (Bottom) Bland-Altman analyses, plotting % difference vs. average between V_d 's calculated with both methods for d) $k_4 = 0.05 \text{ min}^{-1}$, e) $k_4 = 0.1 \text{ min}^{-1}$ and f) $k_4 = 0.3 \text{ min}^{-1}$	70
Figure 2.7: Noisy case, with $\langle f_N^Q \rangle_{N,t}$ equal to 0.19. (Top) Linear regressions for the a) $k_4 = 0.05 \text{ min}^{-1}$, b) $k_4 = 0.1 \text{ min}^{-1}$ and c) $k_4 = 0.3 \text{ min}^{-1}$. (Bottom) Bland-Altman analyses, plotting % difference vs. average between V_d 's calculated with both methods for d) $k_4 = 0.05 \text{ min}^{-1}$, e) $k_4 = 0.1 \text{ min}^{-1}$ and f) $k_4 = 0.3 \text{ min}^{-1}$, noisy cases.	71
Figure 3.1: The 3-Compartment kinetic model of tracer uptake in tissue.	84
Figure 3.2: Fit of the tumour tissue TAC of a PC-3 mouse model to obtain parameters for the simulated TACs.....	85
Figure 3.3: Instantaneous and simulated averaged arterial TACs. The full acquisition duration (3,600 s) is shown on the left, and an expanded time scale (0-500s) is shown on the right. This frame averaging schedule was also applied to the tissue TAC.	94
Figure 3.4: Normalized sensitivity curve calculated for each parameter of the 3-Compartment model as a function of time.....	98

Figure 3.5: Estimated vs. true k_3 for all the model solutions. (Left) No error in K_1 and k_2 . (Right) K_1 and k_2 with simulated bias. (Top) SNR = 20, (Middle) SNR = 10, (Bottom) SNR = 4.	100
Figure 3.6: k_3 estimates produced by the 3C-LIN model solution (with no V_b term) for different values of V_b	102
Figure 3.7: The coefficients of variation of model parameters with TAC SNR = 4 calculated using the covariance matrix represent the Cramér-Rao Bound.	103
Figure 3.8: k_3 estimates (top row), $\text{bias}^2 + \text{variance}$ (middle row), and COV (bottom row) for 250 noise runs with no K_1 and k_2 error (left column), and simulated error (right column). Error bars represent standard deviation.	104
Figure 3.9: (Top) Example of impulse residue functions (IRF) of the Johnson-Wilson (J-W) and 3-compartment models.	108
Figure 4.1: (Top) Cross-Section of the mouse heart phantom (not to scale, to emphasize the LV and myocardium chambers).	120
Figure 4.2: Axial slice of a mouse phantom PET scan with the myocardium chamber filled with FDG..	123
Figure 4.3: Registered images of the LV and myocardium phantom scans..	124
Figure 4.4: The 3-compartment kinetic model for uptake of ^{18}F -FCH in tissue.	132
Figure 4.5: (Top) Blood counter TAC in response to a step change in activity measured at withdrawal speeds of 10 and 50 $\mu\text{l}/\text{min}$ along with the fitted exponential curves.	137
Figure 4.6: (Top) Blood-sampled arterial TAC at 10 $\mu\text{l}/\text{min}$ and dispersion corrected TAC for one mouse study.	139

Figure 4.7: Example of image-derived, partial volume and spillover corrected arterial TAC from LV and dispersion corrected blood sampled arterial TAC from one tail artery at 10 μ l/min.....	139
Figure 4.8: Image-derived PVSC TAC obtained using fitted values of α and β	140
Figure 4.9: Model fits of a mean tumor ROI TAC from a PC-3 hybrid PET-CTP study, produced by both linearized model solutions.	141
Figure 4.10: CT Perfusion functional maps of a PC-3 tumor at days 64, 69 and 94 post implantation.	142
Figure 4.11: Maps showing SUV ₆₀ and the distribution volume (V_d) from the Logan Plot analysis.....	143
Figure 4.12: PET parametric maps of the same PC-3 mouse tumor as Figure 4.10 and Figure 4.11 at days 64, 69 and 94.	144
Figure 4.13: a) Plot of k_{3max} vs. tumor volume..	145
Figure 4.14: Histological results compared to k_3 paramtric maps.....	146
Figure 4.15: The progression of blood flow through PE10 tubing in the blood counter insert.....	149
Figure 4.16: Effect of varying the k_3 parameter on the tissue TACs.....	151
Figure 4.17: (Top) Impulse residue functions for the Johnson-Wilson and compartment models.....	152

List of Appendices

Appendix A: Coefficients in the 3-Compartment Model	169
Appendix B: Partial Derivatives of $Q(t)$	170
Appendix C: Animal Ethics Approval for the work contained in Chapter 4 entitled “A quantitative hybrid PET-CT Perfusion technique for measuring the binding rate constant of ^{18}F -Fluorocholine in a mouse model of prostate cancer”	173
Appendix D: Copyright Agreements	174

List of Abbreviations

3C-LIN	3-Compartment Linear
3C-LIN-K1	3-Compartment Linear with K_1 from CT Perfusion
3C-LIN-K1k2	3-Compartment Linear with K_1 and k_2 from CT Perfusion
ADP	Adenosine diphosphate
ADT	Androgen deprivation therapy
ATP	Adenosine triphosphate
AV	Active surveillance
BF	Blood flow
BPH	Benign prostatic hyperplasia
BV (or V_b)	Blood volume
ChK α	Choline Kinase α
CK	Choline kinase
CT	Computed Tomography
CTP	CT Perfusion
DCE-CT	Dynamic contrast-enhanced CT
DRE	Digital rectal examination
DWI	Diffusion-weighted imaging
FCH	^{18}F -Fluorocholine
FDG	^{18}F -Fluorodeoxyglucose
H&E	Hematoxylin & eosin

HDR	High dose rate
LDR	Low dose rate
mp-MRI	Multi-parametric MRI
MRI	Magnetic resonance imaging
MRS	Magnetic resonance spectroscopy
NCCN	National Comprehensive Cancer Network
PC	Phosphocholine
PCa	Prostate Cancer
PET	Positron emission tomography
PS	Permeability-surface area product
PSA	Prostate specific antigen
PVSC	Partial volume and spillover corrected
ROI	Region of interest
SUV	Standardized uptake value
T2W	T2-weighted
TRUS-GBS	Trans-rectal ultrasound-guided biopsy

Epigraph

“The truth is more magical - in the best and most exciting sense of the word - than any myth or made-up mystery or miracle. Science has its own magic: the magic of reality.”

- Richard Dawkins

Chapter 1

1 Introduction

1.1 Prostate Cancer

1.1.1 Prevalence

Approximately 1 in 7 Canadian men will develop prostate cancer and 1 in 27 men will die from the disease. Prostate cancer is the most common cancer in Canadian men and accounts for 23.9% of new cancer cases in Canada. [1] On average, 66 men will be diagnosed with prostate cancer every day and 11 men will die from prostate cancer every day. It is estimated that there were 24,000 new cases and 4,100 deaths caused by the disease in 2015. [1]

1.1.2 Potential Causes

Causes of prostate cancer are complex and multifactorial. The data regarding the causes of prostate cancer are not conclusive, however there have been some indications from epidemiological studies that the typical Western diet may play a role. [2-4] Specifically, high calcium, high fat diets as well as dairy products and red and processed meats have emerged as potential causative factors in epidemiological studies. [5] In addition to dietary factors, lifestyle factors such as exercise may also play a role. [6]

1.1.3 Mechanisms

Healthy prostate tissue and androgen-dependent prostate cancer depend on androgen hormones such as testosterone as regulators of growth and proliferation. [7]

Androgen-dependent prostate cancer depends on androgen receptors for growth and survival. [8] After crossing the cell membrane, testosterone is converted by the enzyme 5α -reductase to dihydrotestosterone, an active hormone with a 5 to 10 fold increased affinity for the androgen receptor. Dihydrotestosterone binds to androgen receptors in the cytoplasm before translocating into the nucleus where it binds to androgen-response elements in the DNA, leading to activation of genes that mediate cell growth and survival. [7]

Androgen-independent prostate cancer is less dependent on the presence of androgen because it develops alternate cellular pathways to compensate for an androgen-depleted environment. Alternatively, cancer cells may develop a pathway that is hypersensitive to androgen and use these low levels of androgen for growth. [9-11] This type of cancer is castration resistant.

Chromosomal alterations and the altered expression of oncogenes have been identified as other potential factors that contribute to the development of prostate cancer. [12]

1.2 Anatomy of the Prostate

The prostate is a gland that secretes seminal fluid and expels it via the urethra during ejaculation. The base of the prostate is located at the neck of the bladder and its apex is found at the urogenital diaphragm. [13, 14] The prostate is situated anterior to the rectum, with a thin layer of connective tissue known as Denonvilliers' fascia separating it from the latter. [13] There are skeletal muscle fibres that extend from the urogenital diaphragm into the apex of the prostate and terminate at the anterior mid-prostate. [15] The entire prostate

gland is covered in a layer of connective tissue called the prostatic capsule. The anterior fibromuscular stroma forms the external surface of the anterior prostate, contributing to its convex shape. [13]

1.2.1 Zonal Anatomy

McNeal was the first to characterize the prostate into distinct zones. [16] (Figure 1.1) The peripheral zone contains 75% of the glandular tissue in the prostate. It includes all of the glandular tissue near the apex and runs superiorly along the capsule to encompass all of the tissue at the apex. This zone has shown to have a higher prevalence of post-inflammatory atrophy, chronic prostatitis and carcinoma. [13]

The central zone is a cone-shaped zone that runs from the apex at the concurrence of the ejaculatory ducts to the prostatic urethra at the mid-prostate. Contrary to the peripheral zone, carcinoma rarely develops in the central zone. [17]

The transition zone is located laterally to the urethra at the midgland. This zone is the main site of development of benign prostatic hyperplasia (BPH) and less frequently it can also develop adenocarcinoma. [13]

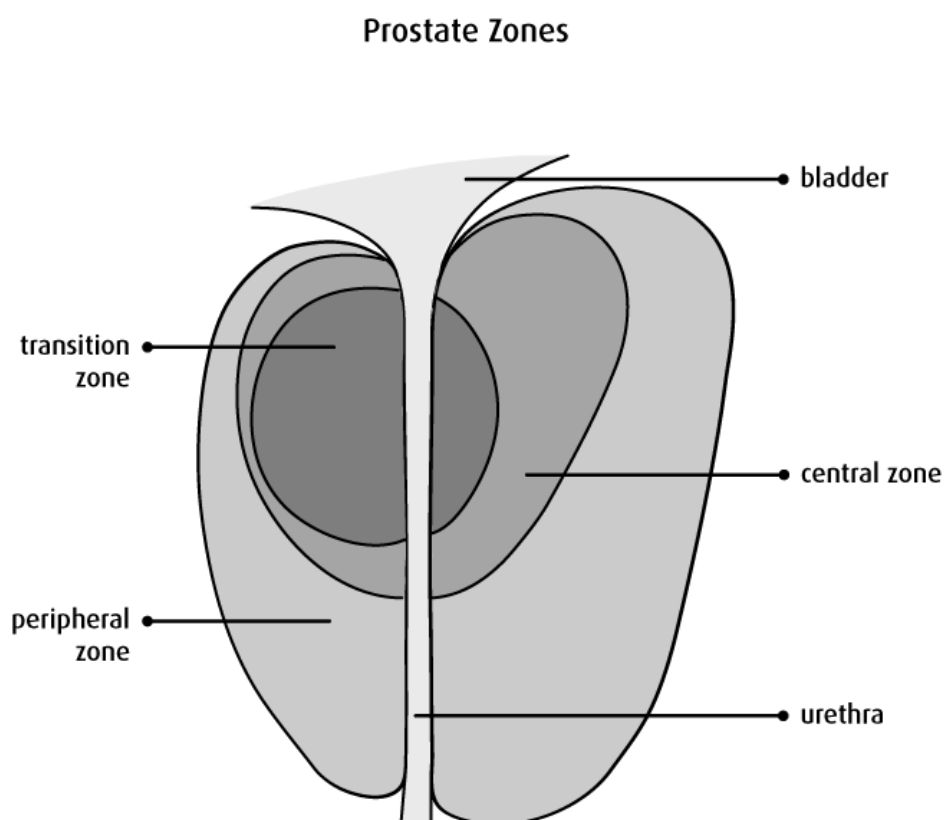


Figure 1.1: Zonal anatomy of the prostate. (Reproduced with permission [18])

1.3 Prostate Cancer Screening

1.3.1 Digital Rectal Examination

Digital Rectal Examination (DRE) is an exam in which the physician palpates the prostate gland via the rectum to determine whether any abnormal enlargement of the gland is present. The efficacy of DRE for the detection of prostate cancer is generally poor, with a positive predictive value ranging between 17-38%, depending on the age of the patient, since older patients are more likely to present with advanced disease. [19]

The DRE can often be confounded by the presence benign prostatic hyperplasia (BPH), an enlargement of the gland that worsens with age. It is generally not recommended

to screen for prostate cancer with DRE alone, as it has been found that DRE has no effect on morbidity or mortality in men with prostate cancer. [20] Indeed, only pathologically advanced cancers can be detected by DRE alone. [21]

1.3.2 Prostate Specific Antigen Screening

Prostate specific antigen (PSA) is a glycoprotein secreted by the epithelial cells of the prostate. PSA levels are often elevated in individuals with prostate cancer, since malignant tissue exhibits increased PSA production and the tortuous nature of cancerous cells results in disruptions to the barrier between the capillaries and prostate lumen, resulting in increased release of PSA into the serum.

Studies estimate that PSA levels can be elevated as much as 5 to 10 years prior to diagnosis of prostate cancer [22, 23] and perhaps even longer. [24] Unfortunately, high PSA levels may also be due to asymptomatic inflammation [25, 26] or bacterial prostatitis. [27] BPH is a confounder as well, since its presence is also associated with elevated PSA levels. [26] PSA levels are also influenced by urinary retention, ejaculation, DRE, and trans-rectal ultrasound-guided biopsy. [28, 29]

The traditional cut-off for PSA screening is a PSA level of greater than 4.0 ng/ml. [30-33] The majority of prostate cancer cases in the range of 4.0 to 10.0 ng/ml are organ-confined and potentially curable cases, while the proportion of organ-confined cases is less than 50% at levels higher than 10.0 ng/ml. [34] The positive predictive value for PSA levels greater than 4.0 ng/ml is only 30%, signifying that less than a third of patients with positive PSA screening will truly have the disease.

The advent of PSA testing has resulted in an increased detection of prostate cancer with stage migration towards lower stage disease. This has greatly increased the risk of over-diagnosis and over-treatment of low-risk patients. These factors have led a recent review to conclude that the risks of PSA screening outweigh the benefits. [35]

1.3.3 Staging: Gleason Grading System

In 1966, Gleason [36] proposed a classification system that assigns a grade to histopathological prostate specimens with the goal of stratifying prostatic carcinoma according to varying degrees of malignancy. The system relies on visual assessment of general histologic patterns observed in H&E stained sections rather than any specific criteria. [37] It is widely recognized that the grade of a tumour is related to its degree of malignancy. [38]

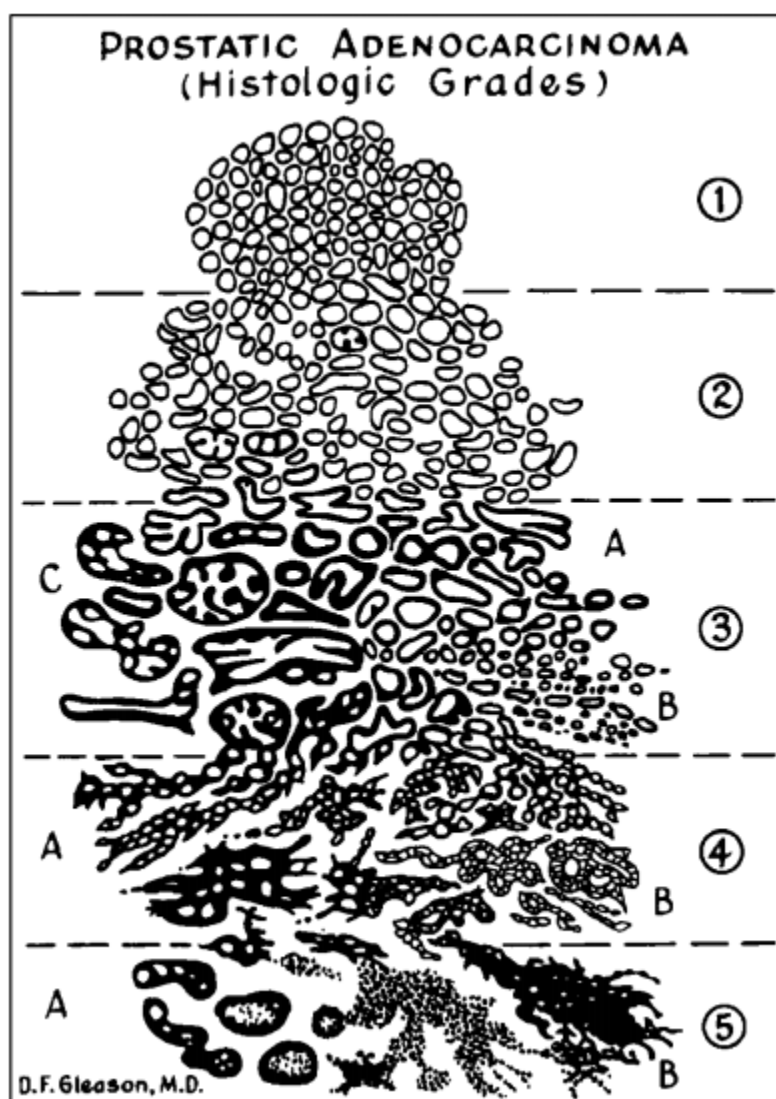


Figure 1.2: Standard drawing illustrating different Gleason grades. (Reprinted by permission from Macmillan Publishers Ltd: Modern Pathology [37], copyright (2004).)

The lowest Gleason grade is 2 and the highest is 10. The Gleason grade is the sum of two individual scores ranging from 1 to 5. The individual scores are used to classify any of the nine different patterns (consolidated into 5 scores) that are seen in prostate histology

specimens. Scores are assigned to the primary pattern, which is the predominant pattern seen throughout a lesion, and the secondary pattern, which is the second most common pattern in the lesion. To achieve a Gleason grade, the scores from the primary and secondary patterns are summed. If only one pattern is present, that pattern is assigned a score and multiplied by two to achieve the Gleason grade. A Gleason score of 3 represents discrete, well-formed, infiltrative glands. A score of 5 indicates very poorly differentiated glands with high potential for proliferation. A Gleason grade of 2-4 is not a candidate for intervention, because in many cases these tumours are actually benign prostatic hyperplasia and classification of these grades has shown poor reproducibility among experts. [39, 40] Higher Gleason grade may be candidates for either active surveillance or treatment.

1.3.4 Trans-Rectal Ultrasound-Guided Biopsy

Transrectal ultrasound guided biopsy (TRUS-GBS) of the prostate is used to diagnose prostate cancer (PCa). Focal disease is challenging to detect with medical imaging and with ultrasound in particular. Many types of prostate cancer are not visible on grayscale ultrasound and other detectable lesions are benign in nature. Further, TRUS has a number of potential side effects, including hematuria, hemorrhage and infection. [41] Despite these disadvantages, TRUS-GBS remains in widespread use due to its low cost, simplicity and high quality images. TRUS-GBS targets broad sectors of the prostate rather than specific localized lesions. In recent years, there has been a trend toward acquiring a larger number of biopsy specimens with some studies recommending up to 12 individual biopsy cores. [42] This “random biopsy” approach has been shown to miss 35% of cancers on first attempt and it also underestimates Gleason grade in 46% of cases. [43, 44] In these cases,

repeat biopsies must be performed if a diagnosis is to be made, which adds to the patient's psychological stress and discomfort, and postpones diagnosis and treatment. [45]

In addition, TRUS-GBS has difficulty detecting anterior prostate tumours until they grow to within 15-20mm of the posterior margin. [46] This causes delayed diagnosis of the disease. Hence, there is substantial motivation to develop an imaging technique with good sensitivity and specificity that could overcome these issues and aid targeting for TRUS-GBS.

1.4 Prostate Cancer Management

Management options for prostate cancer include active surveillance, androgen deprivation therapy, brachytherapy, chemotherapy and external beam radiation therapy.

1.4.1 Active Surveillance

Active surveillance (AS) is a management strategy for low-risk prostate cancer in routine surveillance and is implemented with the purpose of identifying any significant progression in the cancer that may be clinically significant. [47] The use of AS for indolent tumours helps to reduce the prevalence of overtreatment and over-diagnosis, sparing the patient from potentially unnecessary side effects and risks as a result of treatment. Guidelines established by the National Comprehensive Cancer Network (NCCN) state that AS is suitable for prostate cancer with Gleason score ≤ 6 , PSA ≤ 10 ng/ml, fewer than three positive biopsy cores, less than 50% cancer in any core, and life expectancy ≥ 20 years. [47]

1.4.2 Androgen Deprivation Therapy

Androgen-dependent prostate cancer requires the presence of androgen hormones such as testosterone in order to grow. Androgen deprivation therapy (ADT) is an anti-hormonal therapy that functions to block the ability of prostate cells to benefit from androgen hormones.

Testosterone is synthesized in the testicles. The simplest, most cost-effective and most radical method to prevent synthesis of testosterone is to surgically remove the testicles in a procedure known as an orchiectomy. However, the most common method of ADT employs chemical means and can achieve the effect of castration without the use of surgery.

Chemical ADT can be delivered using gonadotropin-releasing hormone (GnRH) agonists that temporarily disable production of testosterone in the testicles. Another method is to use anti-androgen medications to block the body's ability to use androgens for the production of testosterone.

Treatment of advanced prostate cancer with ADT usually leads to remission lasting 2 to 3 years, but in most cases the prostate cancer progresses to an androgen-independent state and leads to widespread metastases. [48-50]

1.4.3 Chemotherapy

The most common chemotherapy for prostate cancer involves intravenous administration of the drugs docetaxel or cabazitaxel. The goal of chemotherapy is to slow or stop the growth of cancer cells. The treatment's side effects involve hair loss, nausea and vomiting, and loss of white blood cells, which increases the risk of infection.

Chemotherapy offers therapeutic potential for androgen sensitive prostate cancer but has been shown to be ineffective for androgen-independent prostate cancer. [51]

1.4.4 Radiation Therapy

Accurate localization of prostatic lesions is challenging, therefore standard radiation therapy of the prostate targets the entire prostate, irradiating both cancer and healthy prostate tissue. Clinical trials have shown that treatment with higher radiation doses may improve overall and progression-free survival but also increase the occurrence of side effects. [52] In light of this issue, there has recently been interest in radiation therapy techniques using integrated radiation boosts to the dominant prostatic lesion, which can spare healthy tissue from radiation dose. [53] This technique has shown potential to increase biochemical control, improve the therapeutic ratio and deliver individualized treatment. [54-57] Hence, there is need for a medical imaging technique that is capable of accurate localization of the dominant prostatic lesion that would allow for intra-prostatic radiation dose escalation.

1.4.4.1 Brachytherapy

The goal of brachytherapy is to deliver an ablative radiation dose to the tumour while sparing surrounding healthy tissues. There are two types of brachytherapy: high dose rate (HDR) and low dose rate (LDR). In HDR brachytherapy, a radioactive source is temporarily placed (i.e. during one visit to the hospital) in the prostate via implanted needles. In LDR brachytherapy, radioactive seeds are permanently implanted into prostate tissue. [58]

Patient selection for brachytherapy focuses on patients with at least 10 years of life expectancy who are at low or medium risk, as per NCCN guidelines. [59] Brachytherapy can also be used as an adjuvant to external beam radiation therapy or ADT in medium to high-risk patients. Brachytherapy only treats intra-prostatic tumours and is therefore contraindicated in patients with metastatic disease. Other contraindications include urinary obstruction, previous pelvic irradiation, previous trans-urethral resection, prostate volume $> 50 \text{ cm}^3$, and inflammatory bowel disease.

1.5 Medical Imaging of Prostate Cancer

The role of imaging in the diagnosis and management of prostate cancer is becoming very important, given its potential for guiding treatment selection and planning. Multiple prostate cancer imaging modalities have been investigated, including ultrasound, magnetic resonance imaging (MRI), computed tomography (CT) and positron emission tomography (PET). The issue of which imaging modality is optimal in terms of sensitivity and specificity is still up for debate and is not clear given the available data.

Imaging has the potential to improve the diagnosis and management of prostate cancer. A modality that enables sensitive and specific diagnosis relative to TRUS would reduce the need for repeat biopsies by assisting in the localization of dominant prostatic lesions and improving biopsy targeting. An imaging modality with a high specificity would assist the identification of high PSA patients eligible for active surveillance and thus reduce the number of unnecessary biopsies that are performed due to false positives, thereby reducing health care costs and reduce patients' psychological distress.

Such an imaging modality would also improve prostate cancer management by assessing the patient's response to treatment and identifying dominant lesions eligible for intra-prostatic radiation boosts, enabling more conformal radiation dose delivery and reducing the incidence and severity of toxicity to the urinary tract. More accurate localization of prostate cancer would also enable better targeting for focal ablative treatment with high dose rate brachytherapy.

1.5.1 Multi-Parametric MRI

Multi-parametric MRI (mp-MRI) uses a combination of parametric MRI techniques. These include magnetic resonance spectroscopy (MRS), T2-weighted imaging (T2W), dynamic contrast-enhanced imaging (DCE-MR) that can analyze tissue microvascular properties and diffusion-weighted imaging (DWI) that is sensitive to restricted diffusion of water molecules. [60] Combinations of DWI and DCE-MR imaging have shown great potential for distinguishing malignant from benign prostate tissues. [61] The advent of widespread PSA screening has increased the detection of prostate cancer in low-risk patients, who are eligible for active surveillance rather than aggressive treatment [62]. It has been shown that mp-MRI may be useful for detecting bilateral involvement of prostate cancer in these patients. [63] Mp-MRI has shown promise for image guidance of biopsies and DWI-MR image intensity has been shown to be negatively correlated with Gleason scores. [64] Mp-MRI has also shown promise for detecting clinically significant prostate cancer with sensitivity comparable to that of biopsy; therefore mp-MRI may be able to reduce the number of biopsies required. [65]

A meta-analysis has shown mp-MRI to have a sensitivity and specificity of 0.74 and 0.88 with a negative predictive value of between 0.65 and 0.94. [66] While other studies have found that mp-MRI is useful for the detection of prostate cancer in the peripheral zone, [67-69] detection in the transition zone is more challenging due to the confounding effects of BPH and the heterogeneous nature of tumours in this zone. [70]

A few studies have found that mp-MRI has shown promise for the detection of cancer after negative biopsy, with a mean prostate cancer detection rate of 37.5%. [71]

Despite the promise of mp-MRI, there is currently no consensus as to the optimal use of the modality for staging or monitoring prostate cancer. In addition, the modality cannot be used in patients with metallic implants or pacemakers.

1.5.2 Ultrasound Imaging

Conventional ultrasound imaging is comparable to DRE in terms of sensitivity and specificity in detecting prostate cancer [72]. To further improve its diagnostic capability, there has been interest in enhanced ultrasound imaging techniques, which are briefly described here.

Prostate perfusion can be measured using color-Doppler ultrasound imaging, by detecting the Doppler frequency/phase shift reflected from moving blood. [73-75] Power Doppler techniques are capable of measuring the amplitude of the reflected ultrasound signal and are more sensitive to small changes in flow velocity. [76] However, Doppler ultrasound imaging techniques are not sufficiently sensitive to eliminate the need for systematic biopsy sampling. [77] A study of Japanese men found that Power Doppler detected prostate cancer with a sensitivity of 98%, negative predictive value of 99%, and

a positive predictive value of 57%, leading the authors to suggest that the technique may be most useful in men with smaller prostates. [78]

As prostate cancer is associated with increased microvessel density, the use of contrast enhanced ultrasound (CE-US) imaging has potential for early detection of prostate cancer. Microvessels in malignant prostate cancer have been shown to be more uniform than in benign tissue. [79] The disadvantage of ultrasound imaging is poor resolution such that detection of flow in microvessels is difficult. This disadvantage can be somewhat overcome with the use of microbubble contrast agents because they intensely reflect and amplify the ultrasound signal from within the microvessels. These CE-US techniques have shown promise for the detection of diffuse prostatic cancer in the absence of a dominant lesion and may be useful for identifying patients that do not require a repeat biopsy or a systematic 12-core biopsy. [80]

1.5.3 Computed Tomography Imaging

1.5.3.1 Non-contrast CT

The use of non-contrast CT for the detection and staging of prostate cancer is non-existent due to poor contrast between different structures both within and outside of the prostate. The role of non-contrast CT for prostate cancer imaging is limited to treatment planning and PET-CT, where it can be helpful for attenuation & scatter correction of PET images and the localization of certain anatomical structures when co-registered with PET images. [81]

1.5.3.2 CT Perfusion

CT Perfusion (CTP) or dynamic contrast enhanced CT (DCE-CT) is a dynamic imaging technique that measures hemodynamic information and functional parameters such as blood flow (BF), blood volume (BV), and permeability surface-area product (PS). It involves the intravenous injection of an iodinated contrast agent during a set of serially acquired CT images to measure delivery of contrast via blood flow and its uptake into the extravascular space.

CT measures the attenuation coefficient of tissue, expressed in Hounsfield Units (HU), a linear transformation of the radio-density such that the value for water at standard temperature and pressure is 0 HU, and air is -1,000 HU. The value of HU measured is linearly proportional to the concentration of contrast in tissue. Hence, the dynamic acquisition of time density curves (TDC) provides direct insight into temporal changes to the contrast concentration in a given voxel. A rule of thumb is that when scanning at 80kVp, 1 mg of iodine per ml is equivalent to an enhancement of 32 HU. [82]

The Johnson and Wilson model [83, 84] assumes that tissues consist of capillary and interstitial tissue. The capillaries are modeled as a cylinder of length L and volume V_b in which blood enters at the arterial end and exits at the venous end. The interstitial tissue is represented as an annulus around the capillary cylinder. (Figure 1.3) As the solute (CT contrast agent) travels along the cylinder from the arterial to the venous end, it diffuses into the interstitial space and thus the concentration C_b of the solute in the capillaries is dependent upon the axial position x of the given solute molecule and time t . The interstitial compartment is assumed to be a well-mixed compartment and hence the interstitial solute

concentration C_e is only a function of time, t . The justification for this approximation is that the arterial and venous end of capillaries are randomly oriented in tissue and thus would appear to be uniform since a CT voxel encompasses a large number of capillaries.

The transport and exchange of solute is described by the following equation:

$$\frac{\partial C_b(x, t)}{\partial t} + \frac{FL}{V_b} \cdot \frac{\partial C_b(x, t)}{\partial x} + \frac{PS}{V_b} [C_b(x, t) - C_e(t)] = 0 \quad (1.1)$$

Where F is the capillary blood flow in ml/min/g and PS is the permeability-surface area product, which is the total diffusional flux across all capillaries per unit mass of tissue.

The concentration of the interstitial compartment is defined by:

$$V_e \frac{dC_e(t)}{dt} = \frac{PS}{L} \int_0^L [C_b(x, t) - C_e(t)] dx \quad (1.2)$$

The extraction efficiency E defines the fraction of solute that diffuses from the capillaries into the interstitial space during a single pass between the arterial and venous ends of the capillaries. It can be shown that E is related to F and PS by: [85, 86]

$$E = \frac{C_a(t - T_c) - C_v(t)}{C_a(t - T_c) - C_e} = (1 - e^{-\frac{PS}{F}}) \quad (1.3)$$

where T_c is the capillary transit time and C_a and C_v are the solute concentrations at the arterial and the venous end of the capillaries, respectively.

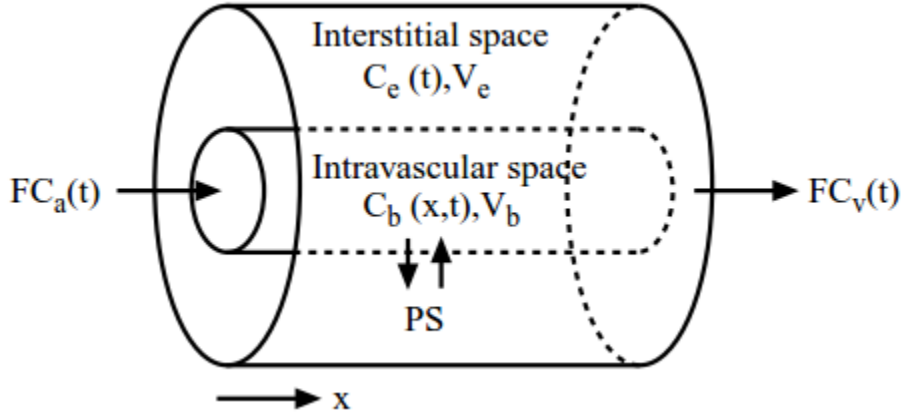


Figure 1.3: Johnson and Wilson model for solute exchange between capillaries and the interstitial space. Symbols are defined in the text.

The solution to the Johnson-Wilson model in the form of Equation (1.1) can only be expressed in the frequency domain through Laplace transforms. For this reason, it is not useful. However, by applying the adiabatic approximation developed by Lee & St. Lawrence [87], a time domain solution for the quantity of solute per unit mass of tissue $Q(t)$ can be expressed as:

$$Q(t) = C_a(t) * F \cdot R(t) \quad (1.4)$$

where $*$ is the convolution operator and $R(t)$ is the impulse residue function (IRF) defined as the fraction of solute that remains in tissue after an instantaneous administration of solute. (Figure 1.4) It is defined as:

$$R(t) = \begin{cases} 1, & t < T_c \\ E e^{-\frac{FE}{V_e}(t-T_c)}, & t \geq T_c \end{cases} \quad (1.5)$$

where V_e is the interstitial volume of solute per unit mass of tissue. The quantity $F \cdot R(t)$ is the blood flow-scaled IRF.

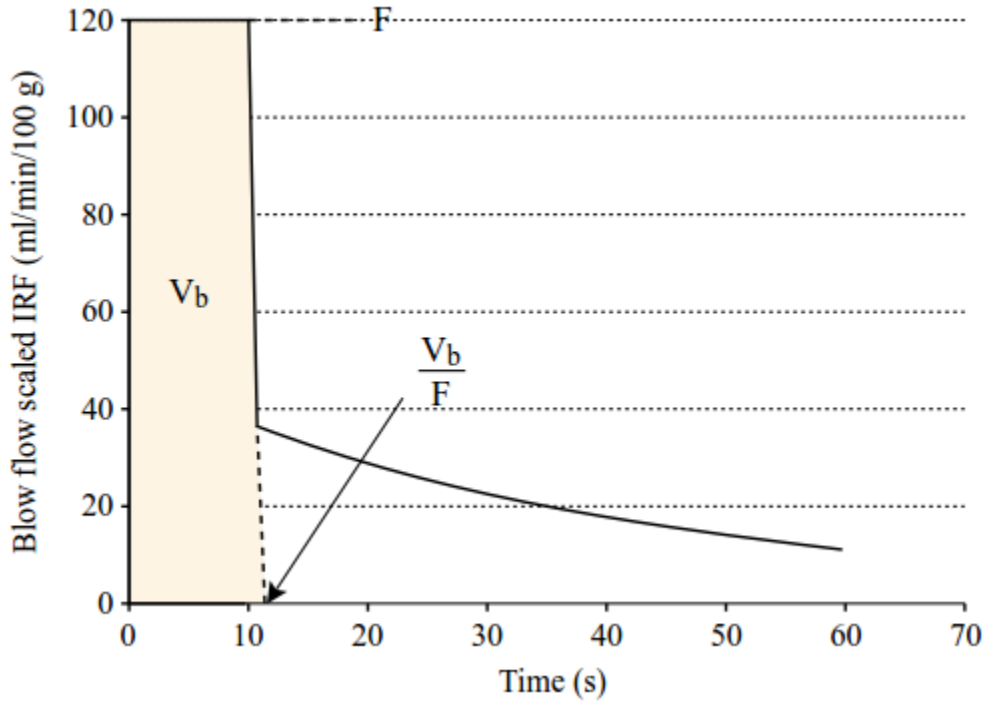


Figure 1.4: The blood-flow scaled impulse residue function based on the Johnson and Wilson model. Symbols are defined in the text. When a bolus of contrast agent is injected into the arterial inlet, the blood flow scaled IRF, which measures the total contrast mass in tissue, remains constant at a value of F up to the tissue transit time T_c (V_b/F), according to the Central Volume Principle [88]). The area under this constant section of the blood flow scaled IRF is equal to V_b . When $t > T_c$, non-extracted contrast agent leaves the tissue.

The arterial time density curve $C_a(t)$ and tissue time density curve $Q(t)$ can be measured from the dynamic images obtained from a dynamic CT study. The blood flow scaled IRF can then be obtained via deconvolution of Equation (1.4), and subsequently, the hemodynamic parameters can be obtained.

CTP has recently been of interest for the detection of prostate cancer, however preliminary studies have shown inconsistent results. Cullu and colleagues reported a study of 25 patients and found significant BF and PS differences between prostate carcinoma and surrounding prostate tissue. [89] Luczynska et. al. found in a prospective study of 94 patients that prostate cancer exhibited higher BF and BV compared to normal prostate tissue. [90] A later study by the same group found correlations between CTP parameters and Gleason score as well as PSA level. Huellner et. al. also found similar results, however they concluded that the correlations were not clinically significant. [91]

1.5.4 Positron Emission Tomography

PET imaging with ^{18}F -fluorodeoxyglucose (FDG) can be used to image glucose metabolism in the prostate. FDG PET imaging of prostate cancer is based on the increased glucose metabolism by anaerobic glycolysis that is observable in malignant cancer cells. This phenomenon is known as the Warburg effect. [92] While it is not clear why cancer cells have a proclivity for producing large amounts of ATP relative to normal cells, this mechanism can nevertheless be used as a biomarker for the presence of malignancy. [93]

In tissue, FDG is phosphorylated into FDG-6-phosphate, which becomes irreversibly bound to cells because the enzyme required for the reversible step, is not widely present in most cancers. [94] This cell-trapping mechanism is exploited by ^{18}F -FDG PET, allowing for the localization of tumour cells with functional imaging.

FDG PET is not without limitations. In some cases, FDG has been known to accumulate in prostatitis, normal prostate tissue and benign prostatic hyperplasia (BPH). [95-97] The tracer can also accumulate in the urinary bladder, whose elevated signal can

obscure measurement of uptake in the prostate. [98, 99] These factors adversely affect the sensitivity and specificity of the modality such that ^{18}F -FDG PET is not recommended for diagnosis or staging of organ-confined prostate cancer. [93]

Positron Emission Tomography (PET) provides metabolic information for a variety of applications via quantification of the uptake of a radiolabeled molecule of interest in tissue. Recently, PET imaging with ^{18}F -fluoromethylcholine (FCH) has been under investigation for the detection and localization of both de-novo and recurrent prostate cancer (PCa) as well as distant metastatic disease. [100]

1.6 Animal Models of Prostate Cancer

Animal models of prostate cancer include genetically engineered and xenograft mouse models, rat models and canine models. [101] This section briefly discusses the various animal models as well as the prostate cancer cell lines that are most commonly used.

1.6.1 Transgenic Mouse Model

Transgenic mice are genetically engineered to develop prostate carcinoma. The advantage of these models is that they reflect the full progression of prostate cancer, from the development of pre-invasive lesions through to the progression of metastatic disease in the presence of a fully functional immune system. The disadvantage is that the lesions are engineered to begin formation early in the life of the mouse, which results in significant biological differences when compared to humans since humans develop prostate cancer at later stages in life [102]. Additionally, the mouse prostate is quite small and therefore

difficult to resolve accurately due to the limited resolution of imaging modalities such as PET. Finally, transgenic mouse models are often more costly when compared to xenograft mouse models.

1.6.2 Xenograft Mouse Model

In xenograft mouse models, prostate cancer cells are subcutaneously or orthotopically implanted into immune-deficient or nude mice. Xenograft mouse models have been useful for studying mechanisms of immune cells in therapeutic resistance [103], and for identifying potential biomarkers for imaging studies. The disadvantage of this technique is that there are a limited number of cell lines currently available, all of which represent advanced disease. Hence, xenograft mouse models are not suitable for prevention studies of prostate cancer. The tumor microenvironment may also be different from in-situ prostate cancer due to either the location of the tumor or its growth in the context of a compromised immune system.

1.6.2.1 Prostate Cancer Cell Lines

The two most common prostate cancer cell lines are PC-3 cells and LNCaP cells. [104] PC-3 cells do not express an androgen receptor and their growth is androgen independent. They are most similar to prostatic small cell neuroendocrine carcinoma (SCNC), which is extremely aggressive and not responsive to hormonal therapy. Patients with SCNC typically present with locally advanced and metastatic disease. [105, 106] Conversely, LNCaP cells are androgen dependent cells that resemble prostate adenocarcinoma, which is responsive to hormonal therapy.

1.6.3 Rat & Canine Models

Rat models of prostate cancer are available, with certain rat strains possessing high rate of spontaneous carcinoma and other strains providing the potential for induced carcinoma. [107] The larger size of rats holds potential for more accurate imaging of the prostate with lower resolution imaging modalities. The disadvantage is that these models are less common, and hence there are far fewer analytical reagents available for the histological tumour analysis of these models, therefore their use and applicability are limited.

Canines spontaneously develop prostate cancer, providing the opportunity to perform prostate cancer imaging studies in a natural environment. Similar to rats, their much larger size compared to mice can improve imaging accuracy with lower resolution modalities. However, producing tumors via implantation of tumor cell lines or genetic means in canines is much more difficult, hence the use of canine models of prostate cancer has been less common. Nevertheless, the larger size and natural tumor environment holds promise for more clinically translatable animal studies of prostate cancer and for identifying the potential clinical utility of novel molecular imaging biomarkers. [108]

1.7 Imaging of Choline Metabolism

1.7.1 The Kennedy Pathway

The Kennedy Pathway, named after Eugene Kennedy who elucidated it in 1956, describes the *de novo* synthesis of phosphatidylcholine and phosphatidylethanolamine, two of the most abundant phospholipid species in eukaryotic cells. [109, 110] In particular, phosphatidylcholine is a phospholipid that is incorporated into the cell membrane.

The phosphorylation of choline is catalyzed by the enzyme choline kinase (CK), which is widely distributed in eukaryotic cells. [111] Choline is carried into the cell via choline transporters. Once inside, the ATP-dependent phosphorylation by the CK enzyme phosphorylates the choline into phosphocholine (PC). [112] (Figure 1.5) PC undergoes further steps and is eventually incorporated into the cell membrane as phosphatidylcholine.

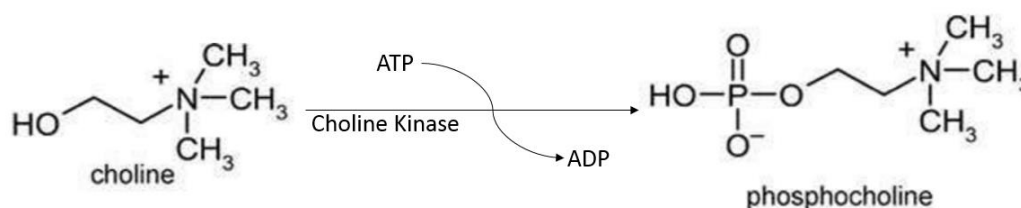


Figure 1.5: ATP-dependent phosphorylation of choline by choline kinase.

The CK enzyme is overexpressed in a variety of cancer cells, including those of the prostate. [113] In addition, it has been shown that malignant prostate tissue contains more phosphocholine when compared to benign or healthy prostate tissue. [114] For these reasons, choline uptake has been of interest as a potential endogenous marker of tumour proliferation.

1.7.2 ¹⁸F-Fluorocholine PET Imaging

It is possible to use PET imaging to investigate the metabolism of choline in different tissues. This is accomplished by synthesizing a radiolabeled choline molecule such as ¹⁸F-Fluorocholine (FCH), also known as ¹⁸F-Fluoromethylcholine. This radiolabeled choline molecule can then be administered and its uptake in the prostate visualized with PET imaging.

Investigations of ^{18}F -FCH PET for the initial staging of PCa have produced mixed results. [115-117] The modality has been found to be useful for the staging and restaging of PCa in patients with elevated PSA, however accurate staging of smaller lesions and patients with lower PSA has been challenging. [118-120] Identification of de-novo dominant prostatic lesions with ^{18}F -FCH-PET has proved difficult due to the low contrast between PCa and other tissues exhibiting similar levels of tracer uptake, such as benign prostatic hyperplasia (BPH). [121, 122] This is counter-intuitive given that, as mentioned previously, the CK enzyme is overexpressed in prostate cancer and there is more phosphocholine in prostate cancer vs. benign tissue.

These studies used the standardized uptake value (SUV), a semi-quantitative technique that is common in the analysis of PET studies. The mixed findings regarding the efficacy of prostate cancer detection with FCH PET may be due to the limitations of the SUV.

1.8 Quantitative Analysis of PET

1.8.1 Standardized Uptake Value

The majority of clinical PET studies utilize the most common PET analysis metric, the semi-quantitative standardized uptake value (SUV), which is a measure of the normalized voxel radioactivity concentration weighted by both the patient weight and the injected radiopharmaceutical dose. [123] The primary reason for its frequent clinical use is that it does not require any arterial blood sampling, which is clinically cumbersome. A group of voxels contained within a region of interest (ROI) is typically used for the analysis. The most common quantification methods include determination of the mean

SUV of voxels within the ROI, which is subject to inter and intra observer variability, [124] and determination of the maximum SUV over all voxels, which is subject to image noise. [125] In addition, the SUV carries the assumption that the time integral of the arterial time activity curve, which governs the quantity of tracer available to tissue, is similar from patient to patient. While this generally holds true, it is not valid for many cases, such as in a patient that has impaired renal clearance of the radiotracer as a result of a prior treatment. [126] In this case, more radiotracer would be available to the tissue resulting in overestimation of the SUV. For these reasons, the use of the SUV as a quantitative index is generally discouraged and it is subject to large variability when used in multicenter trials. [127] Finally, while SUV correlates well with the metabolic influx constant K_i obtained from graphical methods, it may lead to opposite conclusions regarding progression of disease. [128]

Another drawback of the SUV is that it does not discriminate between tracer molecules that are in different physiological states. For instance, it cannot determine what proportion of the tracer molecules are in blood vessels, in the interstitial space surrounding cells, or bound to cells. This decreases the ability to discriminate between regions that demonstrate similar tracer activity, yet exhibit different tracer kinetic properties. This is illustrated in Figure 1.6.

FCH is of interest because choline is phosphorylated by the enzyme choline kinase into phosphocholine, which is incorporated into the cell membrane [129] and it is known that malignant tumours exhibit an increased rate of membrane synthesis. [130] Malignant prostate tumours also possess high levels of phosphocholine relative to benign prostate

tissues, [114] and phosphocholine levels are higher in human prostate cells derived from metastases than in normal prostate epithelial and stromal cells. [131] These data would lead one to expect lower choline kinase activity in BPH compared to malignant tissue, which cannot be discriminated using the SUV. The poor discriminating capability of SUV is potentially due to pooling of the tracer in the interstitial space of BPH contributing to the SUV signal, or the inability of the SUV to identify TAC's with different kinetics when measured at time frames during which SUV in both regions is similar. Nevertheless, this is a plausible explanation for why similar SUV is seen in BPH and malignant tissues.

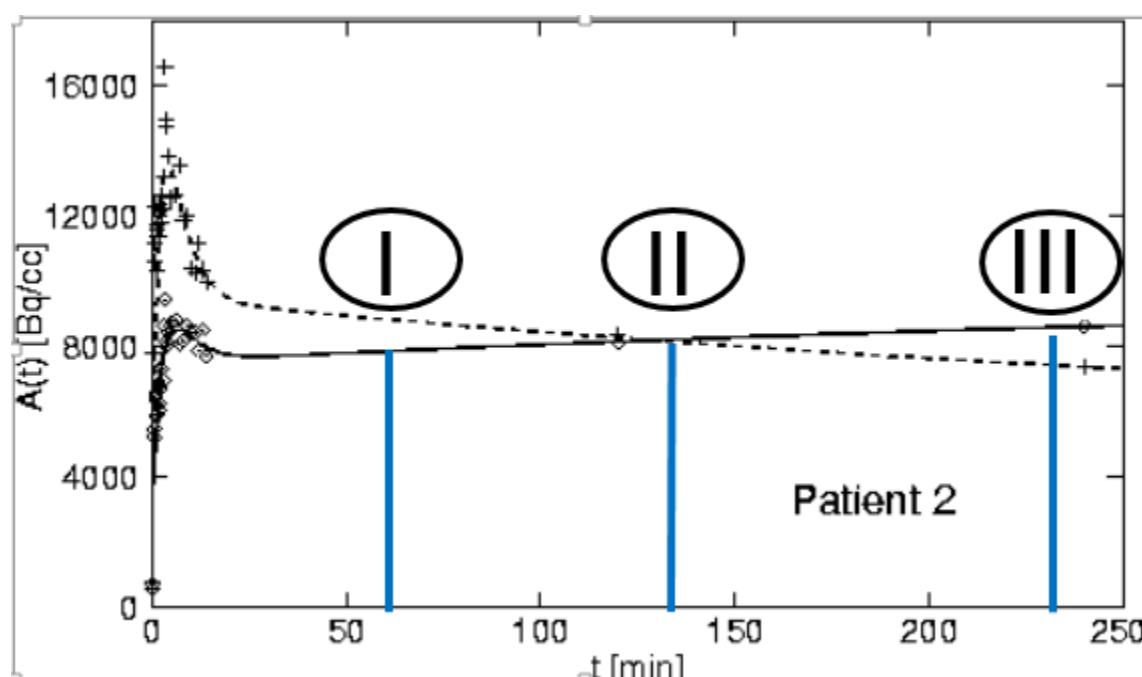


Figure 1.6: Sample TAC's from two different regions with different kinetics. The SUV produces different conclusions at time points I, II and III. (Data source: [132]. ©Institute of Physics and Engineering in Medicine. Reproduced by permission of IOP Publishing. All rights reserved.)

1.8.2 Kinetics Modeling

Quantitative tracer kinetic modeling allows for the determination of the conversion rate constants of the radiolabeled molecule into its different physiological states in-vivo. One common technique is compartment modeling in which unique physiological states are each represented as different, well-mixed compartments. Each compartment is assigned a differential equation defining the rate of change of the compartment's activity concentration per unit time. Tracer can be exchanged between compartments, and a rate constant specifies the rate at which the activity concentration in a given compartment will be altered by this exchange.

The arterial time activity curve (TAC) serves as input for the compartment model. Mathematically, this input function is not technically a compartment given that it is a measured quantity and not solved for, however some authors nevertheless include it as a compartment in the model. This work will follow this convention from this point forward.

Compartment models include a number of assumptions. The compartments are assumed to be well-mixed; there is no spatial concentration gradient within individual compartments. The second assumption is that the amount of tracer injected is small enough that it does not alter the system physiologically. Third, the system must be in a steady-state where the inter-compartmental rate constants are not changing with time. The final assumption is that labeling the molecule of interest does not significantly affect its properties.

1.8.2.1 The 2-Compartment Model

The 2-compartment model can describe tissue uptake for solute that is inert (not metabolized) such as a CT contrast agent. This model is shown in Figure 1.7 and is defined by the following equations:

$$\frac{dC_e(t)}{dt} = K_1 C_a(t) - k_2 C_e(t) \quad (1.6)$$

$$Q(t) = V_b C_a(t) + C_e(t) \quad (1.7)$$

Where $C_e(t)$ is the concentration in the interstitial compartment, K_1 is the forward rate constant from the intravascular to the interstitial space, k_2 is the backflux rate constant from the interstitial space to the intravascular space, $C_a(t)$ is the arterial concentration of solute, and V_b is the solute volume per unit volume of blood.

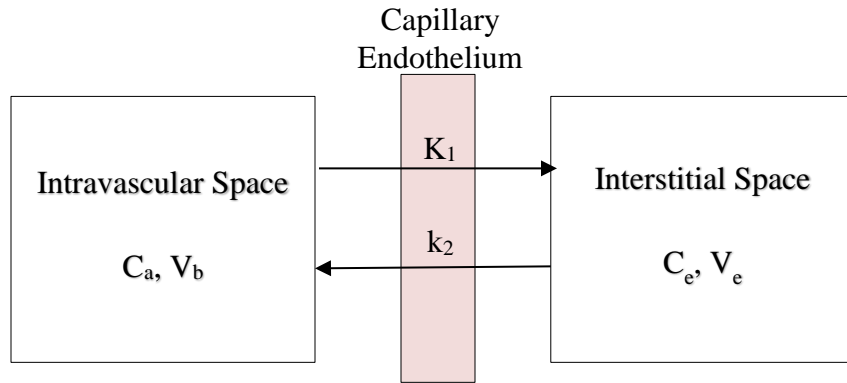


Figure 1.7: The 2-compartment model for an inert solute. Symbols defined in text.

The solution and operational equation for the 2-compartment model is:

$$Q(t) = V_b C_a(t) + K_1 \int_0^t C_a(u) e^{-k_2(t-u)} du \quad (1.8)$$

where u is the convolution variable for the convolution integral. Note that this equation is similar to Equation (1.4), in that

$$K_1 = FE \quad (1.9)$$

$$k_2 = \frac{K_1}{V_e} = \frac{FE}{V_e} \quad (1.10)$$

The difference here is that the intravascular compartment is assumed to be well-mixed and hence its concentration is uniform and not spatially dependent. The parameters for the 2-compartment model can be obtained by solving Equation (1.8) using a variety of non-linear regression methods. [133]

1.8.2.2 The 3-Compartment Model

The 2-compartment model can be extended to accommodate the case of a tracer that is bound in the tissue by a target process (e.g. phosphorylation by choline kinase for ^{18}F -FCH) by adding an additional compartment. This 3-compartment model is shown in Figure 1.8 and requires two added rate constants: k_3 is the binding rate constant of the target process and k_4 is the dissociation rate constant. The binding rate constant can have varying physiological meanings depending on the type of tracer molecule under study. For instance, in the case of FCH, k_3 represents the rate at which radiolabeled choline permeates cell membrane and then becomes phosphorylated. The enzyme choline kinase catalyzes this phosphorylation reaction, therefore k_3 represents the activity of choline kinase.

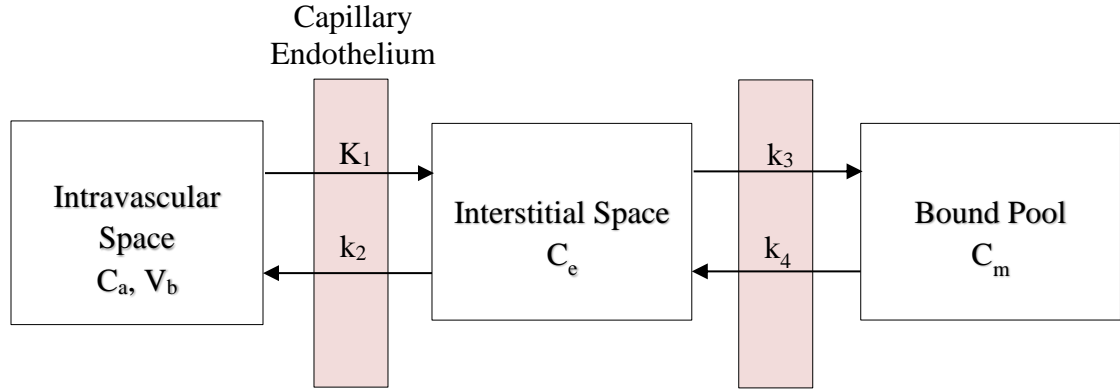


Figure 1.8: 3-Compartment model for metabolized tracers.

The equations governing the 3-compartment model are as follows:

$$\frac{dC_e(t)}{dt} = K_1 C_a(t) - (k_2 + k_3) C_e(t) + k_4 C_m(t) \quad (1.11)$$

$$\frac{dC_m(t)}{dt} = k_3 C_e(t) - k_4 C_m(t) \quad (1.12)$$

$$Q(t) = V_b C_a(t) + C_e(t) + C_m(t) \quad (1.13)$$

where $C_m(t)$ is the concentration of the bound pool. The solution and operating equation of the 3-compartment model is:

$$Q(t) = V_b C_a(t) + C_a(t) * [G e^{-\alpha t} + H e^{-\beta t}] \quad (1.14)$$

where

$$G = K_1 \left(\frac{k_4 + k_3 - \alpha}{\beta - \alpha} \right) \quad (1.15)$$

$$H = K_1 \left(\frac{k_4 + k_3 - \beta}{\alpha - \beta} \right) \quad (1.16)$$

$$\alpha = \frac{k_2 + k_3 + k_4 + \sqrt{(k_2 + k_3 + k_4)^2 - 4k_2k_4}}{2} \quad (1.17)$$

$$\beta = \frac{k_2 + k_3 + k_4 - \sqrt{(k_2 + k_3 + k_4)^2 - 4k_2k_4}}{2} \quad (1.18)$$

A non-linear regression can be performed to fit Equation (1.14) and determine the parameters that give the best fit to the measured data.

1.8.3 Graphical Analysis

Graphical analysis is a simple, model-independent method for quantifying the net uptake of a particular tracer in tissue. There are two well-known graphical methods: the Patlak Plot and the Logan Plot. The Patlak plot is applicable to tracers that bind irreversibly to the target process, and the Logan Plot applies to reversible tracers.

1.8.3.1 Patlak Plot

The Patlak Plot applies to irreversible tracers and measures the influx constant K_i of the tracer. The influx constant is the amount of tracer that has been taken up in tissue relative to the amount available in the plasma.

In the context of the 3-compartment model, K_i is defined as:

$$K_i = K_1 \left(\frac{k_3}{k_2 + k_3} \right) \quad (1.19)$$

where variables are as described in Section 1.8.2.2.

In the case of an irreversible tracer, any tracer that becomes bound to the target is irreversibly trapped in the bound pool ($k_4 = 0$). Patlak et. al. showed that in this case, the graphical analysis equation for the Patlak Plot is: [134, 135]

$$\frac{Q(t)}{C_a(t)} = K_i \frac{\int_0^t C_a(T) dT}{C_a(T)} + (V_e + V_p) \quad (1.20)$$

The arterial and tissue TAC's can be used to create a Patlak plot, where after some time the system reaches equilibrium and the curve becomes linear. The slope of this curve is K_i with intercept $(V_e + V_p)$. This equilibrium is achieved once the extravascular distribution volume of free tracer in tissue water, V_e , becomes constant.

1.8.3.2 Logan Plot

The Logan Plot applies to reversible tracers and measures the distribution volume V_d of the tracer. The distribution volume is defined as the ratio of tracer mass in tissue to tracer concentration in arterial blood at equilibrium.

For the 2-compartment (one tissue) model, it is equivalent to the extravascular distribution volume V_e of free tracer in tissue water:

$$V_d = V_e = \frac{K_1}{k_2} \quad (1.21)$$

The distribution volume for the 3-compartment (two tissue) model is not equivalent to V_e since it also includes tracer that is specifically bound to the target, while V_e is the distribution volume of non-displaceable (free + non-specifically bound) tracer. [136] The distribution volume for the 3-compartment model is:

$$V_d = V_e \left(1 + \frac{k_3}{k_4} \right) + V_b \quad (1.22)$$

The distribution volume can be calculated with a Logan Plot. [137] In the context of a 3-compartment model with arterial and tissue TAC's $C_a(t)$ and $Q(t)$, respectively, the Logan Plot is based on the following equation:

$$\frac{\int_0^t Q(t')dt'}{Q(t)} = V_d \frac{\int_0^t C_a(t')dt'}{Q(t)} + int \quad (1.23)$$

The integral of the tissue TAC is plotted vs. the integral of the arterial TAC and both normalized to the tissue TAC. After a time t^* , the steady-state condition is met and the curve is linear where V_d represents the slope of the linear portion of the curve. The steady state condition occurs when the ratio of tracer in tissue to tracer in arterial blood becomes constant over time. For the 3-compartment model, the steady state condition occurs when

$$\frac{C_e(t) + C_m(t)}{C_a(t)} \quad (1.24)$$

becomes constant. [137]

1.8.4 Kinetics Modeling of FCH PET: Motivation

The k_3 rate constant represents the rate at which tracer molecules are binding to their target. As mentioned in Section 1.7.1, in the case of FCH, this binding rate constant represents the activity of choline kinase, which may be different for benign vs. malignant prostate tissues.

Obtaining a robust estimate of the binding rate constant is challenging due to PET image noise as well as the covariance between model parameters. [138] To reduce these effects, it is possible to estimate “macroparameters” that are dependent on multiple model parameters, such as the distribution volume V_d [137] or the influx constant K_i [134] that depends on the binding rate constant. However, these are not pure measures of target

binding because they are subject to confounding effects, such as blood flow in the local vasculature.

A standard 3-compartment model solution consists of five different model parameters: V_b , K_1 , k_2 , k_3 and k_4 . It is possible to reduce the effect of parameter covariance by reducing the number of estimated parameters in the model, which can be achieved if one or more parameter values are measured by other means. With PET-CT scanners currently available, it is possible to perform a dynamic contrast enhanced CT (DCE-CT) scan immediately prior to an ^{18}F -FCH PET scan. Kinetic analysis of DCE-CT data enables calculation of local vascular blood volume (BV) and blood flow (BF) in tissue, which are factors that confound the measurement of the binding rate constant. [139] By incorporating these measured values from DCE-CT, it is possible to reduce the 3-compartment ^{18}F -FCH PET model from five to only two parameters to be estimated, which could result in a more robust and accurate estimate of the binding rate constant.

Kinetic analysis of DCE-CT and dynamic PET data often involves the minimization of a cost function, the sum of squared differences between the fit and the true data, using nonlinear regression methods. The primary limitation of nonlinear optimization algorithms, such as the Levenberg-Marquardt algorithm, [140, 141] is the heavy dependence of the solution on the choice of starting parameter values, since the algorithm will terminate if it finds a local minimum – regardless of whether it is the optimal solution. This directly leads to an increase in the bias and standard deviation of parameter estimates, particularly when noise is present in the PET imaging data. The most robust nonlinear optimization method involves an exhaustive search in the entire parameter space to

determine the combination of parameter values which gives the absolute minimum of the cost function. The principal drawback of this approach is that it is computationally intensive and time consuming, making it impractical when timely results are critical in the clinic.

1.9 Objectives and Outline

1.9.1 Hypothesis

I hypothesize that PET studies of prostate cancer can be significantly improved through quantitative tracer kinetic analysis using 3-compartment models that incorporate quantitative data from DCE-CT studies. Importantly, these two imaging techniques can be acquired with a single PET-CT scan. Specifically, I posit that this hybrid imaging technique will allow more accurate and less variable measurement of the binding rate constant, k_3 , in PET imaging studies using reversible tracers. Exploiting this hybrid imaging technique to obtain more accurate measurements of k_3 may be useful to quantify the phosphorylation rate of ^{18}F -FCH in tissue, which could allow for the differentiation of malignant prostate cancer from benign or atrophied prostate tissue. This could improve targeting of the dominant prostatic lesion when using TRUS guided biopsy and could potentially reduce the number of cores that need to be sampled from the prostate. In addition, more accurate targeting of the dominant prostatic lesion would be useful in assisting targeting of intra-prostatic radiation dose escalation and focal ablative therapy.

1.9.2 Research Objectives

The primary objective of this thesis was to improve upon quantitative tracer kinetic modelling techniques, in terms of ease of implementation, accuracy and variability of parameter estimates. This objective was met through the following aims:

1. Investigation of the feasibility of using venous TAC's instead of arterial TAC's for the measurement of distribution volume with the Logan Plot. The effect of venous dispersion between the arterial and venous sampling sites of the human forearm on the venous TAC was simulated and used to compare distribution volume measurements obtained using both arterial and simulated venous TAC's.
2. Implementation of linearized versions of compartment models to reduce computation time, and to simulate what effect incorporating functional parameters from DCE-CT would have on the accuracy and variability of estimates of the binding rate constant, k_3 .
3. Investigation of the use of hybrid DCE-CT/PET imaging in a mouse model of PC-3 human prostate cancer to demonstrate the feasibility of creating functional maps of the k_3 parameter in a short amount of time, as well as to determine whether there is a correlation between the k_3 parameter and tumor volume or the expression of the choline kinase enzyme as demonstrated by immunohistochemistry staining.

1.10 References

1. *Canadian Cancer Society's Advisory Committee on Cancer Statistics: Canadian Cancer Statistics 2015*. 2015, Toronto, Canada.
2. Giovannucci, E., *Nutritional factors in human cancers*. Adv Exp Med Biol, 1999. **472**: p. 29-42.
3. Schmitz-Drager, B.J., et al., *Nutrition and prostate cancer*. Urol Int, 2001. **67**(1): p. 1-11.
4. Jankevicius, F., S.M. Miller, and R. Ackermann, *Nutrition and risk of prostate cancer*. Urol Int, 2002. **68**(2): p. 69-80.
5. Abid, Z., A.J. Cross, and R. Sinha, *Meat, dairy, and cancer*. Am J Clin Nutr, 2014. **100 Suppl 1**: p. 386s-93s.
6. Carruba, G., et al., *Nutrition, aging and cancer: lessons from dietary intervention studies*. Immun Ageing, 2016. **13**: p. 13.
7. Pienta, K.J. and D. Bradley, *Mechanisms Underlying the Development of Androgen-Independent Prostate Cancer*. Clinical Cancer Research, 2006. **12**(6): p. 1665-1671.
8. Feldman, B.J. and D. Feldman, *The development of androgen-independent prostate cancer*. Nat Rev Cancer, 2001. **1**(1): p. 34-45.
9. Chen, C.D., et al., *Molecular determinants of resistance to antiandrogen therapy*. Nat Med, 2004. **10**(1): p. 33-9.
10. Gregory, C.W., et al., *Androgen receptor stabilization in recurrent prostate cancer is associated with hypersensitivity to low androgen*. Cancer Res, 2001. **61**(7): p. 2892-8.
11. Weber, M.J. and D. Gioeli, *Ras signaling in prostate cancer progression*. J Cell Biochem, 2004. **91**(1): p. 13-25.
12. Schulz, W.A., M. Burchardt, and M.V. Cronauer, *Molecular biology of prostate cancer*. Molecular Human Reproduction, 2003. **9**(8): p. 437-448.

13. Hammerich, K., A. GE, and W. TM, *Anatomy of the prostate gland and surgical pathology of prostate cancer*, in *Prostate Cancer*. 2009, Cambridge University Press: Cambridge.
14. Berry, S.J., et al., *The development of human benign prostatic hyperplasia with age*. The Journal of urology, 1984. **132**(3): p. 474-479.
15. Kost, L. and G. Evans, *Occurence and significance of striated muscle within the prostate*. The Journal of urology, 1964. **92**: p. 703-704.
16. McNeal, J.E., *The zonal anatomy of the prostate*. The prostate, 1981. **2**(1): p. 35-49.
17. McNeal, J.E., *Origin and development of carcinoma in the prostate*. Cancer, 1969. **23**(1): p. 24-34.
18. *Anatomy and Physiology of the Prostate* (<http://www.cancer.ca/en/cancer-information/cancer-type/prostate/anatomy-and-physiology/?region=on>). 2016, Canadian Cancer Society.
19. Richie, J.P., et al., *Effect of patient age on early detection of prostate cancer with serum prostate-specific antigen and digital rectal examination*. Urology, 1993. **42**(4): p. 365-74.
20. Krahn, M.D., et al., *Screening for prostate cancer. A decision analytic view*. Jama, 1994. **272**(10): p. 773-80.
21. Chodak, G.W., P. Keller, and H.W. Schoenberg, *Assessment of screening for prostate cancer using the digital rectal examination*. J Urol, 1989. **141**(5): p. 1136-8.
22. Gann, P.H., C.H. Hennekens, and M.J. Stampfer, *A prospective evaluation of plasma prostate-specific antigen for detection of prostatic cancer*. Jama, 1995. **273**(4): p. 289-94.
23. Draisma, G., et al., *Lead times and overdetection due to prostate-specific antigen screening: estimates from the European Randomized Study of Screening for Prostate Cancer*. J Natl Cancer Inst, 2003. **95**(12): p. 868-78.

24. Whittemore, A.S., et al., *Prostate specific antigen levels in young adulthood predict prostate cancer risk: results from a cohort of Black and White Americans*. J Urol, 2005. **174**(3): p. 872-6; discussion 876.
25. Simardi, L.H., et al., *Influence of asymptomatic histologic prostatitis on serum prostate-specific antigen: a prospective study*. Urology, 2004. **64**(6): p. 1098-101.
26. Nadler, R.B., et al., *Effect of inflammation and benign prostatic hyperplasia on elevated serum prostate specific antigen levels*. J Urol, 1995. **154**(2 Pt 1): p. 407-13.
27. Kawakami, J., D.R. Siemens, and J.C. Nickel, *Prostatitis and prostate cancer: implications for prostate cancer screening*. Urology, 2004. **64**(6): p. 1075-80.
28. Tchetgen, M.B. and J.E. Oesterling, *The effect of prostatitis, urinary retention, ejaculation, and ambulation on the serum prostate-specific antigen concentration*. Urol Clin North Am, 1997. **24**(2): p. 283-291.
29. Yuan, J.J., et al., *Effects of rectal examination, prostatic massage, ultrasonography and needle biopsy on serum prostate specific antigen levels*. J Urol, 1992. **147**(3 Pt 2): p. 810-4.
30. Brawer, M.K., et al., *Screening for prostatic carcinoma with prostate specific antigen*. J Urol, 1992. **147**(3 Pt 2): p. 841-5.
31. Catalona, W.J., et al., *Detection of organ-confined prostate cancer is increased through prostate-specific antigen-based screening*. Jama, 1993. **270**(8): p. 948-54.
32. Crawford, E.D., et al., *Serum prostate-specific antigen and digital rectal examination for early detection of prostate cancer in a national community-based program. The Prostate Cancer Education Council*. Urology, 1996. **47**(6): p. 863-9.
33. Mettlin, C., et al., *The American Cancer Society National Prostate Cancer Detection Project. Findings on the detection of early prostate cancer in 2425 men*. Cancer, 1991. **67**(12): p. 2949-58.
34. Catalona, W.J., et al., *Comparison of digital rectal examination and serum prostate specific antigen in the early detection of prostate cancer: results of a multicenter clinical trial of 6,630 men*. J Urol, 1994. **151**(5): p. 1283-90.

35. Chou, R., et al., *Screening for prostate cancer: a review of the evidence for the U.S. Preventive Services Task Force*. Ann Intern Med, 2011. **155**(11): p. 762-71.
36. Gleason, D.F., *Classification of prostatic carcinomas*. Cancer Chemother Rep, 1966. **50**(3): p. 125-8.
37. Humphrey, P.A., *Gleason grading and prognostic factors in carcinoma of the prostate*. Mod Pathol, 2004. **17**(3): p. 292-306.
38. Gardner, W.A., Jr., *Histologic grading of prostate cancer: a retrospective and prospective overview*. Prostate, 1982. **3**(6): p. 555-61.
39. Epstein, J.I., *Gleason score 2-4 adenocarcinoma of the prostate on needle biopsy: a diagnosis that should not be made*. Am J Surg Pathol, 2000. **24**(4): p. 477-8.
40. Epstein, J.I., et al., *The 2005 International Society of Urological Pathology (ISUP) Consensus Conference on Gleason Grading of Prostatic Carcinoma*. Am J Surg Pathol, 2005. **29**(9): p. 1228-42.
41. Rodriguez, L.V. and M.K. Terris, *RISKS AND COMPLICATIONS OF TRANSRECTAL ULTRASOUND GUIDED PROSTATE NEEDLE BIOPSY: A PROSPECTIVE STUDY AND REVIEW OF THE LITERATURE*. The Journal of Urology, 1998. **160**(6, Part 1): p. 2115-2120.
42. Eichler, K., et al., *Diagnostic value of systematic biopsy methods in the investigation of prostate cancer: a systematic review*. J Urol, 2006. **175**(5): p. 1605-12.
43. Djavan, B., et al., *Prospective evaluation of prostate cancer detected on biopsies 1, 2, 3 and 4: when should we stop?* J Urol, 2001. **166**(5): p. 1679-83.
44. Noguchi, M., et al., *Relationship between systematic biopsies and histological features of 222 radical prostatectomy specimens: lack of prediction of tumor significance for men with nonpalpable prostate cancer*. J Urol, 2001. **166**(1): p. 104-9; discussion 109-10.
45. Autorino, R., et al., *How to decrease pain during transrectal ultrasound guided prostate biopsy: a look at the literature*. J Urol, 2005. **174**(6): p. 2091-7.
46. Loffroy, R., et al., *Current role of multiparametric magnetic resonance imaging for prostate cancer*. Quant Imaging Med Surg, 2015. **5**(5): p. 754-64.

47. Chung, M.S. and S.H. Lee, *Current status of active surveillance in prostate cancer*. Investigative and Clinical Urology, 2016. **57**(1): p. 14-20.
48. Roudier, M.P., et al., *Phenotypic heterogeneity of end-stage prostate carcinoma metastatic to bone*. Hum Pathol, 2003. **34**(7): p. 646-53.
49. Saitoh, H., et al., *Metastatic patterns of prostatic cancer. Correlation between sites and number of organs involved*. Cancer, 1984. **54**(12): p. 3078-84.
50. Bubendorf, L., et al., *Metastatic patterns of prostate cancer: an autopsy study of 1,589 patients*. Hum Pathol, 2000. **31**(5): p. 578-83.
51. Yagoda, A. and D. Petrylak, *Cytotoxic chemotherapy for advanced hormone-resistant prostate cancer*. Cancer, 1993. **71**(3 Suppl): p. 1098-109.
52. Wolff, R.F., et al., *A systematic review of randomised controlled trials of radiotherapy for localised prostate cancer*. Eur J Cancer, 2015. **51**(16): p. 2345-67.
53. von Eyben, F.E., et al., *Radiotherapy Boost for the Dominant Intraprostatic Cancer Lesion-A Systematic Review and Meta-Analysis*. Clin Genitourin Cancer, 2015.
54. Pinkawa, M., et al., *Dose-escalation using intensity-modulated radiotherapy for prostate cancer--evaluation of the dose distribution with and without 18F-choline PET-CT detected simultaneous integrated boost*. Radiother Oncol, 2009. **93**(2): p. 213-9.
55. Al-Mamgani, A., et al., *Update of Dutch multicenter dose-escalation trial of radiotherapy for localized prostate cancer*. Int J Radiat Oncol Biol Phys, 2008. **72**(4): p. 980-8.
56. Kuban, D.A., et al., *Long-term results of the M. D. Anderson randomized dose-escalation trial for prostate cancer*. Int J Radiat Oncol Biol Phys, 2008. **70**(1): p. 67-74.
57. Zietman, A.L., et al., *Comparison of conventional-dose vs high-dose conformal radiation therapy in clinically localized adenocarcinoma of the prostate: a randomized controlled trial*. Jama, 2005. **294**(10): p. 1233-9.
58. Chao, M.W., et al., *Brachytherapy: state-of-the-art radiotherapy in prostate cancer*. BJU Int, 2015. **116** Suppl 3: p. 80-8.

59. Davis, B.J., et al., *American Brachytherapy Society consensus guidelines for transrectal ultrasound-guided permanent prostate brachytherapy*. Brachytherapy, 2012. **11**(1): p. 6-19.
60. Alonzi, R., A.R. Padhani, and C. Allen, *Dynamic contrast enhanced MRI in prostate cancer*. Eur J Radiol, 2007. **63**(3): p. 335-50.
61. Langer, D.L., et al., *Prostate cancer detection with multi-parametric MRI: logistic regression analysis of quantitative T2, diffusion-weighted imaging, and dynamic contrast-enhanced MRI*. J Magn Reson Imaging, 2009. **30**(2): p. 327-34.
62. Noldus, J., et al., *Stage migration in clinically localized prostate cancer*. Eur Urol, 2000. **38**(1): p. 74-8.
63. Delongchamps, N.B., et al., *Multiparametric MRI is helpful to predict tumor focality, stage, and size in patients diagnosed with unilateral low-risk prostate cancer*. Prostate Cancer Prostatic Dis, 2011. **14**(3): p. 232-7.
64. Turkbey, B. and P.L. Choyke, *Multiparametric MRI and prostate cancer diagnosis and risk stratification*. Curr Opin Urol, 2012. **22**(4): p. 310-5.
65. Moore, C.M., et al., *Image-Guided Prostate Biopsy Using Magnetic Resonance Imaging-Derived Targets: A Systematic Review*. European Urology, 2013. **63**(1): p. 125-140.
66. de Rooij, M., et al., *Accuracy of multiparametric MRI for prostate cancer detection: a meta-analysis*. AJR Am J Roentgenol, 2014. **202**(2): p. 343-51.
67. Abd-Alazez, M., et al., *The accuracy of multiparametric MRI in men with negative biopsy and elevated PSA level--can it rule out clinically significant prostate cancer?* Urol Oncol, 2014. **32**(1): p. 45.e17-22.
68. Itatani, R., et al., *Negative predictive value of multiparametric MRI for prostate cancer detection: outcome of 5-year follow-up in men with negative findings on initial MRI studies*. Eur J Radiol, 2014. **83**(10): p. 1740-5.
69. Shakir, N.A., et al., *Identification of threshold prostate specific antigen levels to optimize the detection of clinically significant prostate cancer by magnetic resonance imaging/ultrasound fusion guided biopsy*. J Urol, 2014. **192**(6): p. 1642-8.

70. Delongchamps, N.B., et al., *Multiparametric magnetic resonance imaging for the detection and localization of prostate cancer: combination of T2-weighted, dynamic contrast-enhanced and diffusion-weighted imaging*. BJU Int, 2011. **107**(9): p. 1411-8.
71. Zhang, Z.X., et al., *The value of magnetic resonance imaging in the detection of prostate cancer in patients with previous negative biopsies and elevated prostate-specific antigen levels: a meta-analysis*. Acad Radiol, 2014. **21**(5): p. 578-89.
72. Aarnink, R.G., et al., *Transrectal ultrasound of the prostate: innovations and future applications*. J Urol, 1998. **159**(5): p. 1568-79.
73. Rifkin, M.D., G.S. Sudakoff, and A.A. Alexander, *Prostate: techniques, results, and potential applications of color Doppler US scanning*. Radiology, 1993. **186**(2): p. 509-13.
74. Sudakoff, G.S., et al., *Color Doppler imaging and transrectal sonography of the prostatic fossa after radical prostatectomy: early experience*. AJR Am J Roentgenol, 1996. **167**(4): p. 883-8.
75. Kravchick, S., et al., *Using gray-scale and two different techniques of color Doppler sonography to detect prostate cancer*. Urology, 2003. **61**(5): p. 977-81.
76. Cho, J.Y., S.H. Kim, and S.E. Lee, *Diffuse prostatic lesions: role of color Doppler and power Doppler ultrasonography*. J Ultrasound Med, 1998. **17**(5): p. 283-7.
77. Prando, A., *Prostate: high-frequency Doppler US imaging for cancer detection*. Int Braz J Urol, 2002. **28**(6): p. 577-8.
78. Okihara, K., et al., *Transrectal power Doppler imaging in the detection of prostate cancer*. BJU Int, 2000. **85**(9): p. 1053-7.
79. Kay, P.A., R.A. Robb, and D.G. Bostwick, *Prostate cancer microvessels: a novel method for three-dimensional reconstruction and analysis*. Prostate, 1998. **37**(4): p. 270-7.
80. Gao, Y., et al., *Contrast-enhanced transrectal ultrasonography for the detection of diffuse prostate cancer*. Clin Radiol, 2016. **71**(3): p. 258-64.
81. Brady, Z., et al., *The clinical application of PET/CT: a contemporary review*. Australas Phys Eng Sci Med, 2008. **31**(2): p. 90-109.

82. Lee, T.Y., et al., *Quantitative computed tomography of the brain with xenon enhancement: a phantom study with the GE9800 scanner*. Phys Med Biol, 1990. **35**(7): p. 925-35.
83. Johnson, J.A. and T.A. Wilson, *A model for capillary exchange*. Am J Physiol, 1966. **210**(6): p. 1299-303.
84. Sawada, Y., C.S. Patlak, and R.G. Blasberg, *Kinetic analysis of cerebrovascular transport based on indicator diffusion technique*. Am J Physiol, 1989. **256**(3 Pt 2): p. H794-812.
85. Crone, C., *The Permeability of Capillaries in Various Organs as Determined by Use of the 'Indicator Diffusion' Method*. Acta Physiologica Scandinavica, 1963. **58**(4): p. 292-305.
86. Renkin, E.M., *Transport of potassium-42 from blood to tissue in isolated mammalian skeletal muscles*. Am J Physiol, 1959. **197**: p. 1205-10.
87. St Lawrence, K.S. and T.Y. Lee, *An adiabatic approximation to the tissue homogeneity model for water exchange in the brain: I. Theoretical derivation*. J Cereb Blood Flow Metab, 1998. **18**(12): p. 1365-77.
88. Meier, P. and K.L. Zierler, *On the theory of the indicator-dilution method for measurement of blood flow and volume*. J Appl Physiol, 1954. **6**(12): p. 731-44.
89. Cullu, N., et al., *Feasibility study of CT perfusion imaging for prostate carcinoma*. Eur Radiol, 2014. **24**(9): p. 2236-44.
90. Luczynska, E., et al., *Perfusion CT is a valuable diagnostic method for prostate cancer: a prospective study of 94 patients*. ecancermedicalscience, 2014. **8**: p. 476.
91. Huellner, M.W., et al., *Integrated CT-perfusion shows no meaningful correlation with PSA and presurgical Gleason score in patients with early prostate cancer*. Clinical Imaging, 2014. **38**(6): p. 850-857.
92. Vander Heiden, M.G., L.C. Cantley, and C.B. Thompson, *Understanding the Warburg Effect: The Metabolic Requirements of Cell Proliferation*. Science (New York, N.Y.), 2009. **324**(5930): p. 1029-1033.
93. Jadvar, H., *FDG PET in Prostate Cancer*. PET clinics, 2009. **4**(2): p. 155-161.

94. Smith, T.A., *Mammalian hexokinases and their abnormal expression in cancer*. Br J Biomed Sci, 2000. **57**(2): p. 170-8.
95. Takahashi, N., et al., *The roles of PET and PET/CT in the diagnosis and management of prostate cancer*. Oncology, 2007. **72**(3-4): p. 226-33.
96. Salminen, E., et al., *Investigations with FDG-PET scanning in prostate cancer show limited value for clinical practice*. Acta Oncol, 2002. **41**(5): p. 425-9.
97. Kao, P.F., Y.H. Chou, and C.W. Lai, *Diffuse FDG uptake in acute prostatitis*. Clin Nucl Med, 2008. **33**(4): p. 308-10.
98. Hofer, C., et al., *Fluorine-18-fluorodeoxyglucose positron emission tomography is useless for the detection of local recurrence after radical prostatectomy*. Eur Urol, 1999. **36**(1): p. 31-5.
99. Liu, I.J., et al., *Fluorodeoxyglucose positron emission tomography studies in diagnosis and staging of clinically organ-confined prostate cancer*. Urology, 2001. **57**(1): p. 108-11.
100. Bauman, G., et al., *18F-fluorocholine for prostate cancer imaging: a systematic review of the literature*. Prostate Cancer Prostatic Dis, 2012. **15**(1): p. 45-55.
101. Ittmann, M., et al., *Animal Models of Human Prostate Cancer: The Consensus Report of the New York Meeting of the Mouse Models of Human Cancers Consortium Prostate Pathology Committee*. Cancer Research, 2013. **73**(9): p. 2718-2736.
102. Bavik, C., et al., *The Gene Expression Program of Prostate Fibroblast Senescence Modulates Neoplastic Epithelial Cell Proliferation through Paracrine Mechanisms*. Cancer Research, 2006. **66**(2): p. 794-802.
103. Ammirante, M., et al., *B-cell-derived lymphotoxin promotes castration-resistant prostate cancer*. Nature, 2010. **464**(7286): p. 302-305.
104. Tai, S., et al., *PC3 is a cell line characteristic of prostatic small cell carcinoma*. Prostate, 2011. **71**(15): p. 1668-79.
105. Tetu, B., et al., *Small cell carcinoma of the prostate. Part I. A clinicopathologic study of 20 cases*. Cancer, 1987. **59**(10): p. 1803-9.

106. Oesterling, J.E., C.G. Hauzeur, and G.M. Farrow, *Small cell anaplastic carcinoma of the prostate: a clinical, pathological and immunohistological study of 27 patients*. J Urol, 1992. **147**(3 Pt 2): p. 804-7.
107. Shirai, T., et al., *Experimental prostate carcinogenesis — rodent models*. Mutation Research/Reviews in Mutation Research, 2000. **462**(2–3): p. 219-226.
108. Chevalier, S., et al., *The dog prostate cancer (DPC-1) model: a reliable tool for molecular imaging of prostate tumors and metastases*. EJNMMI Res, 2015. **5**(1): p. 77.
109. Gibellini, F. and T.K. Smith, *The Kennedy pathway--De novo synthesis of phosphatidylethanolamine and phosphatidylcholine*. IUBMB Life, 2010. **62**(6): p. 414-28.
110. Kennedy, E.P. and S.B. Weiss, *The function of cytidine coenzymes in the biosynthesis of phospholipides*. Journal of Biological Chemistry, 1956. **222**(1): p. 193-214.
111. Rontein, D., et al., *Plants synthesize ethanolamine by direct decarboxylation of serine using a pyridoxal phosphate enzyme*. J Biol Chem, 2001. **276**(38): p. 35523-9.
112. Li, Z. and D.E. Vance, *Thematic Review Series: Glycerolipids. Phosphatidylcholine and choline homeostasis*. Journal of Lipid Research, 2008. **49**(6): p. 1187-1194.
113. Glunde, K., M.A. Jacobs, and Z.M. Bhujwalla, *Choline metabolism in cancer: implications for diagnosis and therapy*. Expert Rev Mol Diagn, 2006. **6**(6): p. 821-9.
114. Swanson, M.G., et al., *Quantification of choline- and ethanolamine-containing metabolites in human prostate tissues using ¹H HR-MAS total correlation spectroscopy*. Magnetic Resonance in Medicine, 2008. **60**(1): p. 33-40.
115. Beauregard, J.M., et al., *Pilot comparison of F-fluorocholine and F-fluorodeoxyglucose PET/CT with conventional imaging in prostate cancer*. Journal of medical imaging and radiation oncology, 2010. **54**(4): p. 325-332.

116. Husarik, D.B., et al., *Evaluation of [(18)F]-choline PET/CT for staging and restaging of prostate cancer*. Eur J Nucl Med Mol Imaging, 2008. **35**(2): p. 253-63.
117. Heinisch, M., et al., *Positron emission tomography/computed tomography with F-18-fluorocholine for restaging of prostate cancer patients: meaningful at PSA < 5 ng/ml?* Mol Imaging Biol, 2006. **8**(1): p. 43-8.
118. Cimitan, M., et al., *[18F]fluorocholine PET/CT imaging for the detection of recurrent prostate cancer at PSA relapse: experience in 100 consecutive patients*. Eur J Nucl Med Mol Imaging, 2006. **33**(12): p. 1387-98.
119. Steiner, C., et al., *Three-phase 18F-fluorocholine PET/CT in the evaluation of prostate cancer recurrence*. Nuklearmedizin.Nuclear medicine, 2009. **48**(1): p. 1-9; quiz N2-3.
120. Veas, H., et al., *18F-choline and/or 11C-acetate positron emission tomography: detection of residual or progressive subclinical disease at very low prostate-specific antigen values (<1 ng/mL) after radical prostatectomy*. BJU Int, 2007. **99**(6): p. 1415-20.
121. Schmid, D.T., et al., *Fluorocholine PET/CT in Patients with Prostate Cancer: Initial Experience*. Radiology, 2005. **235**(2): p. 623-628.
122. Igerc, I., et al., *The value of 18F-Choline PET/CT in patients with elevated PSA-level and negative prostate needle biopsy for localisation of prostate cancer*. European Journal of Nuclear Medicine & Molecular Imaging, 2008. **35**(5): p. 976-983.
123. Adams, M.C., et al., *A Systematic Review of the Factors Affecting Accuracy of SUV Measurements*. American Journal of Roentgenology, 2010. **195**(2): p. 310-320.
124. Lucignani, G., *SUV and segmentation: pressing challenges in tumour assessment and treatment*. Eur J Nucl Med Mol Imaging, 2009. **36**(4): p. 715-20.
125. Benz, M.R., et al., *Treatment monitoring by 18F-FDG PET/CT in patients with sarcomas: interobserver variability of quantitative parameters in treatment-induced changes in histopathologically responding and nonresponding tumors*. J Nucl Med, 2008. **49**(7): p. 1038-46.

126. Huang, S.C., *Anatomy of SUV. Standardized uptake value*. Nucl Med Biol, 2000. **27**(7): p. 643-6.
127. Boellaard, R., et al., *Effects of noise, image resolution, and ROI definition on the accuracy of standard uptake values: a simulation study*. J Nucl Med, 2004. **45**(9): p. 1519-27.
128. Freedman, N.M., et al., *Comparison of SUV and Patlak slope for monitoring of cancer therapy using serial PET scans*. Eur J Nucl Med Mol Imaging, 2003. **30**(1): p. 46-53.
129. Wu, G. and D.E. Vance, *Choline kinase and its function*. Biochem Cell Biol, 2010. **88**(4): p. 559-64.
130. Vallabhajosula, S., *¹⁸F-Labeled Positron Emission Tomographic Radiopharmaceuticals in Oncology: An Overview of Radiochemistry and Mechanisms of Tumor Localization*. Seminars in nuclear medicine, 2007. **37**(6): p. 400-419.
131. Ackerstaff, E., et al., *Detection of Increased Choline Compounds with Proton Nuclear Magnetic Resonance Spectroscopy Subsequent to Malignant Transformation of Human Prostatic Epithelial Cells*. Cancer research, 2001. **61**(9): p. 3599-3603.
132. Thorwarth, D., et al., *A kinetic model for dynamic [¹⁸F]-Fmiso PET data to analyse tumour hypoxia*. Phys Med Biol, 2005. **50**(10): p. 2209-24.
133. Gill, P., W. Murray, and M. Wright, *Practical Optimization*. 1981, London: Academic Press.
134. Patlak, C.S., R.G. Blasberg, and J.D. Fenstermacher, *Graphical evaluation of blood-to-brain transfer constants from multiple-time uptake data*. J Cereb Blood Flow Metab, 1983. **3**(1): p. 1-7.
135. Patlak, C.S. and R.G. Blasberg, *Graphical evaluation of blood-to-brain transfer constants from multiple-time uptake data. Generalizations*. J Cereb Blood Flow Metab, 1985. **5**(4): p. 584-90.
136. Innis, R.B., et al., *Consensus nomenclature for in vivo imaging of reversibly binding radioligands*. J Cereb Blood Flow Metab, 2007. **27**(9): p. 1533-9.

137. Logan, J., *Graphical analysis of PET data applied to reversible and irreversible tracers*. Nucl Med Biol, 2000. **27**(7): p. 661-70.
138. Muzi, M., et al., *Kinetic analysis of 3'-deoxy-3'-18F-fluorothymidine in patients with gliomas*. J Nucl Med, 2006. **47**(10): p. 1612-21.
139. Lee, T.Y., T.G. Purdie, and E. Stewart, *CT imaging of angiogenesis*. Q J Nucl Med, 2003. **47**(3): p. 171-87.
140. Levenberg, K., *A Method for the Solution of Certain Problems in Least-Squares*. Quarterly Applied Math, 1944. **2**: p. 164-168.
141. Marquardt, D., *An Algorithm for Least-Squares Estimation of Nonlinear Parameters*. SIAM Journal of Applied Math, 1963. **11**: p. 431-441.

Chapter 2

2 Simulating the effect of venous dispersion on distribution volume measurements from the Logan Plot

2.1 Introduction

There exist various techniques for the analysis of Positron Emission Tomography (PET) data. One technique that is common, but not limited, to the field of neuroreceptor imaging is graphical analysis via the Logan Plot. [1] This technique involves plotting a linear relationship between the normalized integral of the arterial time activity curve (TAC) and that of the tissue TAC. Under equilibrium conditions, the slope of this relationship is equal to the distribution volume, which is a quantitative index of metabolic uptake that is related to the number of free binding sites for a radioligand of interest. [2]

An arterial TAC showing the time course of arterial activity concentration during the study is required for the Logan Plot. An image-derived arterial TAC can be obtained by sampling the acquired images of a dynamic PET study with a user-defined region of interest (ROI) in an artery; this method underestimates the true activity in small diameter arteries (relative to the spatial resolution of the PET scanner) due to partial volume averaging. [3] Presently, the gold standard for measuring arterial activity concentrations is arterial blood sampling, in which the patient's radial artery is cannulated and blood is continuously drawn or discretely sampled in order to measure the activity concentration at various times during the study.

A disadvantage of arterial blood sampling is that it is often much more difficult to cannulate an artery compared to a vein, and it can be painful for the patient. In addition,

arterial cannulation is not without risk, as it may lead to permanent injury to the patient, including arterial occlusion and ischemic damage. [4-7] Additionally, the high arterial pressure of an artery increases the risk of excessive bleeding. On the contrary, this is less of a concern for venous cannulation given the lower venous pressure, and venous sampling is much more common in clinical use compared to arterial sampling. [8]

Some studies have examined the feasibility of using venous blood in the place of arterial blood for a variety of applications. Some of these applications include measurement of glucose metabolism [9, 10], metabolite analysis following administration of ^{11}C -Acetate and ^{11}C -Palmitate [11] and quantification of serotonin receptors [12].

Venous TACs differ from arterial TACs due to the distance that the tracer must travel between arterial and venous sampling sites. Not only is the venous curve's arrival delayed compared to the arterial one, but it is also subject to dispersion effects due to the number of possible routes between the arterial and venous sampling sites. [13] While traversing this distance, different tracer molecules will take different paths through the vascular network and hence travel different path lengths, which results in an underestimate of the peak activity concentration due to broadening of the TAC's peak. Additionally, the extraction efficiency of the PET tracer will affect the amount of leakage that occurs between the sampling sites. The backflux of the leaked tracer into the vascular space would lead to further dispersion of the venous TAC relative to that of the artery. It is expected that these factors could affect the measurement of the distribution volume with the Logan plot when the venous TAC is used instead of the arterial TAC, depending on the extent of the dispersion. This work aims to investigate using computer simulations the relationship

between the extent of venous dispersion from differential path lengths and leakage and the distribution volume measurement with the Logan Plot.

2.2 Methods

2.2.1 Tissue Curve Simulation

A representative arterial TAC, $C_p(t)$, was obtained from an in vivo dynamic ^{18}F -Fluorocholine (FCH) PET human prostate study with acquisition intervals of: 10 x 10 seconds, 5 x 20 seconds, 4 x 40 seconds, 4 x 60 seconds, and 4 x 180 seconds, for a total scan time of 22 minutes. This image-derived TAC was obtained from a mean ROI in the left external iliac artery. For the purposes of this work, this TAC served as a representative instantaneous (as opposed to averaging over the acquisition interval) arterial time activity curve.

The tissue curves in this investigation were generated from the arterial TAC for a variety of parameter sets using a kinetic model. The Johnson & Wilson model for tracer delivery and capillary exchange with parenchymal tissue [14] was modified to include a bound pool compartment connected to the extra-vascular (interstitial) space along with the corresponding rate constants k_3 and k_4 , representing reversible binding of the tracer to cells or other targets. The equations governing the system are:

$$K_1 = FE \quad (2.1)$$

$$k_2 = \frac{K_1}{V_e} \quad (2.2)$$

$$\frac{dC_e(t)}{dt} = K_1 C_p(t) - (k_2 + k_3) C_e(t) + k_4 C_m(t) \quad (2.3)$$

$$\frac{dC_m(t)}{dt} = k_3 C_e(t) - k_4 C_m(t) \quad (2.4)$$

where $C_p(t)$, $C_e(t)$, and $C_m(t)$ are the arterial, interstitial, and bound pool activity concentrations, respectively. A description of the remaining model parameters can be found in Table 2.1.

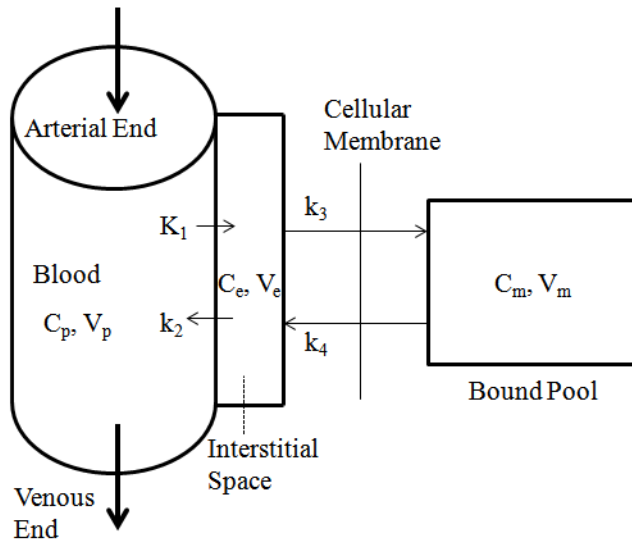


Figure 2.1: Kinetic model used to produce the simulated tissue curves. Tracer flows from the arterial end to the venous end of the capillaries and leaks by passive diffusion into the interstitial space of tissue and then exchange with the tissue bound pool.

By solving Equations (2.3) & (2.4), it can be shown that the impulse residue function $R(t)$ for this model is:

$$R(t) = \begin{cases} 0 & t < t_0 \\ 1 & t_0 < t < (t_0 + MTT) \\ E\left(\frac{\alpha + k_3 + k_4}{\alpha - \beta}\right)e^{\alpha(t-t_0-MTT)} + E\left(-\frac{\beta + k_3 + k_4}{\alpha - \beta}\right)e^{\beta(t-t_0-MTT)} & t > (t_0 + MTT) \end{cases} \quad (2.5)$$

where:

$$\begin{aligned} \alpha &= \frac{-(k_2 + k_3 + k_4) + \sqrt{(k_2 + k_3 + k_4)^2 - 4k_2k_4}}{2} \\ \beta &= \frac{-(k_2 + k_3 + k_4) - \sqrt{(k_2 + k_3 + k_4)^2 - 4k_2k_4}}{2} \end{aligned} \quad (2.6)$$

t_0 is the delay in arrival of tracer at the tissue relative to that at the artery and MTT is the vascular mean transit time.

The tissue TAC was obtained by convolving the arterial TAC with the blood flow-scaled $R(t)$:

$$Q(t) = C_p(t) * (F \cdot R(t)) \quad (2.7)$$

where blood flow (F) was related to blood volume (V_p) and mean transit time (MTT) by the central volume principle [15]:

$$F = \frac{V_p}{MTT} \quad (2.8)$$

Table 2.1: Description of the parameters and parameter values used in the 3-compartment, digital phantom simulation in order to produce simulated tissue TACs.

Parameter	Description	Value	Units
F	Blood Flow	Multiple Values	ml/min/g
E	Extraction Efficiency	0.4	unitless
V_p	Blood Volume	0.1	ml/g
V_e	Interstitial Volume	Multiple Values	ml/g
K_1	Influx constant	Multiple Values	ml/min/g
k_2	Interstitial space to blood backflux constant	Multiple Values	min ⁻¹
k_3	Interstitial space to bound pool constant	Multiple Values	min ⁻¹
k_4	Bound pool to interstitial space backflux constant	0.05, 0.1, 0.3	min ⁻¹
MTT	Mean transit time through capillary bed	Multiple Values	min
t_0	Tracer bolus arrival time	5	seconds

2.2.2 Simulation of Venous Dispersion

To simulate the venous dispersion, a transit time spectrum of the dispersion of tracer from arterial to venous sampling sites was derived from a dynamic contrast enhanced CT study of the forearm as described in the following. The forearm of a supine patient was

placed above the liver and scanned repeatedly at intervals of using 120 kV, 50 mAs and 5 mm slice thickness. The arterial time density curve (TDC) came from a region of interest in the radial artery. The venous TDC came from a region in a vein which was adjacent to the radial artery. The TDCs were smoothed with a moving average filter. The arterial and venous TDCs were then deconvolved to obtain the transit time spectrum $h_{CT}(t)$, using the model in Figure 2.1 with k_3 and k_4 set to zero, since CT contrast agent is inert. Knowing that the transit time spectrum $h_{CT}(t)$ is related to $R(t)$ such that:

$$h_{CT}(t) = -\frac{dR(t)}{dt} \quad (2.9)$$

the venous TAC is given by the following equations.

$$SC \cdot C_{vCT}^m(t) = C_{vCT}(t) = C_{aCT}(t) * h_{CT}(t) \quad (2.10)$$

$$C_{vCT}^m(t) = \begin{cases} 0 & 0 < t < W \\ SC \left\{ (1 - E_{CT}) C_{aCT}(t - W) + k_{2CT} E_{CT} \int_0^{t-W} C_{aCT}(u) e^{-k_{2CT}(t-W-u)} du \right\} & t \geq W \end{cases} \quad (2.11)$$

where $C_{vCT}^m(t)$ and $C_{vCT}(t)$ are the measured and actual venous TAC's, respectively, $C_{aCT}(t)$ is the arterial CT TAC from the radial artery, $h_{CT}(t)$ is the transit time spectrum of CT contrast agent, SC is the scaling factor due to partial volume averaging, E_{CT} is the extraction efficiency of CT contrast agent, k_{2CT} is the backflux rate constant for CT contrast agent from tissue to vascular space, and W is the combined delay time and vascular mean transit time, which excludes the transit time of leaked contrast into the tissue, between the arterial and venous sampling sites. The extraction efficiency E_{CT} , arterio-venous delay W , and scaling factor SC were calculated by iterative deconvolution using Equations (2.10) and (2.11).

To relate E_{CT} of x-ray contrast agent to that of PET tracers, it is noted that the permeability surface area product of a permeable membrane to molecules is inversely proportional to their molecular weight. [16] Thus,

$$E_{av} = E_{CT} \sqrt{\frac{m_1}{m_2}} \quad (2.12)$$

Where m_1 and m_2 are the molecular weights of iopamidol (777.08 Da) and the PET tracer, respectively. For the case of FCH (157.6 Da), $E_{av} = 2.22E_{CT}$, and $k_{2av} = 2.22k_{2CT}$ since $k_{2av} = FE_{av}/Ve$. An additional case was simulated for a PET tracer with a higher extraction efficiency, where $E_{av} = 6.57E_{CT}$, which corresponds to a molecular weight of 18 Da (water). Molecules larger than 100 Daltons are related by a cubic root rather than the square root seen above. [17] However, Danielli's theoretical work suggests that for liquid medium, the square root relationship holds. [18] Therefore, we conservatively assumed a square root relationship since this results in a larger difference between the iopamidol and FCH extraction efficiencies.

With the parameters of the PET tracer transit time spectrum, $h_{av}(t)$, evaluated as above, the PET venous curve can be simulated by the following convolution:

$$C_v(t) = C_p(t) * h_{av}(t) \quad (2.13)$$

where $C_v(t)$ denotes the venous PET TAC, and $C_p(t)$ is the PET image derived arterial TAC from the iliac artery, and $h_{av}(t)$ is analogous to Equation (2.11) for the CT case, which gives:

$$C_v(t) = \begin{cases} 0 & 0 < t < W \\ (1 - E_{av})C_p(t - W) + k_{2av}E_{av} \int_0^{t-W} C_p(u)e^{-k_{2av}(t-W-u)} du & t \geq W \end{cases} \quad (2.14)$$

Note that the transit time spectrum used here was derived from the Johnson-Wilson model without a bound compartment, since the amount of tracer binding to targets in the forearm is negligible, given the quiescent nature of the forearm's muscles during the PET study.

2.2.3 Digital Phantom

Noise was added to the instantaneous arterial, venous and tissue TACs. Instantaneous activity measurements are based on the number of counts recorded by the PET scanner and hence these measurements will follow a Poisson distribution, given the intrinsic random nature of radioactive decay. The variance of Poisson noise is equal to the number of counts. However, this distribution is not sufficient to describe the noise in the image-derived TAC, since the PET scanner introduces other sources of noise and the data is reconstructed with a noise suppressing filter. This makes it impossible to know the variance at a discrete instantaneous time point. [19] Nevertheless, this work employs a noise model that is based on a Gaussian distribution. The decay of the radioisotope over the time course of the imaging study is also accounted for, assuming an ^{18}F labeled tracer. This model has previously been used by other investigators. [20, 21] Here, the only differences are notational. The noisy TAC is given by:

$$Q_n(t'_k) = ROI(t'_k) + G(0,1) \cdot \varepsilon \cdot \sqrt{ROI(t'_k)e^{\lambda t'_k}} \quad (2.15)$$

where t'_k is the midpoint time of the k^{th} acquisition frame, Q_n is the noisy activity concentration, $G(0,1)$ is a random number based on Gaussian distribution of zero mean and variance equal to one, ε is a scale factor that determines the magnitude of the noise, and λ is the decay constant of the radioisotope which is equal to $\ln(2)$ divided by its half-life. $ROI(t'_k)$ is the time-weighted average concentration for the k^{th} acquisition frame, such that:

$$ROI(t'_k) = \frac{1}{\Delta t_k} \int_{t_{k-1}}^{t_k} Q(t) dt \quad (2.16)$$

where $Q(t)$ is the instantaneous TAC, t_k is the endpoint of the k^{th} interval, and Δt_k is the length of the frame. The same procedure was used to obtain $C_{pn}(t'_k)$ and $C_{vn}(t'_k)$, which denote the noisy time-weighted average arterial and venous TACs, respectively.

Noise $\langle f_N^Q \rangle_{N,t}$ was quantified in the same manner as that used by Logan. [20]

$$\langle f_N^Q \rangle_{N,t} = avg \left\{ \frac{abs(Q_n(t) - Q(t))}{Q(t)} \right\} \quad (2.17)$$

where $Q(t)$ is the original data and $Q_n(t)$ is the noisy data. The average over all data points and all curves was taken.

The arterial and venous Logan methods were compared for a wide range of kinetic parameters. A digital phantom (Figure 2.2) was constructed consisting of 21 groups of parameter sets, covering three different k_4 values and seven F values. Each group consisted of a 7x7 grid where each square represented a unique kinetic parameter set, achieved by varying the parameters k_3 and V_e . Each square had a unique distribution volume,

determined by its unique parameter set. For the noisy case, each square of the grid contained 10x10 pixels for a total of 100 noise runs. An unpublished phantom study of our eXplore VISTA small animal PET scanner (GE Healthcare) showed a noise level equivalent to $\langle f_N^Q \rangle_{N,t} = 0.19$, therefore this digital phantom was constructed with this noise level to simulate a realistic case. In addition, two additional noise levels of $\langle f_N^Q \rangle_{N,t} = 0.11$ and $\langle f_N^Q \rangle_{N,t} = 0.29$ were simulated to cover a wider range of noise cases. All other model parameters were fixed (Table 2.1). For every parameter set, the true distribution volume was calculated as:

$$V_d = \frac{K_1}{k_2} \left(1 + \frac{k_3}{k_4} \right) + V_p \quad (2.18)$$

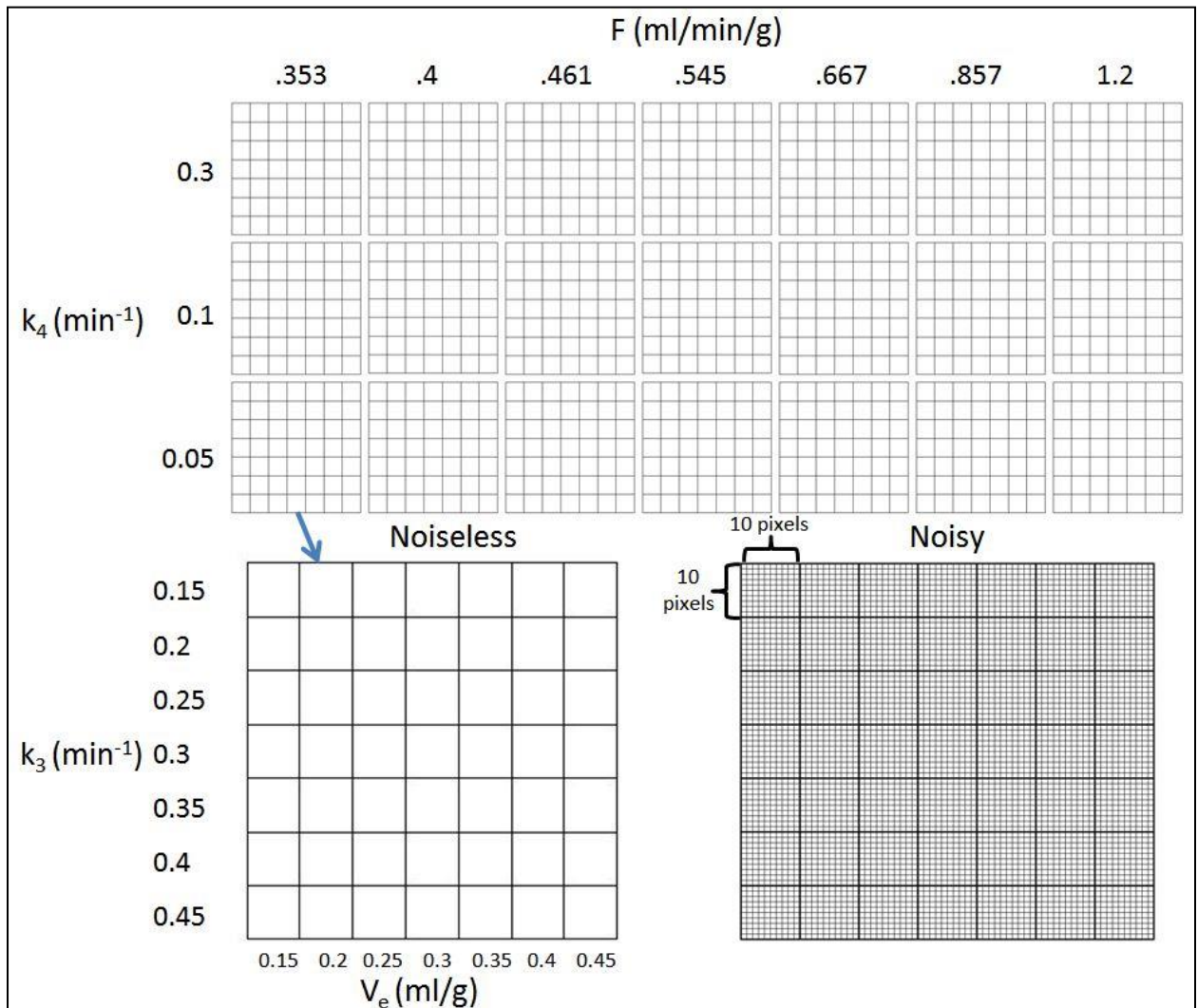


Figure 2.2: Digital phantom used to produce tissue TACs. The phantom is organized into 21 (three k_4 values x seven F values) groups of parameter sets. Each individual group consists of 49 (seven k_3 values x seven V_e values) unique parameter sets. In the noiseless case, each square on the grid represents a parameter set that produces a different tissue TAC and hence a different distribution volume. In the noisy case, each square (parameter set) is divided into a set of $10 \times 10 = 100$ pixels, each representing a unique noise case.

2.2.4 Logan Graphical Analysis

Graphical analysis was performed using the Logan method. [1] Keeping notation consistent with the Logan equation, which is a straight line of transformed tissue activity vs time, it can be written:

$$\frac{\sum_{k=1}^N Q_n(t'_k) \Delta t_k}{Q_n(t'_k)} = V_d \frac{\sum_{k=1}^N C_{pn}(t'_k) \Delta t_k}{Q_n(t'_k)} + I \quad (2.19)$$

where V_d is the slope, I is the intercept and k is the image frame number.

Logan plots were generated for Q_n with both 1) the arterial TAC C_{pn} and 2) the venous TAC C_{vn} . Linear regression was performed on the linear portion of the Logan plot to determine V_d , using the perpendicular regression method described by Varga and Szabo. [21]

An automated algorithm was developed to determine the linear portion of the Logan Plot. For a Logan curve with endpoint p_N , the radius of curvature r for points p_N , p_{N-1} , and p_{N-2} was calculated. This was done iteratively, by decreasing N by 1 at each iteration, until r differed from the previous calculation by more than 1%. The noisy case resulted in a Logan curve with bigger variations between data points, therefore the stopping criteria for all noisy cases was 50%. Once this stopping criterion was satisfied, the linear range for the Logan Plot was chosen to run from the most recent p_{N-1} to the last point of the curve.

2.2.5 Statistical Analysis

For each parameter set, the difference between arterial and venous Logan distribution volumes was calculated as a percentage difference: $[V_d(\text{arterial}) - V_d(\text{venous})] / V_d(\text{arterial}) \times 100$. For the noisy case, this difference represents a mean percentage difference over all 100 noise runs for that parameter set. Finally, the mean and standard deviations of the differences over all parameter sets were calculated for the given values of k_4 .

Linear regression was performed to compare Logan distribution volume measurements between the arterial and venous methods. Bland-Altman analysis [22] was used to assess the agreement between the arterial and venous methods. Since the difference between the arterial and venous methods depends on V_d , the percentage difference (instead of the absolute difference) was plotted against the mean of the two methods. [22]

2.3 Results

2.3.1 Simulated Venous Curves

The radial artery and median cubital vein TDCs are shown in Figure 2.3. The deconvolution between the two curves produced transit time spectrum parameter estimates of $E_{CT} = 3.8\%$, $k_{2CT} = 0.001 \text{ sec}^{-1}$, $W = 6 \text{ sec}$, and $SC = 0.457$. Translating this to the FCH PET case resulted in $E_{av} = 8.4\%$ and $k_{2av} = 0.0022 \text{ sec}^{-1}$. For the 18 Daltons PET tracer case, $E_{av} = 25\%$ and $k_{2av} = 0.0065 \text{ sec}^{-1}$.

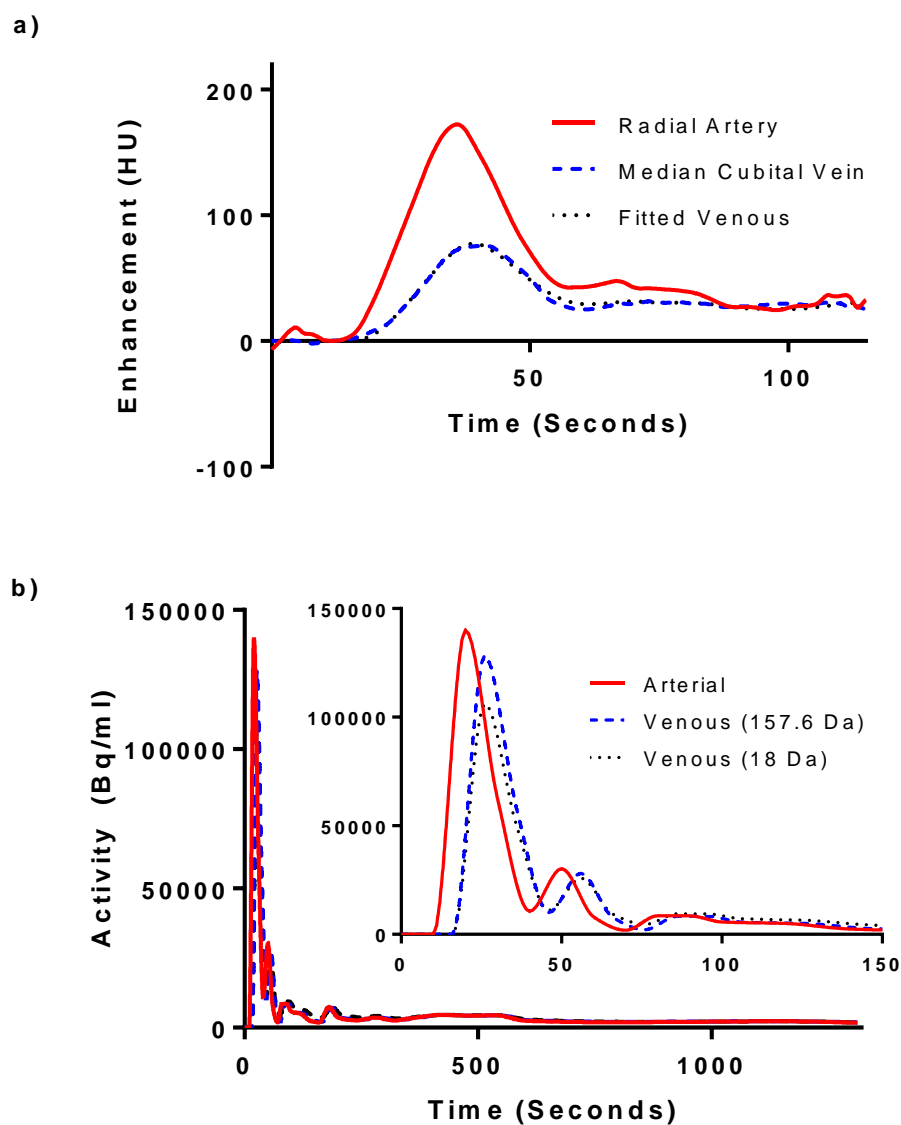


Figure 2.3: a) Measured radial artery along with measured and fitted median cubital vein TDCs from the DCE-CT forearm study. Curves were smoothed using a moving average filter. b) Measured FCH PET arterial TAC from the iliac artery along with simulated venous curves for PET tracers of 157.6 and 18 Daltons. The venous curves

were simulated based on the transit time spectrum measured with DCE-CT in the forearm which was transformed to the PET case based on the relationship between extraction efficiency and molecular weight.

2.3.2 Arterial and Venous Logan Analyses

The true distribution volumes for the $k_4 = 0.05 \text{ min}^{-1}$ case ranged from 0.4 to 6.4 ml/g. Qualitative results are shown for the noiseless case in Figure 2.4 and the noisy case in Figure 2.5. For the noiseless case of $E = 0.084$ (FCH), the mean percent difference \pm standard deviation between the arterial and venous graphical distribution volumes was $2.77 \pm 1.88\%$. For the noisy case of $\langle f_N^Q \rangle_{N,t} = 0.19$, the result was $-3.44 \pm 2.98\%$. For the largest extraction efficiency ($E_{av} = 25\%$) investigated, the result was $3.27 \pm 2.37\%$ and $4.33 \pm 10.2\%$ for the noiseless and $\langle f_N^Q \rangle_{N,t} = 0.19$ cases, respectively. Results for the remaining cases are outlined in Table 2.2. The mean percent difference was proportional to the extraction efficiency and decreased as k_4 increased.

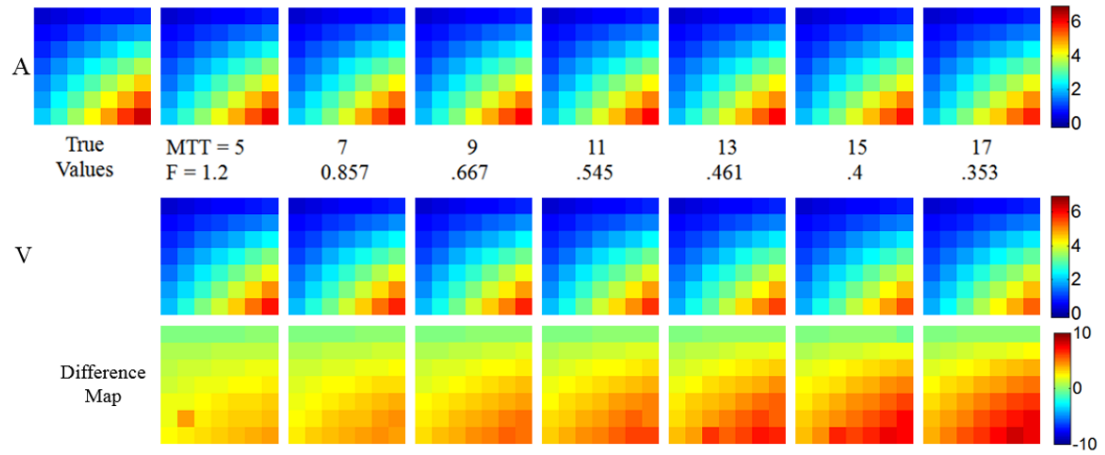


Figure 2.4: Results for $k_4 = 0.05 \text{ min}^{-1}$ and $E_{av} = 8.4\%$ (FCH) noiseless case. The first two rows show maps of the V_d 's calculated for the arterial (A) and venous (V) methods as well as the true V_d values in ml/g. The blood flow F is in ml/min/g and the vascular mean transit time MTT is in seconds. Difference maps show the percentage difference between the arterial and venous methods, with the arterial method as reference: $(\text{arterial} - \text{venous} / \text{arterial}) \times 100$.

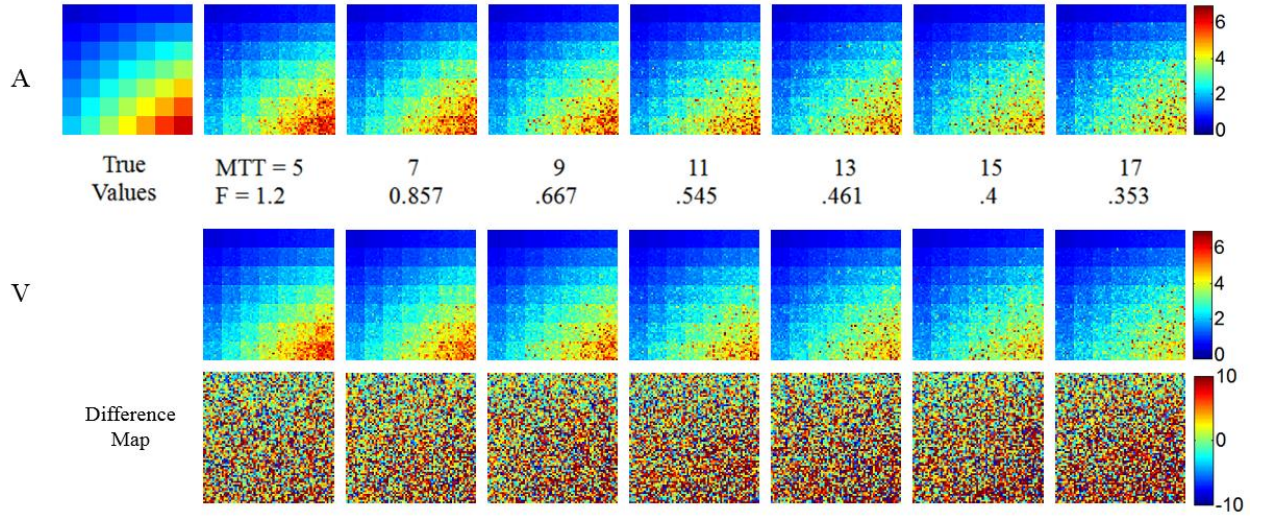


Figure 2.5: Results for the $k_4 = 0.05 \text{ min}^{-1}$ and $E = 8.4\%$ (FCH) noise case, with

$\langle f_N^Q \rangle_{N,t} = 0.19$. Setup is the same as in Figure 2.4.

Table 2.2: Mean percent differences for the Logan distribution volume measurements, shown as mean percent difference (SD) in %. For noisy cases, the difference was calculated as the mean percentage difference over all 100 runs of each parameter set. Values in this table represent the mean of the 343 (7 x 49) individual parameter set differences.

k_4 (min ⁻¹)	Mol. Weight (Da)	E_{av}	Noiseless	$\langle f_N^Q \rangle_{N,t}$ =0.11	$\langle f_N^Q \rangle_{N,t}$ =0.19	$\langle f_N^Q \rangle_{N,t}$ =0.29
0.05	157.6	8.4%	2.77 (1.88)	3.25 (1.69)	3.44 (2.98)	1.56 (26.3)
	18	25%	3.27 (2.37)	4.63 (1.71)	4.03 (10.2)	4.43 (15.8)
0.1	157.6	8.4%	0.86 (0.96)	1.57 (1.01)	1.47 (1.11)	1.54 (1.80)
	18	25%	0.92 (1.03)	2.93 (1.03)	2.83 (1.09)	2.79 (1.87)
0.3	157.6	8.4%	-0.49 (0.25)	0.15 (0.40)	0.15 (0.56)	0.07 (0.80)
	18	25%	-0.52 (0.27)	1.47 (0.36)	1.36 (0.54)	1.36 (0.71)

Linear regressions comparing V_d 's for both methods in the noiseless case resulted in fitted slopes with R^2 values close to unity. Bland-Altman analysis indicated good agreement between methods for all noiseless cases, with the majority of points falling within the 95% limits of agreement. (Figure 2.6) The limits of agreement were from -0.97% to 6.63%, -1.04% to 2.79% and -0.98 to 0% for $k_4 = 0.05, 0.1$ and 0.3 min⁻¹, respectively.

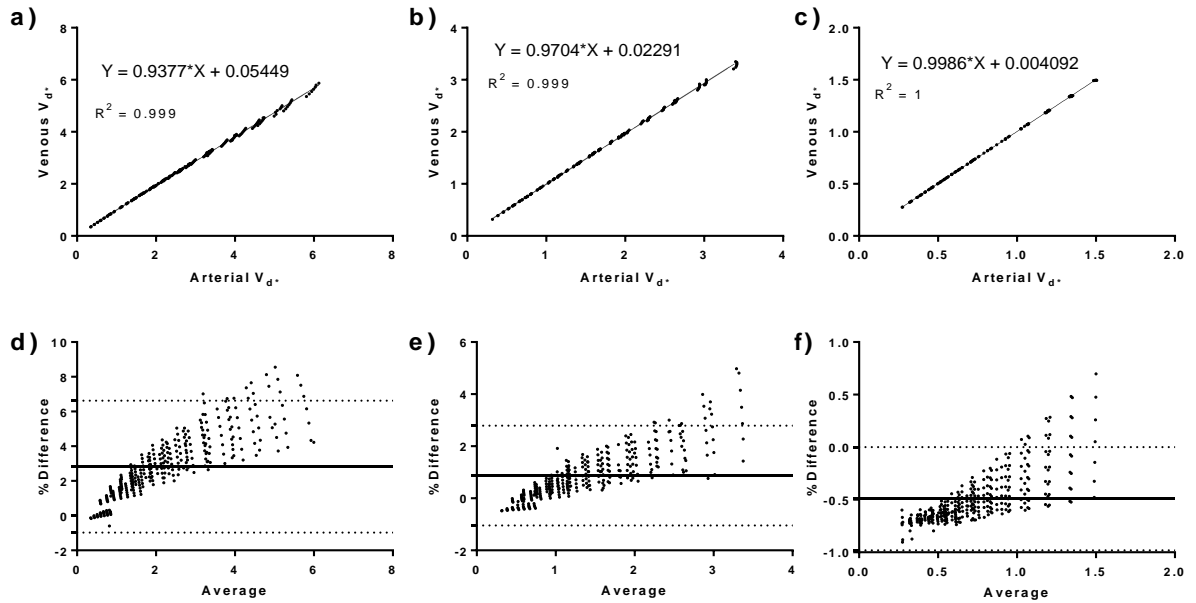


Figure 2.6: Noiseless case. (top) Linear regressions for the a) $k_4 = 0.05 \text{ min}^{-1}$, b) $k_4 = 0.1 \text{ min}^{-1}$ and c) $k_4 = 0.3 \text{ min}^{-1}$, $E = 8.4\%$ (FCH). (Bottom) Bland-Altman analyses, plotting % difference vs. average between V_d 's calculated with both methods for d) $k_4 = 0.05 \text{ min}^{-1}$, e) $k_4 = 0.1 \text{ min}^{-1}$ and f) $k_4 = 0.3 \text{ min}^{-1}$. The majority of the data points falls within the limits of agreement (± 1.96 SD of the mean), suggesting good agreement.

For the noisy case, the regression fit between the two methods had an R^2 of 0.99. On the Bland-Altman plot, the majority of the data points fell within the 95% limits of agreement, indicating good agreement. (Figure 2.7) The limits of agreement were from -0.76% to 7.56%, -0.72% to 3.70% and -0.96 to 1.25% for $k_4 = 0.05$, 0.1 and 0.3 min^{-1} , respectively.

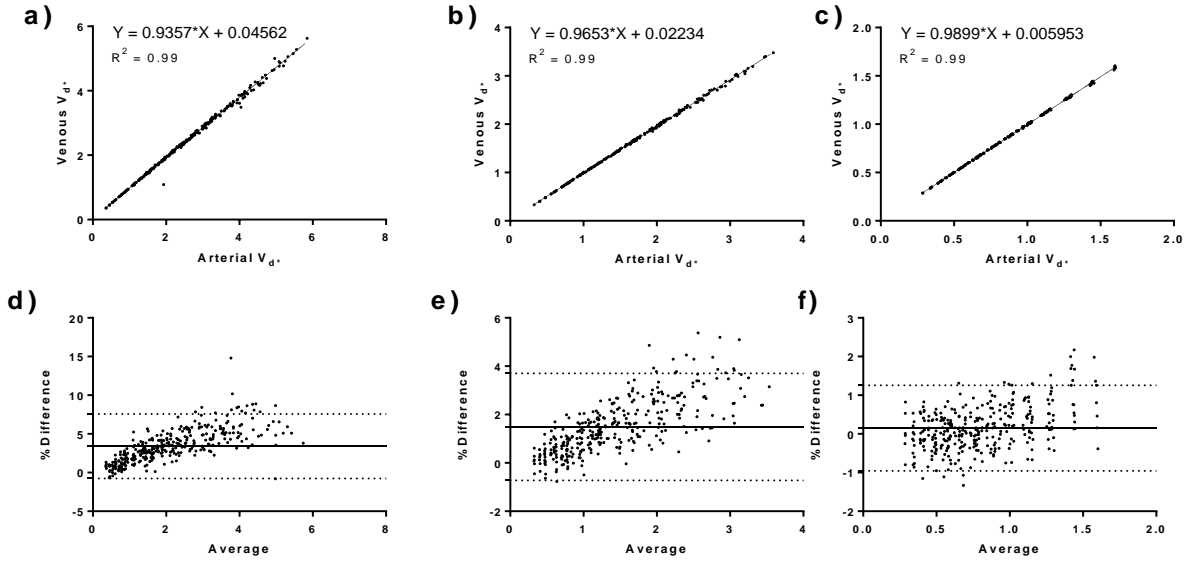


Figure 2.7: Noisy case, with $\langle f_N^Q \rangle_{N,t}$ equal to 0.19. (Top) Linear regressions for the a) $k_4 = 0.05 \text{ min}^{-1}$, b) $k_4 = 0.1 \text{ min}^{-1}$ and c) $k_4 = 0.3 \text{ min}^{-1}$. (Bottom) Bland-Altman analyses, plotting % difference vs. average between V_d 's calculated with both methods for d) $k_4 = 0.05 \text{ min}^{-1}$, e) $k_4 = 0.1 \text{ min}^{-1}$ and f) $k_4 = 0.3 \text{ min}^{-1}$, noisy cases. The majority of the data points falls within the limits of agreement (± 1.96 SD of the mean), suggesting good agreement.

2.4 Discussion

In the current study, our simulation demonstrates that the effects of arterial TAC dispersion on Logan distribution volume measurement are small. We simulated these effects over a range of different arterio-venous transit times and performed in-depth

analysis of different leakage rates into forearm tissue representative of both FCH and a theoretical tracer with higher extraction efficiency. Arterial blood sampling is typically performed from the radial artery and venous samples are usually obtained from a vein in the antecubital fossa. Given the similarity in shape between the arterial and venous TACs, especially at times beyond the recirculation phase, it can be inferred that the leakage from the blood vessel to the tissue in between the arterial and venous sampling sites is not significant for FCH. This is supported by the fitted arterio-venous transit time spectrum of contrast agent which has an extraction efficiency of 3.8%, which translates into an FCH extraction efficiency of $\sim 8\%$. Moreover, some of this tracer will travel back into the vasculature, further reducing the amount of tracer lost due to leakage as well as the total mean transit time through the tissue (equivalently, the area underneath $h_{av}(t)$.)

The results can be largely explained by the fact that the Logan Plot relies on the integral of the input TAC and is thus less sensitive to variations caused by dispersion. [23] This was also observed by Guo *et. al.* [24]. It follows that dispersion effects may be more noticeable in parameters estimated from kinetic modeling with compartment models.

The percentage difference between distribution volumes measured with the arterial and venous methods was proportional to the extraction efficiency of the PET tracer. In addition, this difference tended to increase as k_4 approached zero, which is expected given that the Logan graphical analysis is more accurate under equilibrium conditions and a small k_4 will increase the time it takes for this equilibrium to be achieved. Previous studies have shown that the magnitude of the bias in Logan graphical analysis V_d estimates is inversely proportional to k_4 . [25, 26]

Theoretically, each denominator in the Logan equation (2.19) is the instantaneous tissue TAC at the end-time of the respective time integral in the numerator. In practice, tissue TACs obtained from dynamic PET studies are averaged over the acquisition frame intervals. This simulation accounted for this effect by using an instantaneous arterial (input) TAC to first generate the corresponding instantaneous venous and tissue TACs with known parameters (hence known distribution volume) of the three-compartment model. Frame averaging as in dynamic PET imaging was then applied to the tissue TACs prior to distribution volume calculation with the Logan Plot as implemented in Equation (2.19). The fact that in the noise free case, the ‘true’ distribution volume was recovered in each simulated case suggests that the modified Logan analysis has minimal effect on the accuracy of the calculated distribution volume.

One of the noise cases investigated here had a signal-to-noise ratio (SNR) of roughly 6 to 1, corresponding to $\langle f_N^Q \rangle_{N,t} = 0.19$. This is consistent with the SNR observed in one of our unpublished phantom studies of the GE Healthcare eXplore VISTA Dual-Ring Small Animal PET Scanner. However, the SNR is dependent upon a number of factors, including scanner characteristics and the type of image reconstruction algorithm that is used. [27] Hartung-Knemeyer *et. al.* found the mean SNR of a clinical scanner to be between 2.6 and 3.6, which is approximated by the $\langle f_N^Q \rangle_{N,t} = 0.29$ in our study. [28]

The applicability of this simulated dispersion to other tracers depends on the tracer’s molecular weight (and hence extraction efficiency) and is highly dependent on that tracer’s uptake in muscle, since this study assumed negligible uptake into tissue between the arterial and venous sampling sites. This study investigated FCH, which has generally

low uptake in muscle [29], especially when compared to the peak activity of the arterial TAC. For FDG, muscle uptake in the forearm appears to be dependent on the amount of muscle exertion prior to the PET scan [30], therefore this may be an important factor to consider. Regardless, the use of venous blood samples for Logan Analysis with different tracers must be validated in future human patient studies.

This study has some limitations. The simulation used an automated algorithm to define the linear region of the Logan Plot, and this algorithm may be highly susceptible to noise effects by adding error to the calculation of the radius of curvature. This is a possible explanation for the presence of the outlier data points in Figure 2.7. Despite this added source of error, the agreement was good between the two methods for the noisy case. It is worth noting that in scenarios where mean TACs from a region of interest are being used, the user would likely manually specify the linear range of the Logan Plot and would therefore avoid any errors resulting from the use of an automated algorithm. Another limitation is that the venous TDC measured from DCE-CT was taken from a vein in proximity to the radial artery rather than the median cubital vein. This was done because the median cubital vein has a very small diameter and was difficult to distinguish in the images. However, given the short distance between the venous ROI and the median cubital vein, we have no reason to believe that the differences in mean transit time and extraction efficiency between these two locations would have any significant effect on the conclusions of this study. Finally, further studies are required in order to evaluate whether the conclusions of this simulation are applicable *in vivo*.

2.5 Conclusions

Our simulations suggest that venous blood sampling may be a feasible alternative to arterial blood sampling for measurement of the distribution volume with the Logan Plot for the range of kinetic parameters that were simulated. The use of venous blood samples for this purpose must be clinically validated in future research. For quantitative dynamic PET studies, this method has the potential to reduce patient discomfort and greatly reduce the risks that are typically associated with arterial cannulation.

2.6 References

1. Logan, J., *Graphical analysis of PET data applied to reversible and irreversible tracers*. Nucl Med Biol, 2000. **27**(7): p. 661-70.
2. Innis, R.B., et al., *Consensus nomenclature for in vivo imaging of reversibly binding radioligands*. J Cereb Blood Flow Metab, 2007. **27**(9): p. 1533-9.
3. Erlandsson, K., et al., *A review of partial volume correction techniques for emission tomography and their applications in neurology, cardiology and oncology*. Phys Med Biol, 2012. **57**(21): p. R119-59.
4. Wilkins, R.G., *Radial artery cannulation and ischaemic damage: a review*. Anaesthesia, 1985. **40**(9): p. 896-9.
5. Slogoff, S., A.S. Keats, and C. Arlund, *On the safety of radial artery cannulation*. Anesthesiology, 1983. **59**(1): p. 42-7.
6. Mandel, M.A. and P.J. Dauchot, *Radial artery cannulation in 1,000 patients: precautions and complications*. J Hand Surg Am, 1977. **2**(6): p. 482-5.
7. Wallach, S.G., *Cannulation Injury of the Radial Artery: Diagnosis and Treatment Algorithm*. American Journal of Critical Care, 2004. **13**(4): p. 315-319.
8. Durbin, C.G., Jr., *Radial arterial lines and sticks: what are the risks?* Respir Care, 2001. **46**(3): p. 229-31.
9. van der Weerdt, A.P., et al., *Use of arterialised venous instead of arterial blood for measurement of myocardial glucose metabolism during euglycaemic-hyperinsulinaemic clamping*. Eur J Nucl Med Mol Imaging, 2002. **29**(5): p. 663-9.
10. Takagi, S., et al., *Quantitative PET cerebral glucose metabolism estimates using a single non-arterialized venous-blood sample*. Ann Nucl Med, 2004. **18**(4): p. 297-302.
11. Ng, Y., et al., *Equivalence of arterial and venous blood for [¹¹C]CO₂-metabolite analysis following intravenous administration of 1-[¹¹C]acetate and 1-[¹¹C]palmitate*. Nucl Med Biol, 2013. **40**(3): p. 361-5.

12. Hahn, A., et al., *Combining image-derived and venous input functions enables quantification of serotonin-1A receptors with [carbonyl-11C]WAY-100635 independent of arterial sampling*. Neuroimage, 2012. **62**(1): p. 199-206.
13. Ayappa, I., et al., *Arterial, capillary, and venous transit times and dispersion measured in isolated rabbit lungs*. J Appl Physiol (1985), 1995. **79**(1): p. 261-9.
14. Lee, T.Y., T.G. Purdie, and E. Stewart, *CT imaging of angiogenesis*. Q J Nucl Med, 2003. **47**(3): p. 171-87.
15. Meier, P. and K.L. Zierler, *On the theory of the indicator-dilution method for measurement of blood flow and volume*. J Appl Physiol, 1954. **6**(12): p. 731-44.
16. Davson, J. and J. Danielli, *The Permeability of Natural Membranes*. 1943, Cambridge: Cambridge University Press.
17. Nystrom, R., *Membrane Physiology*. 1976: Prentice-Hall.
18. Danielli, J.F., *Theory of penetration of a thin membrane, Appendix A*, in *The Permeability of Natural Membranes (Theory of penetration of a thin membrane, Appendix A)*. 1952, University Press: Cambridge.
19. Budinger, T.F., et al., *Quantitative potentials of dynamic emission computed tomography*. J Nucl Med, 1978. **19**(3): p. 309-15.
20. Logan, J., et al., *A strategy for removing the bias in the graphical analysis method*. J Cereb Blood Flow Metab, 2001. **21**(3): p. 307-20.
21. Varga, J. and Z. Szabo, *Modified regression model for the Logan plot*. J Cereb Blood Flow Metab, 2002. **22**(2): p. 240-4.
22. Bland, J.M. and D.G. Altman, *Measuring agreement in method comparison studies*. Stat Methods Med Res, 1999. **8**(2): p. 135-60.
23. Zanotti-Fregonara, P., et al., *Image-derived input function for brain PET studies: many challenges and few opportunities*. J Cereb Blood Flow Metab, 2011. **31**(10): p. 1986-98.
24. Guo, H., R.A. Renaut, and K. Chen, *An input function estimation method for FDG-PET human brain studies*. Nucl Med Biol, 2007. **34**(5): p. 483-92.

25. Guo, H., et al., *Reducing modeling error of graphical methods for estimating volume of distribution measurements in PIB-PET study*. Mathematical Biosciences, 2010. **226**(2): p. 134-146.
26. Price, J.C., et al., *Kinetic modeling of amyloid binding in humans using PET imaging and Pittsburgh Compound-B*. J Cereb Blood Flow Metab, 2005. **25**(11): p. 1528-1547.
27. Teymurazyan, A., et al., *Properties of noise in positron emission tomography images reconstructed with filtered-backprojection and row-action maximum likelihood algorithm*. J Digit Imaging, 2013. **26**(3): p. 447-56.
28. Hartung-Knemeyer, V., et al., *Optimizing positron emission tomography image acquisition protocols in integrated positron emission tomography/magnetic resonance imaging*. Invest Radiol, 2013. **48**(5): p. 290-4.
29. Verwer, E.E., et al., *Quantification of 18F-fluorocholine kinetics in patients with prostate cancer*. J Nucl Med, 2015. **56**(3): p. 365-71.
30. Jackson, R.S., et al., *Prevalence and Patterns of Physiologic Muscle Uptake Detected with Whole-Body 18F-FDG PET*. Journal of Nuclear Medicine Technology, 2006. **34**(1): p. 29-33.

Chapter 3

3 Noise Study of Linear and Non-Linear Solutions of a DCE-CT/PET Hybrid Imaging Technique

3.1 Introduction

Positron emission tomography (PET) allows for quantitative imaging of biochemical processes and can provide functional, metabolic or molecular information in imaging of diseases, e.g. cancer and neurodegeneration, involving different body organs [1, 2]. In these imaging applications, a non-pharmacological dose of a specific radiolabeled molecule of interest (tracer) is injected into the patient and a static or dynamic acquisition is performed to measure tissue tracer uptake at a fixed time after injection or as a function of time or time-activity curves. The one-time uptake or time-activity curve is then used to assess the rate of tracer binding to targets which can in turn be used to infer the activity of specific functional, metabolic or molecular processes in tissue.

The simplest and most common analysis metric used in PET is the standard uptake value (SUV) which normalizes the measured activity in a given region to the dose injected and the patient's weight [3]. The SUV is a semi-quantitative metric because it is not a pure measure of the tracer-target binding rate. While it does account for target bound tracer, it also includes free unbound tracer present in the vasculature and in the interstitial space (tissue water) which confounds the measurement of the target binding rate. It also fails to account for the effect of tracer delivery via tissue blood flow, which may make inter-patient comparisons [3] and longitudinal comparisons within a single patient difficult if blood flow is different between subjects or changes over time in the same patient. [4] The SUV is

commonly used clinically as it does not require complicated tracer kinetic (e.g. compartmental) analysis which would require arterial blood sampling to measure the arterial tracer concentration curve over time. However, given its limitations, its use is generally discouraged for multicenter trials [5].

Quantitative measurement of the tracer-target binding rate is possible with the use of compartment models such as the 3-compartment model [6]. These models describe the different processes, represented by rate constants, involved in the distribution of the tracer into different tissue compartments: blood plasma, tissue water and bound target pool. Estimating the model rate constants would typically involve fitting of the measured tissue time activity curve (TAC) to a model in which the arterial TAC serves as the model's input. However, reproducible estimates of these model rate constants are difficult to obtain due to the covariances among them. For example, Slaets et. al. [7] found high variability of rate constant estimates using a 3 compartment (two tissue) model of FCH in nude mice and Muzi et. al. [8] found high covariance between rate constants using the same compartment model in an analysis of FLT uptake in glioma patients.

One way of dealing with model parameter variance is to estimate composite parameters that are functions of the basic model rate constants. Examples of composite parameters include the influx constant K_i and the distribution volume V_d , which can also be measured using a Patlak plot and a Logan plot, respectively [9, 10]. Another example is in the study of Muzi et. al., where the model was reparametrized to measure the composite parameter K_1/k_2 instead of estimating K_1 and k_2 individually [8]. The trade-off of this approach is that a composite parameter is a function of multiple model rate constants.

Frequently, the rate constants included in the composite parameter's functional definition are related to blood flow and blood volume in the local vasculature. Therefore, the improvement in reproducibility of the composite parameter is to a certain extent offset by the implicit dependence on other model rate constant(s).

It may be possible to reduce the variability resulting from parameter covariance by reducing the number of estimated parameters (model rate constants). This could be done by measuring a subset of parameters by means of a different imaging modality that is better in terms of accuracy and precision at measuring these parameters and then incorporating those parameter values into the compartment model of interest, effectively reducing the number of parameters to be estimated. This approach can be implemented with relative ease using PET/CT scanners. Using these scanners, a dynamic contrast enhanced CT (DCE-CT or CT Perfusion) study can be performed which is automatically registered with the dynamic PET study either before or after the DCE-CT study. In a DCE-CT study, an iodinated, inert (does not bind to tissue targets) contrast agent is injected into the patient and dynamic CT scanning of the tissue is used to measure the tissue time-density curve (TDC) which is a record of the accumulation and wash-out of contrast in the plasma and tissue water compartment, driven by blood flow, over time. CT Perfusion software (GE Healthcare) is then used to analyze the tissue TDC with respect to the arterial TDC to estimate blood flow, blood volume and flow extraction product of the PET tracer and hence the influx and efflux rate constant of tracer between the plasma and tissue water compartment, which can be related using a scaling factor to account for differences in molecular weight between the CT contrast agent and PET tracer [11]. The influx and efflux

rate constant could be incorporated into the PET tracer model to reduce the number of parameters to be estimated and hence reduce covariance among or increase the reproducibility of the remaining parameters. This hybrid DCE-CT/PET imaging technique is the subject of this work.

Non-linear optimization techniques are often used to fit the PET model curve to the measured PET TAC. Another potential disadvantage to compartment modeling is the lengthy computation time taken to estimate the model rate constants with non-linear optimization techniques. In certain clinical settings, it may be desirable to create functional maps of the model rate constants. For a dynamic PET study using 128x128 image format there are over 10,000 non-linear curve fits, which would take several hours to compute. Linear solutions of the 3-compartment model have been developed which permit much faster computation of curve fits [12, 13]. Making use of these linear solutions alongside the hybrid DCE-CT/PET imaging technique may allow for rapid generation of functional parametric maps of the target binding rate constant. This work simulates the use of PET/CT scanning and a linearized solution of the 3-compartment model to investigate the effect of TAC noise on the bias and variation of the estimated target binding rate constant from the 3-compartment model.

3.2 Methods

3.2.1 Generation of Simulated Tissue Time Activity Curves

The 3-compartment model was used to represent the uptake of bound tracer in tissue (Figure 3.1). The equations governing the model are the following:

$$\frac{dC_i}{dt} = K_1 C_a(t) - (k_2 + k_3) C_i(t) + k_4 C_m(t) \quad (1)$$

$$\frac{dC_m}{dt} = k_3 C_i(t) - k_4 C_m(t) \quad (2)$$

$$Q(t) = V_b C_a(t) + C_i(t) + C_m(t) \quad (3)$$

where $C_a(t)$ is the arterial TAC, $C_i(t)$ is the interstitial concentration of free tracer, K_1 is the influx rate constant in min^{-1} , k_2 is the efflux rate constant for the return of tracer from the interstitial space back into blood vessels, k_3 is the binding rate constant in tissue, k_4 is the dissociation rate constant, $C_m(t)$ is the concentration of bound tracer and $Q(t)$ is the tissue TAC. The non-linear solution of $Q(t)$ from these equations is

$$Q(t) = V_b C_a(t) + C_a(t) * [G e^{-\alpha t} + H e^{-\beta t}] \quad (4)$$

where $*$ denotes the convolution operator. G , H , α , and β are defined as:

$$\alpha = \frac{k_2 + k_3 + k_4 + \sqrt{(k_2 + k_3 + k_4)^2 - 4k_2 k_4}}{2} \quad (5)$$

$$\beta = \frac{k_2 + k_3 + k_4 - \sqrt{(k_2 + k_3 + k_4)^2 - 4k_2 k_4}}{2} \quad (6)$$

$$G = K_1 \frac{(k_3 + k_4 - \alpha)}{(\beta - \alpha)} \quad (7)$$

$$H = K_1 \frac{(\beta - k_3 - k_4)}{(\beta - \alpha)} \quad (8)$$

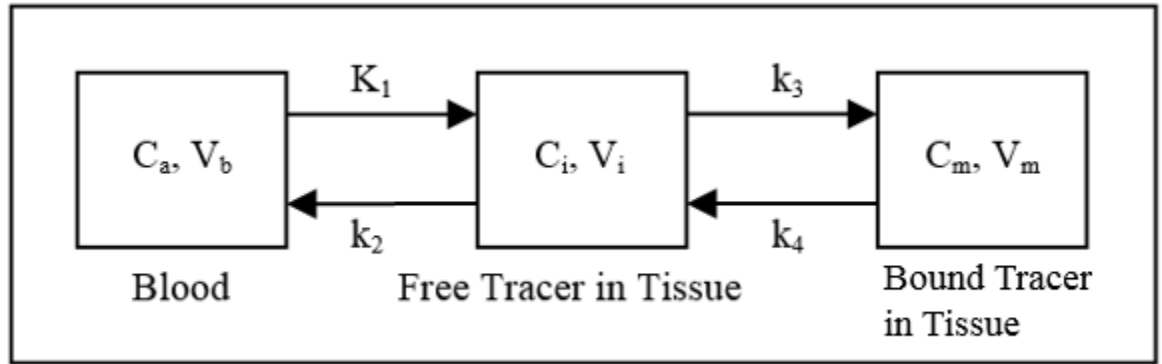


Figure 3.1: The 3-Compartment kinetic model of tracer uptake in tissue.

A simulated tissue TAC was generated by convolving the arterial TAC with the impulse response function of the kinetic model. This was accomplished with the use of JSim software. [14] The model parameters used to simulate the tissue curve were based on measurements in a mouse study with the tracer ^{18}F -fluorocholine which is phosphorylated by choline kinase and becomes trapped in the cell membrane.

An athymic nude mouse was injected with PC-3 human prostate cancer cells and the tumor was imaged at day 54 (post-injection). Dynamic ^{18}F -Fluorocholine PET scanning was performed on a GE Healthcare eXplore VISTA dual-ring small-animal PET scanner. Data was acquired in list mode and images were reconstructed using the ordered subset expectation maximization algorithm.

Images were binned into acquisition frames of 8 x 15 s, 9 x 60 s, 10 x 120 s, and 6 x 300 s for a total scan time of one hour. An image-derived arterial TAC was used for kinetic analysis, which was obtained from a region of interest (ROI) in the left ventricle cavity. The TAC was corrected for metabolites based on the method of Slaets *et. al.* [7].

The mouse tumour was segmented and the mean TAC was obtained from this ROI. Fitting was performed by using the non-linear trust-region-reflective algorithm in MATLAB [15, 16]. The parameters obtained were used to generate the simulated tissue curve (Table 3.1). The fit of the tissue TAC is shown in Figure 3.2.

Table 3.1: Parameters obtained from fitting of mean ROI TAC in a PC-3 mouse tumour.

V_b (ml/g)	K_1 (ml/min/g)	k_2 (min ⁻¹)	k_3 (min ⁻¹)	k_4 (min ⁻¹)
0	0.12	0.56	0.23	0.03

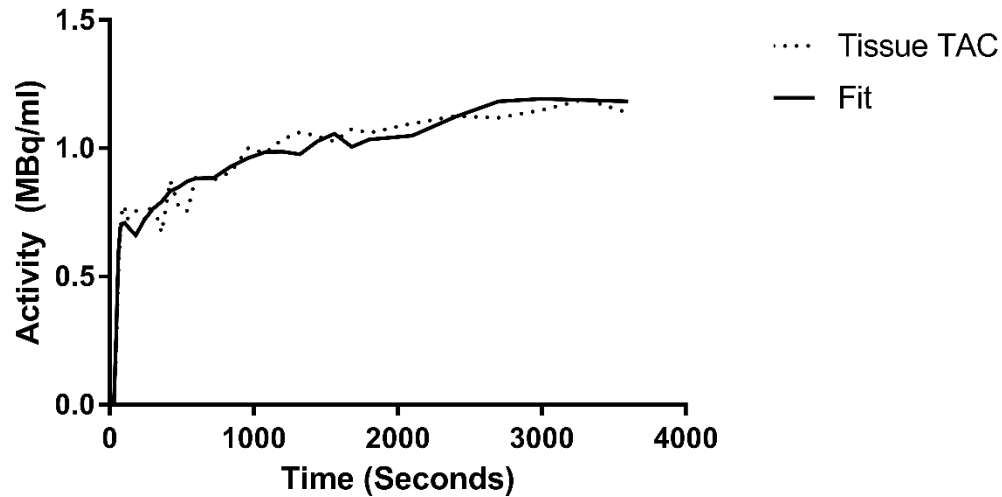


Figure 3.2: Fit of the tumour tissue TAC of a PC-3 mouse model to obtain parameters for the simulated TACs.

3.2.2 Linear Solutions of 3-Compartment Model

With the use of the Laplace transform, the solution of the 3-compartment model can be written in a linearized form:

$$\begin{aligned}
Q(t) = & V_b [C_a(t)] - P_1 \left[\int_0^t Q(u) du \right] - P_2 \left[\int_0^t \int_0^T Q(u) du dT \right] + P_3^* \left[\int_0^t C_a(u) du \right] \dots \\
& + P_4^* \left[\int_0^t \int_0^T C_a(u) du dT \right]
\end{aligned} \tag{9}$$

where the coefficients V_b , P_1 , P_2 , P_3^* , and P_4^* can be solved for using a non-negative least squares (NNLS) [17] algorithm by constructing a system of linear equations where there is one equation for each time point of $Q(t)$. The rate constants can be calculated as $K_1 = P_3$, $k_2 = P_1 - (P_4/P_3)$, $k_4 = P_2/k_2$, and $k_3 = P_1 - k_2 - k_4$, where $P_3 = P_3^* - P_1 V_b$ and $P_4 = P_4^* - P_2 V_b$. This formulation is outlined by Feng et. al. [12] and similar to the linear least squares solution developed by Blomqvist [13] for the irreversible 3-compartment model.

This model was simplified to the case of $V_b=0$ given the finding that the smallest sum of squared deviations fit in a mouse tumor produced a value of zero for this parameter. This is consistent with an assumption made in another kinetic modeling study of FCH in mice [7] as well as observations by other investigators that FCH has extremely rapid uptake relative to PET frame length. [18, 19]

Equation (9) served as the foundation from which all other linearized model solutions were developed in this study. These models assume a V_b of zero and some models include parameters known a priori from CT Perfusion functional maps. The different models are outlined in Table 3.2.

Table 3.2: Linearized solutions of the 3-Compartment model assuming zero blood volume. Some models assume known parameters from CT Perfusion functional maps. Coefficients of the linearized solutions were solved for using a non-negative least squares algorithm in Matlab and rate constants were calculated from the coefficients. Constraints were used to prevent negative rate constants.

Model Name	3C-LIN
Known Parameters from CT Perfusion	None
Estimated Parameters	K_1, k_2, k_3, k_4
Linearized Equation	$Q(t) = -P_1 \left[\int_0^t Q(u) du \right] - P_2 \left[\int_0^t \int_0^T Q(u) dudT \right] + P_3 \left[\int_0^t C_a(u) du \right] \dots$ $+ P_4 \left[\int_0^t \int_0^T C_a(u) dudT \right]$
Constraints	$P_1 \geq P_4$
Coefficients	$P_1 = k_2 + k_3 + k_4$ $P_2 = k_2 k_4$ $P_3 = K_1$ $P_4 = K_1(k_3 + k_4)$
Rate Constant Equations	$K_1 = P_3$ $k_2 = P_1 - (P_4/P_3)$ $k_4 = P_2/k_2$ $k_3 = P_1 - k_2 - k_4$
Model Name	3C-LIN-K1
Known Parameters from CT Perfusion	K_1
Estimated Parameters	k_2, k_3, k_4
Linearized Equation	$Q(t) - K_1 \int_0^t C_a(u) du = -P_1 \left[\int_0^t Q(u) du \right] - P_2 \left[\int_0^t \int_0^T Q(u) dudT \right] + P_4 \left[K_1 \int_0^t \int_0^T C_a(u) dudT \right]$
Constraints	$P_1 \geq P_4$
Coefficients	$P_1 = k_2 + k_3 + k_4$

	$P_2 = k_2 k_4$ $P_4 = k_3 + k_4$
Rate Constant Equations	$k_2 = P_1 - P_4$ $k_4 = P_2 / k_2$ $k_3 = P_4 - k_4$
Model Name	<i>3C-LIN-K1K2</i>
Known Parameters from CT Perfusion	K_1, k_2
Estimated Parameters	k_3, k_4
Linearized Equation	$Q(t) - K_1 \int_0^t C_a(u) du + k_2 \int_0^t Q(u) du = P_1 \left[K_1 \int_0^t \int_0^T C_a(u) du dT - \int_0^t Q(u) du \right] \dots$ $- P_2 \left[k_2 \int_0^t \int_0^T Q(u) du dT \right]$
Constraints	$P_1 \geq P_2$
Coefficients	$P_1 = k_3 + k_4$ $P_2 = k_4$
Rate Constant Equations	$k_4 = P_2$ $k_3 = P_1 - P_2$

3.2.3 Non-Linear Solutions of 3-Compartment Model

The non-linear solution of the 3C model was performed by using the non-linear trust-region-reflective algorithm in MATLAB 2015b [15, 16] to fit Equation (4) (with no blood volume term). Different sets of initial values for the model parameters were used. (Table 3.3) The set that led to a fit with the smallest sum of squared deviations (SSD) was accepted as the final (optimal) fit.

Table 3.3: Initial parameter sets and constraints used for the non-linear fitting of the tissue TACs.

Parameter	Starting Values				Lower Bound	Upper Bound
	Set 1	Set 2	Set 3	Set 4		
K_1 (ml/min/g)	0.01	1.00	0.5	0.2	0	1
k_2 (min ⁻¹)	0.01	1.00	0.5	0.3	0	1
k_3 (min ⁻¹)	0.01	1.00	0.5	0.25	0	1
k_4 (min ⁻¹)	0.01	1.00	0.5	0.01	0	1

The absence of the LIN identifier in the model name represents the non-linear solution of that model. Hence, the non-linear models are 3C, 3C-K1, and 3C-K1K2. In models where some parameters are assumed to be known a priori from CT Perfusion, those parameters were held fixed in the fitting procedure.

3.2.4 Sensitivity Analysis

The TAC values measured at different time points of an imaging study can be described using the compartment model above. To robustly estimate a parameter, the TAC must be sensitive to changes in the parameter value during some time interval of the study. Sensitivity analysis produces time-dependent sensitivity functions for each parameter that indicate the response of the TAC to perturbations in parameter values. This analysis can be carried out numerically or analytically.

The numerical method involves altering a given parameter by a small value (say 1%) and calculating the change in the model TAC, $Q(t)$ for each time point in the study. This is the method of finite differences. The sensitivity function for a given parameter P is given by

$$S(t, P_i) = \frac{\delta Q(t, P_i)}{\delta P_i} = \frac{Q(t, P_0) - Q(t, P_0 + \Delta)}{\Delta} \quad (10)$$

where P_0 is the value of parameter P_i and Δ is equal to 1% of P_0 . For an experiment with N time points and M parameters, the $N \times M$ sensitivity matrix \mathbf{S} is then constructed:

$$\mathbf{S} = \begin{bmatrix} S(t_1, P_1) & S(t_1, P_2) & \dots & S(t_1, P_M) \\ S(t_2, P_1) & S(t_2, P_2) & \dots & S(t_2, P_M) \\ \vdots & \vdots & \dots & \vdots \\ S(t_{N-1}, P_1) & S(t_{N-1}, P_2) & \dots & S(t_{N-1}, P_M) \\ S(t_N, P_1) & S(t_N, P_2) & \dots & S(t_N, P_M) \end{bmatrix} \quad (11)$$

In order to compare the effect of different parameters on the model solution, $S(t, P_i)$ was normalized such that

$$S_N(t, P_i) = S(t, P_i) \cdot \frac{P_0}{Q(t)} \quad (12)$$

The analytical method involves the determination of the sensitivity matrix \mathbf{S} in which each column is the partial derivative of the model solution taken with respect to a model parameter. For the 3-compartment model and a tissue TAC with N time points, \mathbf{S} is given by

$$\mathbf{S} = \begin{bmatrix} \frac{\partial Q(t_1)}{\partial K_1} & \cdots & \frac{\partial Q(t_1)}{\partial k_4} \\ \vdots & \cdots & \vdots \\ \frac{\partial Q(t_{N-1})}{\partial K_1} & \cdots & \frac{\partial Q(t_{N-1})}{\partial k_4} \\ \frac{\partial Q(t_N)}{\partial K_1} & \cdots & \frac{\partial Q(t_N)}{\partial k_4} \end{bmatrix} \quad (13)$$

The partial derivatives are not defined here, for brevity.

In this work, JSim software [14] was used to perform sensitivity analysis. It uses the numerical method of finite differences. The sensitivity matrix obtained numerically from equation (11) was used to calculate the covariance and correlation matrices (Section 3.2.5). The normalized sensitivity functions from (12) were plotted versus time for each parameter. The sensitivity functions obtained via the numerical and analytical methods were compared to verify agreement.

3.2.5 Identifiability Analysis

While the TAC must be sensitive to a parameter in order to estimate it, this property alone does not guarantee robust estimates. Identifiability tells us whether a parameter can be estimated without the variance being large and without being confounded by other model parameters by examining the correlations among the parameters. If two parameters are highly correlated, then it is difficult to estimate each parameter independently because similar perturbations in those parameters would produce similar responses in the TAC. This reduces the reliability of those parameter estimates. The Fisher information matrix, \mathbf{F} , which gives the variances and covariances of the model parameters, has elements

$$F_{ij} = \sum_t \frac{1}{\sigma^2} \frac{\delta Q(t)}{\delta P_i} \frac{\delta Q(t)}{\delta P_j} \quad (14)$$

Where i and j go from 1 to M parameters and σ^2 is the estimate of the noise variance in the measured TAC which is fitted by the model solution. F is an $M \times M$ symmetric matrix. Based on the previous definition of S , it follows that the Fisher matrix can be expressed in terms of the sensitivity matrix as

$$F = \frac{1}{\sigma^2} [S' S] \quad (15)$$

where S' is the transpose of S . Inverting F gives the covariance matrix V : [20]

$$V = F^{-1} = \sigma^2 \cdot [S' S]^{-1} \quad (16)$$

The lower bound of the variance of the parameter estimates, the Cramér-Rao bound [21, 22], is represented by the diagonal matrix elements of V . The lower bound of the coefficient of variation (COV) was calculated for each parameter by first taking the square root of these diagonal elements (equal to the standard deviation for each parameter) and then dividing those by the true parameter value. The covariance matrix was converted to the correlation matrix C by dividing each element by the square root of the product of the corresponding diagonal elements:

$$C_{ij} = \frac{V_{ij}}{\sqrt{V_{ii} \cdot V_{jj}}} \quad (17)$$

In this work, noise in the measured TAC is assumed to follow a Gaussian distribution with a variance of σ^2 (note that a Poisson distribution with mean > 15 can be closely approximated by a Gaussian distribution).

3.2.6 Simulating PET Frames

Data from dynamic PET acquisitions are binned into image frames of varying temporal length. The noise-free activity for a PET frame is determined by integrating the activity over the length of the PET frame and dividing by the length of the frame: [23]

$$C_a(t_k) = \frac{1}{\Delta t_i} \int_{t_{i-1}}^{t_i} C_{inst}(T) dT \quad (18)$$

Where $C_{inst}(t)$ is the instantaneous TAC, $C_a(t_k)$ is the TAC averaged over the PET frame, t_{i-1} is the start time of the i^{th} frame, t_i is the end time of the i^{th} frame, $\Delta t_i = t_i - t_{i-1}$ is the length of the frame and t_k is the midpoint of the i^{th} frame ($t_i = t_i - \Delta t_i/2$).

The instantaneous arterial TAC and the simulated instantaneous tissue TAC were averaged according to the above equation. The image bins used for the simulation were as follows: 8 x 15 s, 9 x 60 s, 10 x 120 s, and 6 x 300 s. (Figure 3.3) All simulations in this work used the time averaged arterial and tissue TACs as shown in equation (18).

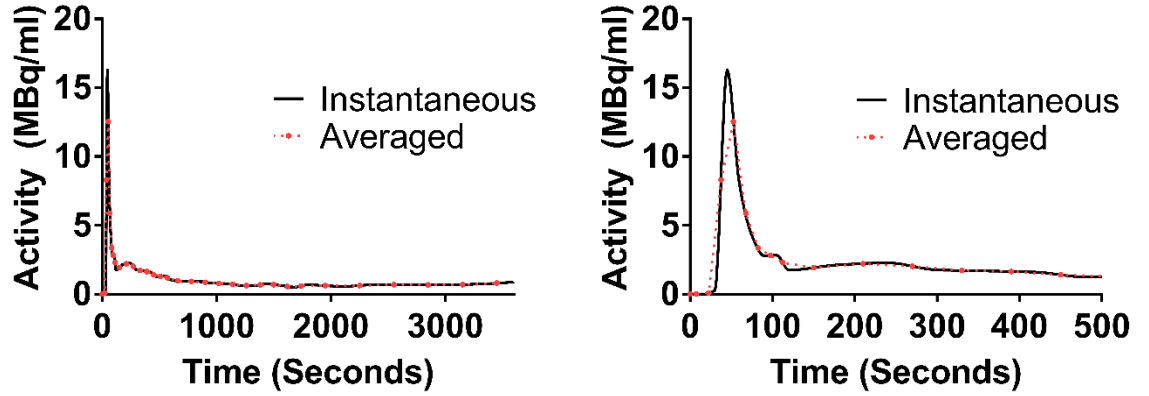


Figure 3.3: Instantaneous and simulated averaged arterial TACs. The full acquisition duration (3,600 s) is shown on the left, and an expanded time scale (0-500s) is shown on the right. This frame averaging schedule was also applied to the tissue TAC.

3.2.7 Effect of Omitting Blood Volume Term

To determine the effect of omitting the blood volume term in Equation (4) on the estimate of the k_3 parameter, tissue TAC's were generated with the parameters found in Table 3.1 with 50 different blood volume values ranging from 0 to 0.1 ml/g. Each tissue TAC was fitted with the 3C-LIN solution (no V_b term) to obtain an estimate of k_3 .

3.2.8 Simulating Noise of Time Activity Curves

Noise was added to the tissue TACs based on the PET noise model described by Logan *et. al.* [24, 25]. The noisy TAC is given by:

$$Q_n(t_k) = ROI(t_k) + G(0,1) \cdot \varepsilon \cdot \sqrt{ROI(t_k) e^{\lambda t_k}} \quad (19)$$

where t_k is the midpoint time of the k^{th} acquisition frame, Q_n is the noisy activity concentration, $G(0,1)$ is a random number based on Gaussian distribution of zero mean and variance equal to one, ε is a scale factor that determines the magnitude of the noise, λ is the decay constant of the radioisotope which is equal to $\ln(2)$ divided by its half-life, and $ROI(t_k)$ is the time-weighted average concentration for the k^{th} acquisition frame, as defined in Equation (18). The noise level was defined as

$$\langle f_N^Q \rangle_{N,t} = \text{avg} \left\{ \frac{\text{abs}(Q_n(t) - Q(t))}{Q(t)} \right\} \quad (20)$$

where $Q(t)$ is the original data and $Q_n(t)$ is the noisy data, generated with the 3-compartment model using parameters in Table 3.1. The average over all data points and all curves is taken. Noise levels investigated were $\langle f_N^Q \rangle_{N,t} = 0.05, 0.1, 0.25$ and 0.5 , which represent SNRs of roughly 20, 10, 4, and 2, respectively.

3.2.9 Linearity of k_3 Estimates

The linearity of the k_3 estimates over a wide range of k_3 values was investigated. A range of tissue TACs were generated using 20 different k_3 values at equal intervals between 0.01 and 0.5 min^{-1} . The other model parameter values were the ones described above. (Table 3.1) Each tissue TAC was fitted with every linearized or non-linear model solution and the estimated k_3 was plotted vs. the true k_3 . For the noisy TACs, 250 noise runs were

performed for each value of k_3 and the means and standard deviations of the k_3 estimates were calculated for each.

3.2.10 Effect of Bias in a priori K_1 and k_2

The presence of CT image noise in the TDC introduces uncertainty into the K_1 and k_2 parameters measured with CT Perfusion, in the form of bias and/or variation. Therefore, it is important to understand the effect of this uncertainty on the k_3 parameter estimate in the 3-compartment model of Figure 3.1. To obtain a realistic estimate of bias on K_1 and k_2 , an arterial time density curve (TDC) was measured with a CT Perfusion study of a mouse heart. The curve was measured using an ROI drawn in the left ventricle of the mouse heart. A simulated tissue TDC was generated using a 2-compartment model with parameters K_1 and k_2 equal to 0.12 ml/min/g and 0.57 min⁻¹, respectively, which was the same as in the simulations of the 3-compartment model.

A cylindrical phantom with diameter of 35 mm and length of 100 mm (to approximate the size of a mouse) was filled with water and scanned with the same CT Perfusion protocol as in our mouse studies (FOV 10cm, 80kVp, 200mA, 0.5s per rotation of the gantry and 1.25mm slice thickness.) The phantom was scanned 70 times. A 451-voxel ROI was drawn in the phantom images. The variance of the 70 measurements was calculated for each voxel, and then the mean of the variances of all 451 voxels was calculated.

The central limit theorem indicates that many additive sources of noise together, as found in DCE-CT, will produce noise with a Gaussian distribution. [26] A Gaussian noise model was used to add noise to the generated tissue TDC with variance equal to the mean

variance measured with the phantom (19.4 HU). 250 noisy TDC's were generated and each was fitted using the 2-compartment model with the non-linear trust regional reflective algorithm in Matlab. The estimates of K_1 and k_2 from each of the noisy TDC were then carried over and used as the *a priori* parameter estimates in the 3-compartment model simulation.

3.2.11 Parameter Accuracy and Best Fit

The simulated frame-averaged PET TACs with simulated noise were fitted with each of the linear and non-linear model solutions and the k_3 estimates for each model solution were compared to the true value to calculate the bias. 250 noisy curves were generated and the mean and standard deviation of the estimates were calculated to determine the coefficient of variation of the estimates, equal to the standard deviation divided by the mean. This was repeated for the case of simulated bias added to the K_1 and k_2 parameters based on the CT phantom measurement described above.

The Akaike information criterion for small sample sizes (AICc) was used to compare the different model solutions [27]. The AICc determines the best model for the fit by taking into account the SSD's of the fit and the model complexity in terms of the number of parameters. The AICc can only be compared for different model fits of the same observation. The model fit that produces the lowest AICc is considered to be the best fit. The Akaike weights were calculated in order to determine the probability that a given model was the best model available to fit the data. For example, a model with an Akaike weight of 0.5 has a 50% chance of being the best model for the given data. By definition,

the sum of Akaike weights from all solutions is 1. The Akaike weights were determined for the noiseless case.

3.3 Results

3.3.1 Sensitivity

The normalized sensitivity functions for the 3-Compartment model are shown in Figure 3.4. The sensitivity functions obtained using the numerical method proved to be identical to those obtained with the analytical method. The most sensitive parameters after 30 minutes are K_1 and k_2 , followed by k_3 . The sensitivity curve for k_3 indicated that this parameter becomes increasingly sensitive for approximately the first 15 minutes of the scan, while there is only a modest improvement in sensitivity beyond this time.

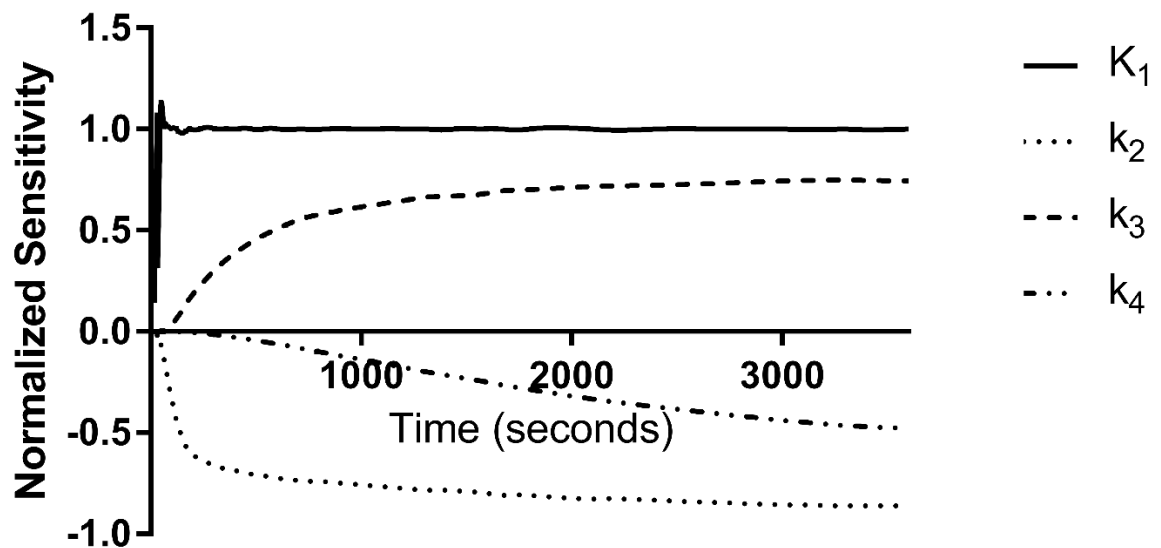


Figure 3.4: Normalized sensitivity curve calculated for each parameter of the 3-Compartment model as a function of time.

Identifiability analysis for the simulated case yielded the correlation matrix (Table 3.4) which indicated that parameters K_1 and k_2 as well as k_2 and k_3 were highly correlated.

Table 3.4: Correlation matrix for the 3-Compartment model. Highly correlated parameters are in bold. Values in the upper right triangular region are omitted given that it is a symmetric matrix.

	K_1	k_2	k_3	k_4
K_1	1	-	-	-
k_2	0.89	1	-	-
k_3	0.61	0.88	1	-
k_4	0.04	0.26	0.60	1

3.3.2 CT Noise Simulation

The 2 compartment CT noise simulation resulted in mean (\pm SD) estimates for K_1 of 0.116 ± 0.009 ml/min/g and k_2 of 0.54 ± 0.1 min⁻¹ or a bias and COV for K_1 of -3.3% and 7.5%, respectively, and -5.4% and 18.6%, respectively for k_2 .

3.3.3 k_3 Linearity

For the noise-free TAC case plus no error in K_1 and k_2 , estimated k_3 vs. true k_3 for all model solutions was linear with a slope of 1 and the estimates had negligible bias.

Results for noise $\langle f_N^Q \rangle_{N,t} = 0.25$ (SNR = 4) are shown in Figure 3.5. The 3C-LIN and 3C-LIN-K1 solutions were more biased as k_3 increased compared to their non-linear counterparts. The 3C-LIN-K1k2 solution was the only linear solution that showed a consistent linear trend over the range of k_3 values investigated.

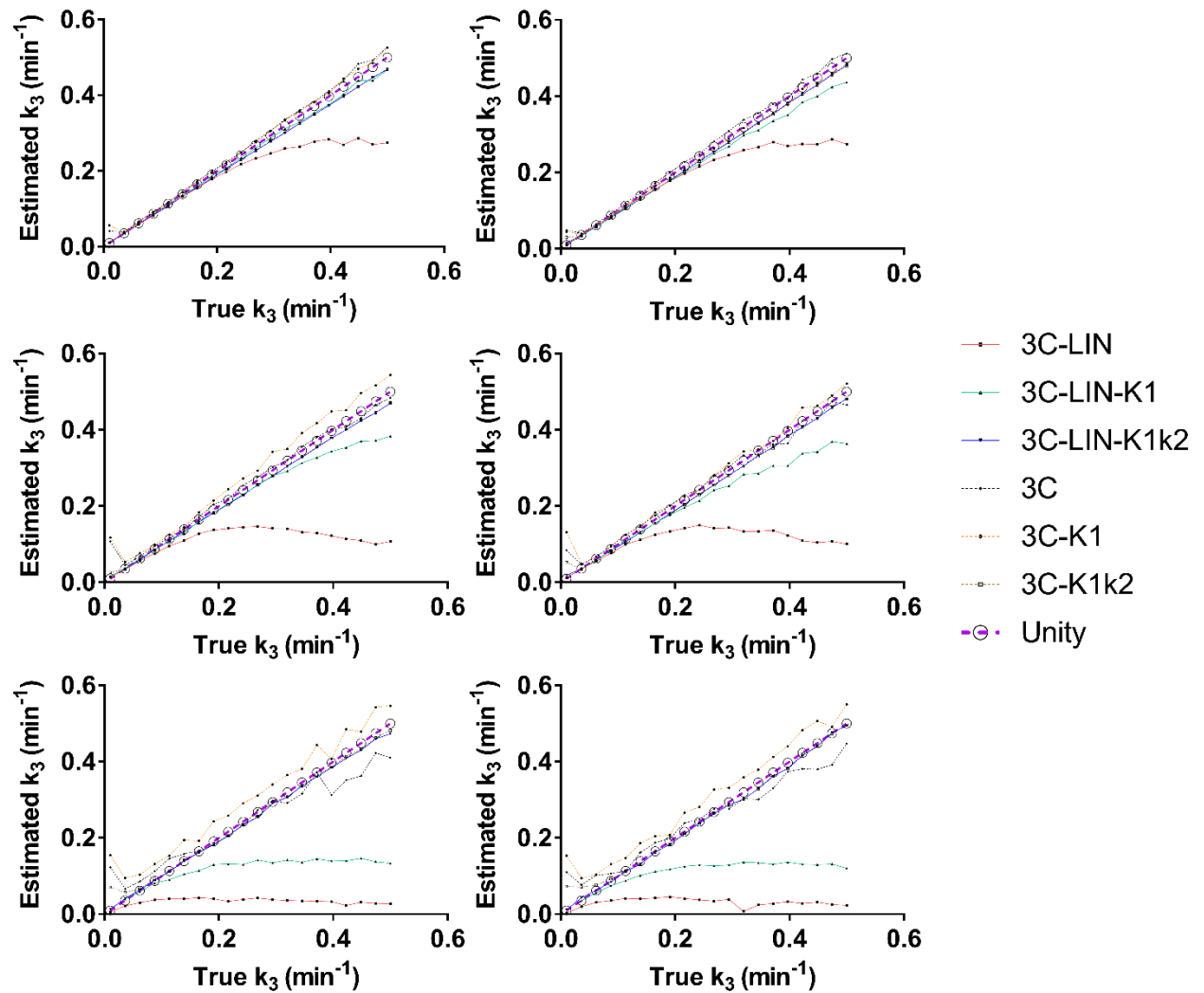


Figure 3.5: Estimated vs. true k_3 for all the model solutions. (Left) No error in K_1 and k_2 . (Right) K_1 and k_2 with simulated bias. (Top) SNR = 20, (Middle) SNR = 10, (Bottom) SNR = 4. Solid and dashed lines represent the linear and non-linear solutions, respectively.

3.3.4 Model Selection

The parameters estimated using the time-averaged TACs in the noise-free case are shown in Table 3.5 along with the AICc and Akaike weights w_i . The sum of squared deviations was very similar for all the model solutions, therefore the Akaike weights indicated that the 3C-LIN-K1k2 and 3C-K1k2 solutions were likely the best solutions because these solutions used the smallest number of parameters.

Table 3.5: Parameter estimates as well as Akaike information criterion for small samples sizes (AICc) and Akaike weights for the different models in the noiseless case. These data show the effect of frame averaging on the model fitting. The 3C-K1k2 and 3C-LIN-K1k2 solutions had the highest probability of producing the best fit because their SSD's were similar to other model solutions and they use the least number of parameters. (SSD = sum of squared deviations between the fit and the tissue TAC)

Model	K_1 (ml/min ⁻¹ /g)	k_2 (min ⁻¹)	k_3 (min ⁻¹)	k_4 (min ⁻¹)	SSD	AICc	w_i
Truth	0.12	0.56	0.23	0.03			
3C-LIN	0.120	0.568	0.228	0.027	12.7	-19.3	0.03
3C-LIN-K1		0.570	0.229	0.027	13.0	-21.3	0.08
3C-LIN-K1K2			0.228	0.027	13.1	-23.7	0.27
3C	0.118	0.556	0.227	0.027	11.4	-22.8	0.17
3C-K1		0.577	0.232	0.027	12.5	-22.5	0.15
3C-K1K2			0.228	0.027	13.0	-23.9	0.30

3.3.5 Effect of Omitting Blood Volume Term

The k_3 estimates produced by the 3C-LIN solution (with no V_b term) with different true values of V_b are shown in Figure 3.6. The bias in k_3 increased as the true V_b increased.

For $V_b < 0.02$ ml/g, the bias in the k_3 estimate was $< 4\%$. At $V_b = 0.05$ ml/g, the bias was 14%. For $V_b = 0.1$ ml/g, the bias was 29%.

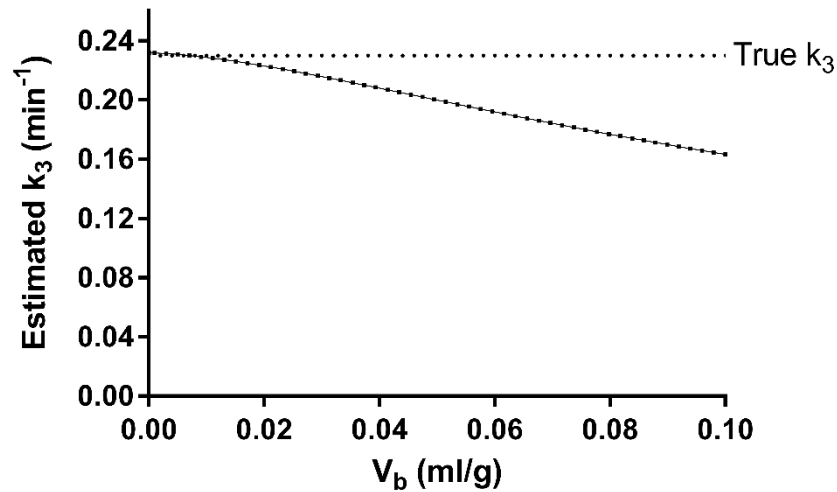


Figure 3.6: k_3 estimates produced by the 3C-LIN model solution (with no V_b term) for different values of V_b .

3.3.6 k_3 Accuracy and Variability

The coefficients of variation for the different parameter estimates calculated with the covariance matrix are shown in Figure 3.7. The COV of the k_3 parameter improved when K_1 was imputed from CT Perfusion and improved further when both K_1 and k_2 were imputed from CT Perfusion.

The mean k_3 estimates (\pm SD) and coefficient of variation (COV) for the 250 noise runs are shown in Figure 3.8 for the bias-free K_1 and k_2 as well as with addition of simulated bias. The non-linear 3C solution had the most accurate mean k_3 estimate, while the 3C-K1k2 and 3C-LIN-K1k2 solutions had the smallest variation under all noise levels. This

simulation was also performed with PMod software (PMod Technologies) for the 3C model and similar results were produced. These results also apply to the linear solutions, given that the linear solutions are based on the same model as the non-linear solutions. The COV for k_3 with the 3C-K1k2 solution was similar to the one obtained with noise simulations of the 3C-K1k2 and 3C-LIN-K1k2 solutions in Figure 3.8 (top row, noise level = 0.25).

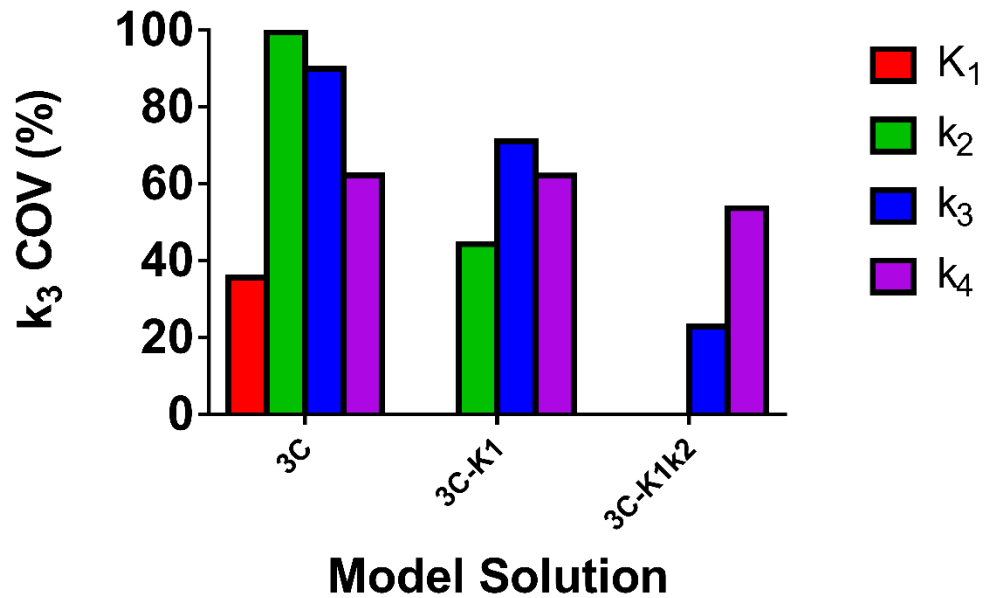


Figure 3.7: The coefficients of variation of model parameters with TAC SNR = 4 calculated using the covariance matrix represent the Cramér-Rao Bound. The COV of k_3 improves as more parameters are measured a priori.

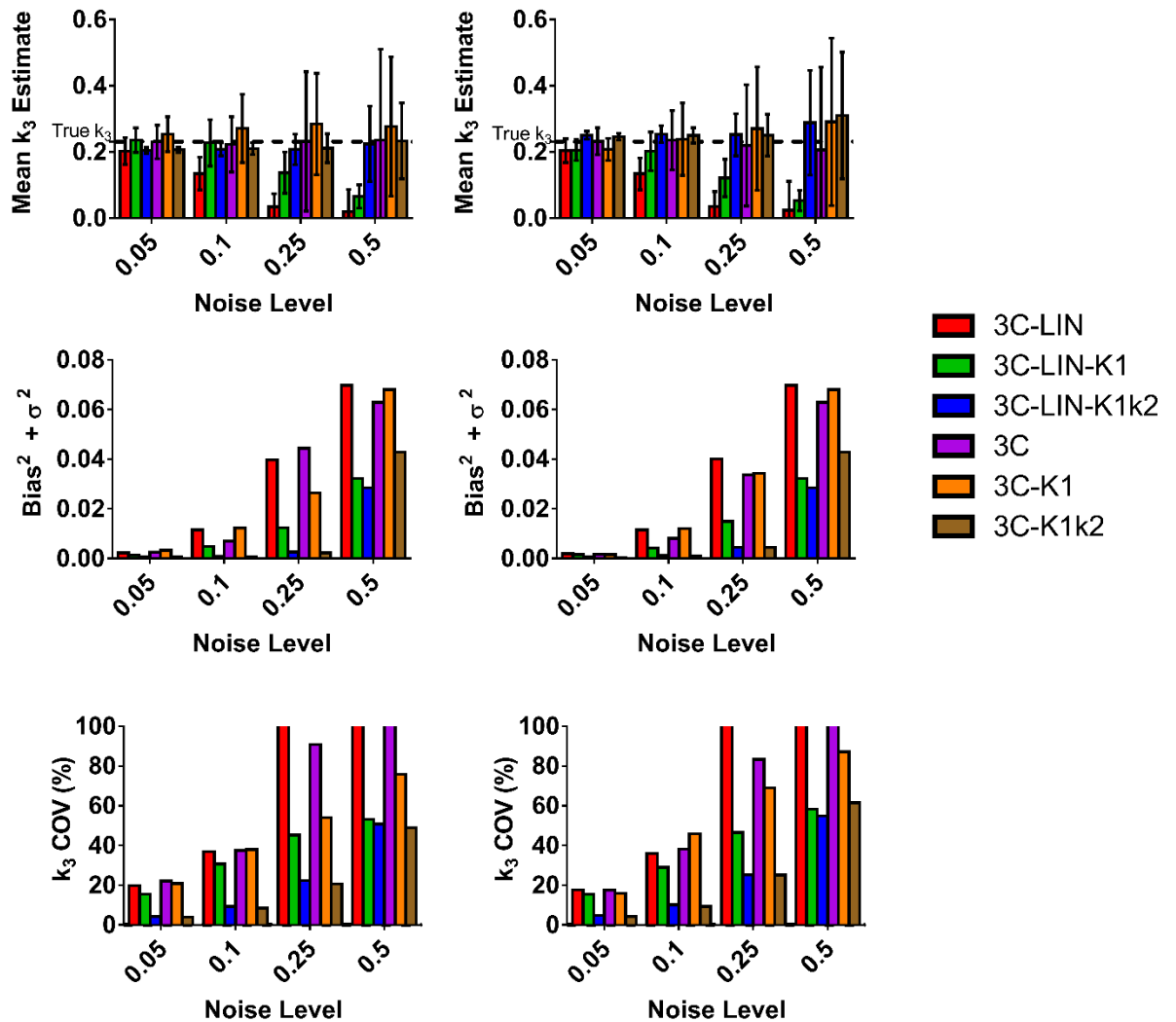


Figure 3.8: k_3 estimates (top row), bias² + variance (middle row), and COV (bottom row) for 250 noise runs with no K_1 and k_2 error (left column), and simulated error

(right column). Error bars represent standard deviation. The horizontal dashed line indicates the true value of k_3 . (0.23 min^{-1})

3.4 Discussion

This study simulated the use of a hybrid DCE-CT/PET imaging technique that uses functional parameters estimated from CT Perfusion as a priori information to increase the precision of the estimated binding rate constant, k_3 in a 3-compartment model. Linearized and non-linear solutions of the 3-compartment model were compared in terms of bias and variation of the k_3 estimate.

Compared to the non-linear solutions, k_3 estimates from the linearized solutions suffered more bias. The reason being the linearized solution depends not only on the tissue TAC, $Q(t)$, but also the time integrated and doubly time integrated $Q(t)$ as shown in Equation (9). As such, noise in $Q(t)$ is accumulated in its time integrals as time progresses through integration. It also means that whereas noise in $Q(t)$ is independent, the same is not true for noise in its time integrals. The correlation of noise in the time integrals of $Q(t)$ is the main reason why biases occur in parameters estimated from the linearized solution. This finding is consistent with the results of Feng et. al. [12] who developed a generalized least squares technique to fit the linearized solution of compartmental models to $Q(t)$ that minimize biases in the estimated model parameters. Feng et. al. showed mathematically that the increased bias present in the linearized model solution is because the noise in the TAC is coloured (i.e. correlated) by the estimates of parameters P_1 and P_2 , and hence of k_2 , k_3 and k_4 . Because of this correlation, poor precision in these parameter estimates will result in increased bias in the parameter estimates. It therefore follows that increasing the

precision of the parameter estimates by measuring parameters a priori will also reduce the magnitude of the bias in the linearized model. Our results confirm that the bias effect is mitigated by the introduction of known parameters as shown in Figure 3.5 where the 3C-LIN-K1k2 solution maintained a linear trend over the range of k_3 values investigated. This is because the inclusion of K_1 and k_2 parameters measured a priori was sufficient to increase the precision of parameter estimates such that the bias due to correlated noise became insignificant.

The AICc indicated that the best model solutions to fit the time-averaged data were the 3C-K1k2 and 3C-LIN-K1k2 solutions. This was expected given the reduction of parameter covariance resulting from the use of a priori measured parameters. The Akaike weights indicated a 30% probability that the 3C-K1k2 model solution produced the best fit compared to 27% for the 3C-LIN-K1k2 solution in the noiseless case. Practically, this difference will be insignificant under noisy conditions that are typical of PET images.

The simulation results presented here illustrate the reason why it has been difficult to independently estimate model parameters with 3-compartment (two tissue) models. The identifiability analysis shows that the K_1 and k_2 parameters are highly correlated with each other (0.89), and that k_2 has a high correlation with k_3 (0.88). The effect of this correlation is evident in the extremely high COV of the estimated k_3 parameter under noisy conditions (Figure 3.8). However, the COV can be very much improved with the hybrid DCE-CT/PET technique wherein K_1 and k_2 will be estimated from DCE-CT as in the 3C-LIN-K1k2 and 3C-K1k2 solutions.

Besides the injected dose (activity), the SNR observed in PET depends on a variety of factors, including the bore size, attenuation and randoms corrections, the temporal protocol and the size of the ROI. Under low SNR conditions, it would be possible to improve the SNR by spatially averaging pixels in a region or by temporal averaging by using a temporal protocol with longer acquisition time per image. The COV results can serve as a guide when using the hybrid DCE-CT/PET technique to give a sense of the precision of the k_3 parameter estimate under noisy conditions. Our simulations found that the COV of the k_3 parameter produced by the covariance matrix for $\text{SNR} = 4$ were of the same order of magnitude as those from noise simulations. This demonstrates that the covariance matrix can be used instead of time-consuming noise simulations in order to estimate the reliability of compartmental model parameter estimates.

Other investigators in the literature have omitted the blood volume term of the 3-compartment model [7]. Our simulations show that the blood volume term can be omitted without any significant bias in the k_3 estimate if $V_b < 0.02$ ml/g. To keep k_3 bias resulting from omission of the V_b term to no more than 10%, the no- V_b model solution should be limited to applications where $V_b \leq 0.04$ ml/g is expected. For tissues where V_b is larger, a realistic way to account for the effect of blood volume would be to include a vascular operator that incorporates the effect of transit time between arterial and venous ends of the capillaries. This vascular operator is employed in the Johnson-Wilson model [28, 29] and is evident when comparing the impulse-residue functions (which represent the fraction of tracer remaining in tissue as a function of time) of the Johnson-Wilson vs. compartmental models (Figure 3.9). The vascular operator would need to be added to the compartmental

model to account for the V_b term. However, this would require a reformulation of the linearized solution to account for the effects of capillary transit time and may increase the required computation time.

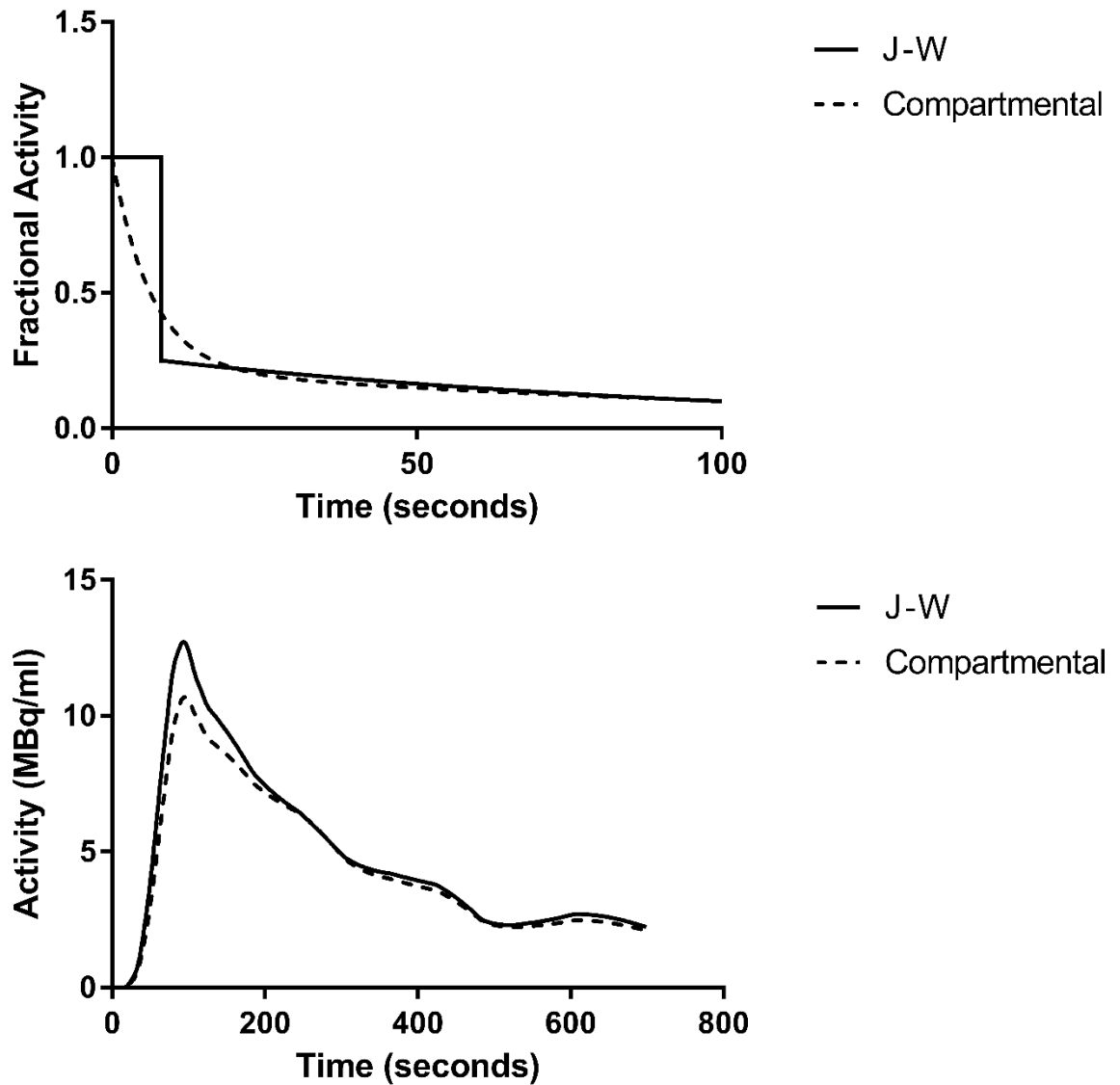


Figure 3.9: (Top) Example of impulse residue functions (IRF) of the Johnson-Wilson (J-W) and 3-compartment models. The vascular operator accounting for the

transit time in the capillaries is represented by the flat, step portion of the J-W model's IRF. This vascular operator is absent in the 3-compartment IRF, which assumes instantaneous transfer and therefore cannot properly account for the effects of blood volume in the vasculature. The blood volume is equal to the area under the step portion of the J-W model's IRF. (Bottom) Example of tissue TACs produced by convolution of the arterial input TAC with the flow-scaled IRF using the same parameters, highlighting the differences resulting from the omission of the vascular operator.

The linearized solution of the 3-compartment model should permit rapid generation of parameter functional maps. For example, the linearized solution performed roughly 20 times faster than the non-linear solution. A 128x128 k_3 parameter map could be generated in less than 30 minutes.

There are some limitations to this study. The CT noise was simulated from measurements taken with a phantom which may not accurately represent the noise present in all cases given that CT noise depends on a variety of factors, such as tube current and patient size. Secondly, the simulation studies were generated with a compartment model which does not account for sources of uncertainty introduced by the potential inapplicability of the compartmental model to certain specific pathologies or tissue types, or uncertainties inherent in the corrections applied to the real world arterial TAC's such as dispersion or metabolite corrections. Finally, differences in molecular weight between the CT contrast and PET tracer would need to be accounted for in the real world case since these would have different rates of diffusion into the extravascular space. This should be

possible with the use of a scalar correction factor based on a cubic root relationship between the two molecular weights. [11] The correction factor could be used to correct the K_1 and k_2 parameters for the effect of diffusion before they are imputed into the PET model. In addition, the dependence of molecular weight on the interstitial and osmotic pressures may also need to be accounted for because these effects may be significant in certain tumor pathologies [30]. This area warrants further investigation.

This hybrid imaging technique has a wide range of potential applications for different pathologies and different tracers for which quantification of the binding rate constant k_3 for the 3-compartment (two tissue) model is of interest.

3.5 Conclusions

A hybrid DCE-CT/PET imaging technique has been developed that allows for more accurate and reliable quantification of the binding rate constant in compartment models. The linearized solution of this model can be used for much more rapid generation of functional maps compared to the standard non-linear approach. This technique may be useful for applications or pathologies where one wishes to quantify the binding rate constant of the 3-compartment (two tissue) model.

3.6 Acknowledgments

The authors wish to acknowledge the financial support of the CIHR Group Grant on Urological Imaging, the Ontario Institute of Cancer Research, and the Quantitative Imaging Network, CIHR and NIH. They also would like to acknowledge the assistance of John Valliant of the Centre for Probe Development and Commercialization.

3.7 References

1. Gambhir, S.S., *Molecular imaging of cancer with positron emission tomography*. Nat Rev Cancer, 2002. **2**(9): p. 683-693.
2. Ichise, M., J.H. Meyer, and Y. Yonekura, *An introduction to PET and SPECT neuroreceptor quantification models*. J Nucl Med, 2001. **42**(5): p. 755-63.
3. Huang, S.C., *Anatomy of SUV. Standardized uptake value*. Nucl Med Biol, 2000. **27**(7): p. 643-6.
4. Freedman, N.M., et al., *Comparison of SUV and Patlak slope for monitoring of cancer therapy using serial PET scans*. Eur J Nucl Med Mol Imaging, 2003. **30**(1): p. 46-53.
5. Boellaard, R., et al., *Effects of noise, image resolution, and ROI definition on the accuracy of standard uptake values: a simulation study*. J Nucl Med, 2004. **45**(9): p. 1519-27.
6. Watabe, H., et al., *PET kinetic analysis--compartmental model*. Ann Nucl Med, 2006. **20**(9): p. 583-8.
7. Slaets, D. and F. De Vos, *Comparison between kinetic modelling and graphical analysis for the quantification of [18F]fluoromethylcholine uptake in mice*. EJNMMI Res, 2013. **3**(1): p. 66.
8. Muzi, M., et al., *Kinetic analysis of 3'-deoxy-3'-18F-fluorothymidine in patients with gliomas*. J Nucl Med, 2006. **47**(10): p. 1612-21.
9. Patlak, C.S., R.G. Blasberg, and J.D. Fenstermacher, *Graphical evaluation of blood-to-brain transfer constants from multiple-time uptake data*. J Cereb Blood Flow Metab, 1983. **3**(1): p. 1-7.
10. Logan, J., *Graphical analysis of PET data applied to reversible and irreversible tracers*. Nucl Med Biol, 2000. **27**(7): p. 661-70.
11. Nystrom, R., *Membrane Physiology*. 1976: Prentice-Hall.
12. Feng, D., et al., *An unbiased parametric imaging algorithm for nonuniformly sampled biomedical system parameter estimation*. IEEE Trans Med Imaging, 1996. **15**(4): p. 512-8.

13. Blomqvist, G., *On the construction of functional maps in positron emission tomography*. J Cereb Blood Flow Metab, 1984. **4**(4): p. 629-32.
14. Butterworth, E., et al., *JSim, an open-source modeling system for data analysis*. F1000Research, 2013. **2**: p. 288.
15. Coleman, T.F. and Y. Li, *An Interior Trust Region Approach for Nonlinear Minimization Subject to Bounds*. SIAM Journal on Optimization, 1996. **6**(2): p. 418-445.
16. *MATLAB and Statistics Toolbox Release 2014a*. The MathWorks, Inc.: Natick, Massachusetts, United States.
17. Lawson and Hanson, in *Solving Least Squares Problems*. 1974, Prentice-Hall. p. 161.
18. DeGrado, T.R., et al., *Pharmacokinetics and Radiation Dosimetry of ^{18}F -Fluorocholine*. Journal of Nuclear Medicine, 2002. **43**(1): p. 92-96.
19. Verwer, E.E., et al., *Quantification of ^{18}F -fluorocholine kinetics in patients with prostate cancer*. J Nucl Med, 2015. **56**(3): p. 365-71.
20. Draper, N.R. and H. Smith, *Applied Regression Analysis*. 1966, New York: John Wiley & Sons, Inc.
21. Cramér, H., *Mathematical Methods of Statistics*. 1946, Princeton, NJ: Princeton Univ. Press.
22. Rao, C.R., *Information and the Accuracy Attainable in the Estimation of Statistical Parameters*, in *Breakthroughs in Statistics: Foundations and Basic Theory*, S. Kotz and N.L. Johnson, Editors. 1992, Springer New York: New York, NY. p. 235-247.
23. Chen, K.W., S.C. Huang, and D.C. Yu, *The effects of measurement errors in the plasma radioactivity curve on parameter estimation in positron emission tomography*. Phys Med Biol, 1991. **36**(9): p. 1183-200.
24. Logan, J., et al., *A strategy for removing the bias in the graphical analysis method*. J Cereb Blood Flow Metab, 2001. **21**(3): p. 307-20.
25. Varga, J. and Z. Szabo, *Modified regression model for the Logan plot*. J Cereb Blood Flow Metab, 2002. **22**(2): p. 240-4.

26. Lu, H., et al. *Analytical noise treatment for low-dose CT projection data by penalized weighted least-square smoothing in the K-L domain*. 2002.
27. Glatting, G., et al., *Choosing the optimal fit function: Comparison of the Akaike information criterion and the F-test*. Medical Physics, 2007. **34**(11): p. 4285-4292.
28. Johnson, J.A. and T.A. Wilson, *A model for capillary exchange*. Am J Physiol, 1966. **210**(6): p. 1299-303.
29. Sawada, Y., C.S. Patlak, and R.G. Blasberg, *Kinetic analysis of cerebrovascular transport based on indicator diffusion technique*. Am J Physiol, 1989. **256**(3 Pt 2): p. H794-812.
30. Baxter, L.T. and R.K. Jain, *Transport of fluid and macromolecules in tumors. I. Role of interstitial pressure and convection*. Microvasc Res, 1989. **37**(1): p. 77-104.

Chapter 4

4 A quantitative hybrid PET-CT Perfusion technique for measuring the binding rate constant of ^{18}F -Fluorocholine in a mouse model of prostate cancer

4.1 Introduction

^{18}F -Fluorocholine (FCH) PET imaging has been used for imaging prostate cancer (PCa) [1, 2]. Choline is of interest because it is phosphorylated by the enzyme choline kinase into phosphocholine via the ATP-dependent Kennedy pathway before being incorporated into the cell membrane as phosphatidylcholine [3, 4]. Malignant PCa overexpresses choline kinase [5, 6] and has been shown to contain more phosphocholine compared to benign or healthy prostate tissues [7], making the phosphorylation of choline a potentially useful biomarker for localizing PCa with ^{18}F -FCH PET imaging.

Results of previous studies investigating the use of ^{18}F -FCH PET for detection of PCa have been mixed [8-13]. These studies quantify uptake of FCH using the standardized uptake value (SUV), a semi-quantitative analysis metric that scales the measured activity by the injected radiopharmaceutical activity and the patient's weight. The general finding has been that it is difficult to differentiate malignant PCa from surrounding prostate tissue, such as benign prostatic hyperplasia (BPH), when using the SUV. This suggests that the SUV is not reflective of the phosphocholine levels in tissue nor the choline kinase activity. One potential reason for this is that the SUV cannot differentiate between ^{18}F -FCH molecules which are specifically bound to cells (phosphorylated) and those that are present in the unbound state in the vasculature or in tissue water.

The aim of tracer kinetic analysis with compartmental models is to quantify the rates of exchange between different physiological compartments. Theoretically, this approach would be capable of quantifying the phosphorylation rate of choline or the activity of choline kinase by measuring the binding rate constant, k_3 . In practice, there are a number of challenges with this approach. Kinetic analysis of compartmental models entails nonlinear curve fitting with multiple parameters. The curve fitting algorithm must be provided with initial guesses or starting model parameters, and the algorithm may converge and terminate in one of many local minima. Nonlinear optimization is also computationally intensive, such that generation of parametric maps is a time-consuming process and inconvenient in clinical settings. Finally, obtaining a robust, accurate estimate of k_3 is difficult because of the high variability from the significant covariance between model parameters, which makes the model even more susceptible to PET image noise [14].

These challenges may be overcome with multiple approaches. First, it is possible to derive a linearized solution to the 3-compartment model, which has been previously described by other investigators [15-17]. The linearized solution enables fast computation of functional maps, does not require any starting parameters, and converges to a single solution. Secondly, it is possible to use a hybrid PET-CT Perfusion (PET-CTP) imaging technique in which two (K_1 , k_2) of the four model parameters are imputed from a separate CT Perfusion study so that only the remaining two model parameters (k_3 , k_4) need to be estimated from the PET data [17]. This results in reduced parameter covariance and more robust estimates of the k_3 parameter.

The objectives of this work are to determine whether quantitative graphical analysis of PET or hybrid PET-CTP imaging can provide better tumor contrast compared to the SUV in a mouse model of human prostate cancer. It has previously been found that choline uptake as measured by SUV is not correlated with tumor proliferation [18] and hence volume. We investigated whether PCa tumor volume in mice was significantly correlated with SUV as well as other quantitative parameters measured by PET-CTP imaging. Finally, preliminary immunohistochemistry was performed with a choline kinase α (ChK α) antibody to determine whether there was any correlation between the k_3 parameter and choline kinase expression.

4.2 Methods

4.2.1 Mouse Model

Twenty athymic nude mice were subcutaneously injected with 10^6 PC-3 human PCa cells in the left flank. Mice were observed weekly and the presence of a tumor was ascertained via palpation. The tumor was imaged bi-weekly at one or several time points post-injection, depending on the growth rate of the tumor. Mice were euthanized once tumors significantly affected the quality of life of the mice, as judged by veterinary staff. All experimental procedures were approved by the Animal Use Subcommittee of the Canadian Council on Animal Care of our institution.

4.2.2 PET Imaging Protocol

For imaging, each mouse was masked with 1.5-2% isoflurane. A dose of ^{18}F - FCH (11.4-15.4 MBq in < 0.4 mL, specific activity 543-963 Ci/ μmol , radiochemical purity $>$

99%, supplied by Centre for Probe Development and Commercialization, McMaster University, Hamilton, Ontario) was injected into a tail vein. Dynamic PET scanning, started 10 s before the injection was performed with a GE healthcare eXplore VISTA dual-ring small-animal PET scanner in list mode. After correction for scatter and random coincidences, images were reconstructed using the ordered subset expectation maximization algorithm and binned into frames of 8 x 15 s, 9 x 60 s, 10 x 120 s, and 6 x 300 s for a total scan time of one hour. Image-derived time-activity curve (TAC) from a region of interest (ROI) placed in the left ventricle was corrected for partial volume and spillover effects (see below) and used as the arterial TAC for subsequent kinetic analysis.

At the conclusion of each PET scanning session, the bed together with the mouse was removed and transported to the CT scanner, taking care not to move the mouse and keep it anesthetized with 1.5-2% isoflurane during the transfer. These precautions ensured minimal movement of the mouse between dynamic ^{18}F -FCH PET and CT Perfusion (CTP) scans.

4.2.3 CT Perfusion Scanning Protocol

CT Perfusion (CTP) studies were performed on a clinical PET-CT scanner (GE Healthcare, Waukesha, WI). Each mouse was masked with 1.5-2% isoflurane as in the dynamic ^{18}F -FCH PET scan. The CTP study began with an infusion of 0.25 ml of iodinated contrast agent (Conray 43, Mallinckrodt Pharmaceuticals, Dublin, Ireland) diluted to 50% with saline into the same tail vein as in the PET study at a rate of 3 ml/min. The CTP acquisition was performed with settings of FOV 10cm, 80kVp, 200mA, 0.5s per rotation of the gantry, and 16 slices each of 1.25 mm thickness in two phases. In the first phase, 60

scans were acquired at 0.5 second intervals, and in the second phase 10 scans were acquired at intervals of 15 seconds, for a total scan time of 210 seconds. Functional maps of blood flow (BF), blood volume (BV), vessel permeability surface product (PS), and extravascular volume (V_e) were generated for each study using CT Perfusion software (GE Healthcare, Waukesha, WI) [19]. The arterial time density curve was acquired with a ROI in the left ventricle of the mouse heart.

4.2.4 Partial Volume & Spillover Correction of Image-Derived PET TACs

^{18}F -FCH exhibits notable uptake in the myocardium of the mouse heart due to the presence of muscarinic acetylcholine receptors [20]. A portion of the myocardial activity can spill over into the left ventricle due to positron travel (mean ^{18}F positron range = 0.64 mm, max = 2.4 mm [21]) before the annihilation event, and radial movement of the myocardium resulting from cardiac motion can also contribute myocardium activity to the left ventricle region. This contributes to an overestimation of the image-derived arterial TAC (ID-ATAC) from the left ventricle. In addition, the diameter of the ventricle is of the same magnitude (see below) as the spatial resolution of the micro-PET scanner (~ 1.5 mm), so the ID-ATAC will also be subject to underestimation of the true activity, due to partial volume averaging. These partial volume and spillover effects can affect the accuracy of quantitative measurements derived with the ID-ATAC.

A mouse heart phantom was designed to correct for partial volume and spillover effects (Figure 4.1). To ensure accurate dimensions, a mouse heart was removed at the conclusion of a PC-3 imaging study, and the myocardium thickness and left ventricle

diameters were measured with a set of calipers. The left ventricle diameter was found to be 3 mm and the myocardium thickness was 1 mm. The phantom consisted of an inner cylindrical left ventricle (LV) chamber of 3 mm external diameter to approximate the left ventricle with chamber wall thickness of 0.8 mm. Surrounding this chamber was a myocardium wall in the shape of a cylindrical shell of internal thickness 1 mm and outer wall thickness of 0.8 mm. This chamber was surrounded by a larger cylindrical shell of external thickness 10 mm to represent the thorax of the mouse. An extra chamber with external diameter of 10 mm (much larger than the PET scanner resolution) and wall thickness of 0.8 mm was added as a control chamber just outside of the phantom. The phantom was made of Acrylonitrile butadiene styrene (ABS) plastic and constructed with a LulzBot TAZ 5 3D printer (Aleph Objects, Inc., Loveland, Colorado, USA).

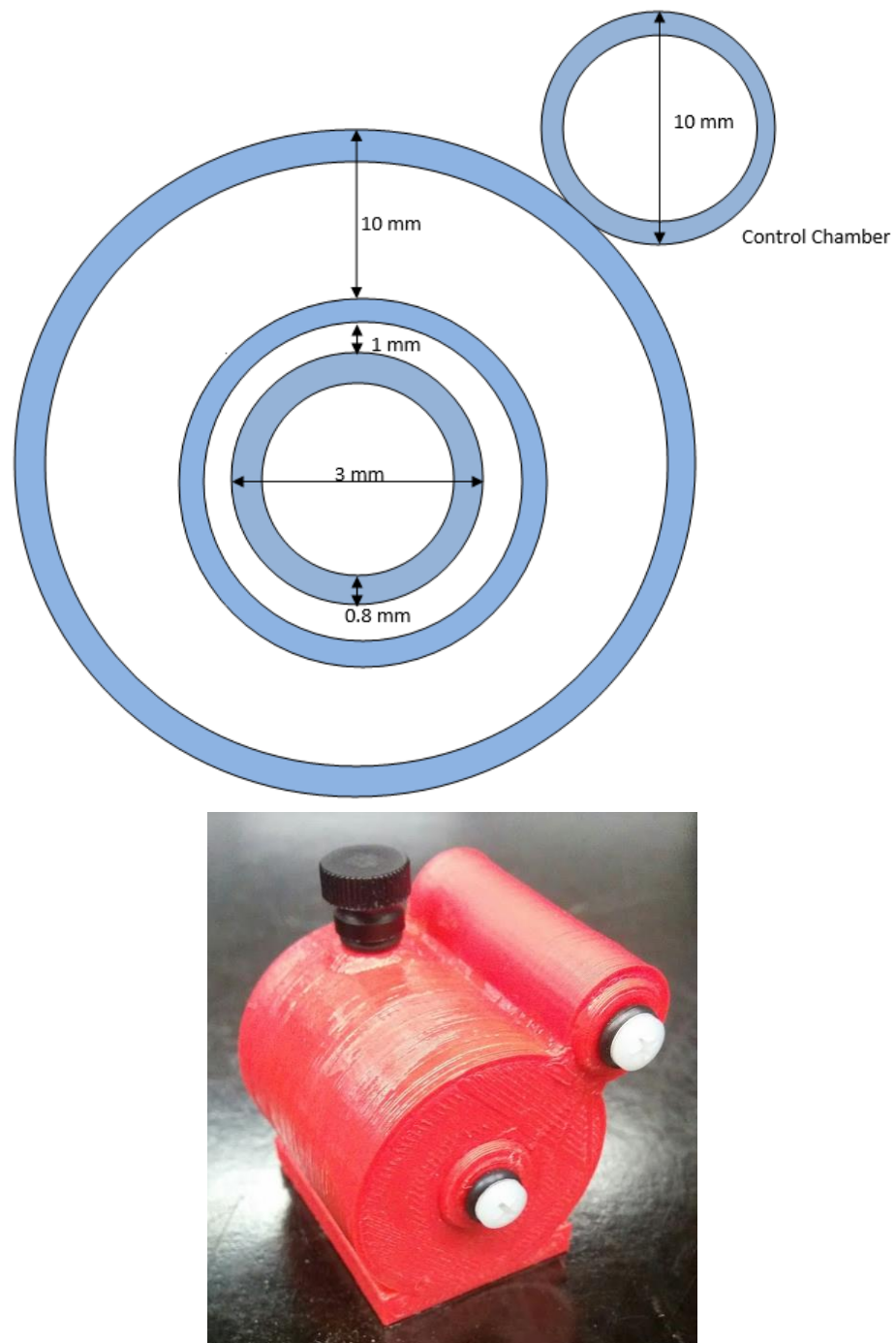


Figure 4.1: (Top) Cross-Section of the mouse heart phantom (not to scale, to emphasize the LV and myocardium chambers). The control chamber is located

outside the main phantom cylinder. All chamber walls are 0.8 mm thick. (Bottom) External view of the mouse heart phantom. The black thumb screw on top of the phantom provides access to the mouse thorax chamber. The center white screw accesses the LV chamber, and the other white screw accesses the control chamber. On the opposite side, another screw (not shown) provides access to the myocardium chamber.

The theory described by Shoghi et. al. [22] was used to characterize the relationship between the left ventricle and myocardium TACs and the partial volume and spillover coefficients:

$$\widetilde{C_{myo}}(t) = r_m C_{myo}(t) + s_{bm} C_{LV}(t) \quad (1)$$

$$\widetilde{C_{LV}}(t) = r_b C_{LV}(t) + s_{mb} C_{myo}(t) \quad (2)$$

Where $C_{LV}(t)$ and $C_{myo}(t)$ are the true left ventricle and myocardium curves, respectively, $\widetilde{C_{LV}}(t)$ and $\widetilde{C_{myo}}(t)$ are the left ventricle and myocardium curves measured by the PET scanner, r_b and r_m are the partial volume recovery coefficients for the left ventricle and myocardium, respectively, s_{bm} is the fraction of myocardium activity spilling into the left ventricle, and s_{mb} is the fraction of left ventricle activity spilling into the myocardium. By rearranging equations (1) and (2), one can solve for the true left ventricle TAC:

$$C_{LV}(t) = \frac{r_m}{r_m r_b - s_{bm} s_{mb}} \widetilde{C_{LV}}(t) - \frac{s_{mb}}{r_m r_b - s_{bm} s_{mb}} \widetilde{C_{myo}}(t) \quad (3)$$

This equation can be simplified by defining variables α and β that represent the coefficients of the two terms, such that:

$$C_{LV}(t) = \alpha \widetilde{C_{LV}}(t) - \beta \widetilde{C_{myo}}(t) \quad (4)$$

In order to utilize this equation, the partial volume and recovery coefficients must be calculated.

Two scans of the mouse heart phantom were obtained. In the first scan, the myocardial wall and the control chamber were filled with an ^{18}F -FDG solution, ensuring that the total activity in the phantom was < 18.5 MBq to not saturate the scanner. The LV and thorax chamber were filled with distilled water. The phantom was scanned using a static 30 minute scan to reduce the effect of noise. To ensure consistent segmentation of the LV chamber and myocardial wall in phantom images and real mouse heart images and to remove the element of operator variability, an in house automated algorithm was developed to segment these two regions of interest (ROIs) using the full width at half maximum of radial activity profiles drawn through the centre of the LV. The inner region encircled by the myocardium was used as the LV ROI. (Figure 4.2) The myocardium partial volume recovery coefficient r_m was calculated by dividing the mean myocardium ROI activity by the mean ROI activity of the control chamber. The myocardium to LV spillover s_{mb} was calculated by dividing the mean LV ROI activity by the mean control chamber ROI activity.

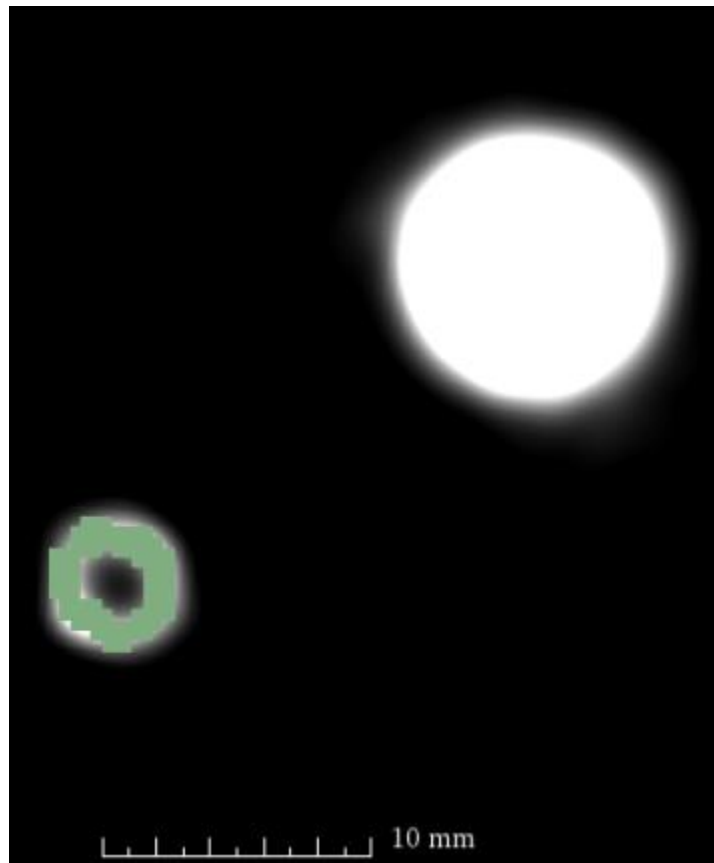


Figure 4.2: Axial slice of a mouse phantom PET scan with the myocardium chamber filled with FDG. The myocardium ROI produced by the automated segmentation algorithm is shown in green. The LV ROI was defined by the space surrounded by the myocardium ROI.

In the second scan, the LV and control chambers were filled with the same ^{18}F -FDG solution (again ensuring not to saturate the scanner) and the remaining chambers were filled with water. The first scan was manually registered to the second scan using a rigid registration by lining up the control and left ventricle chambers. (Figure 4.3) The ROI's generated in the first scan were then used for quantification in the second scan, to ensure

consistency. The LV partial volume recovery coefficient r_b was calculated by dividing the mean LV ROI activity by the mean ROI activity of the control chamber. The LV to myocardium spillover s_{bm} was calculated by dividing the mean myocardium ROI activity by the mean control chamber ROI activity.

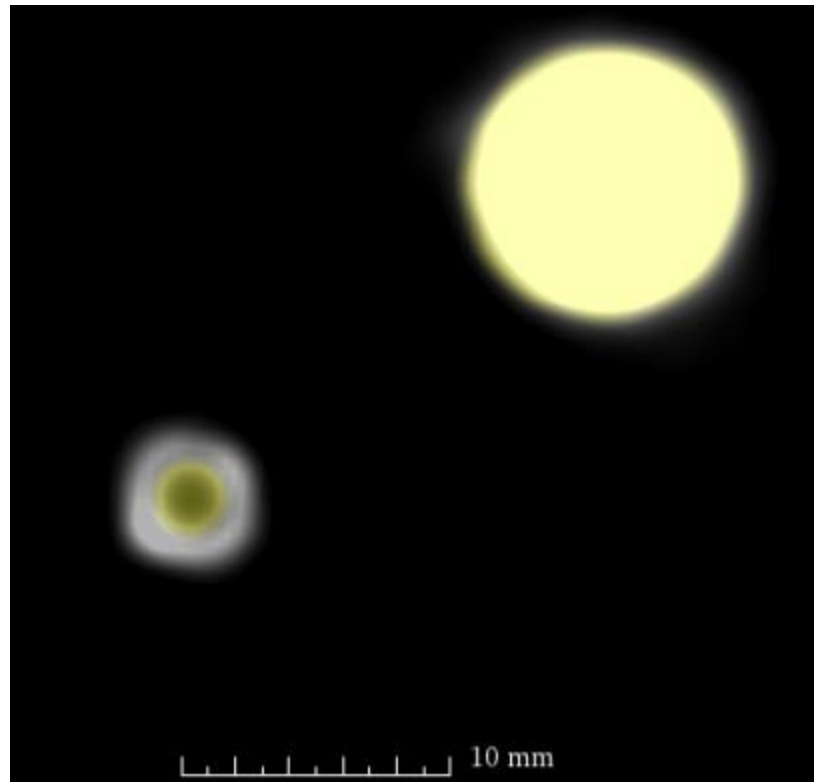


Figure 4.3: Registered images of the LV and myocardium phantom scans. The images were registered by aligning the control chambers from both scans. The activity from the LV scan is shown in yellow and the myocardium scan activity is shown in grey. The control chamber appears yellow because the images from both scans are superimposed.

4.2.5 Dispersion Correction

As blood travels between the arterial blood sampling catheter and then through the PE10 tubing to the arterial blood counter's detector, relative to the outlet of arterial catheter, the tracer bolus is delayed in arrival and is dispersed because the boundary layer at the PE10 tubing wall creates a radial velocity gradient that slows the speed of plasma depending on its proximity to the wall. This dispersion causes a broadening of the arterial time activity curve as measured by the arterial blood counter and will add uncertainty to the estimated model parameters if it is not corrected.

The arterial TAC at the outlet of the arterial catheter can be recovered by deconvolving the measured TAC with the blood counter's dispersion function according to the following equation:

$$\widetilde{C}_a(t) = C_a(t) * D(t) \quad (5)$$

where $\widetilde{C}_a(t)$ is the arterial TAC measured by the blood counter, $C_a(t)$ is the arterial TAC at the outlet of the arterial catheter, $D(t)$ is the dispersion function of the blood counter and * denotes the convolution operator [23].

The blood counter dispersion function was obtained by measuring the response of the blood counter to an abrupt increase of activity delivered at the PE10 tubing's inlet. Two solutions were prepared: 1) A 'cold' 40% sucrose solution in order to approximate the viscosity of blood [24] and 2) a similar 'hot' solution with ^{18}F -FCH added. The same 50.8 cm long PE10 tubing line used in our mouse experiments was also used in this dispersion experiment. First the line was filled with the 'cold' sucrose solution with care not to introduce any air bubbles. Next, one end of the line was connected to the blood counter

while the other end was submerged in the ‘hot’ sucrose solution and acquisition with the blood counter was started. The hot solution was withdrawn at a speed of 10 $\mu\text{l}/\text{min}$, the same as in our mouse studies, and the activity passing through the blood counter was measured for a time period until an obvious plateau was achieved. This same experiment was repeated for a pumping speed of 50 $\mu\text{l}/\text{min}$ because one mouse in the experiment had blood sampled at this rate. The measured TAC was corrected for radioactive decay of Fluorine-18 and normalized to a peak value of 1. The normalized TAC was fitted to an inverted exponential curve:

$$S(t) = \begin{cases} 0, & t < \tau \\ 1 - e^{-k(t-\tau)}, & t \geq \tau \end{cases} \quad (6)$$

where k is an exponential decay constant and τ is the delay in arrival of activity at the detector of the blood counter. The dispersion function $D(t)$ is the derivative of $S(t)$ and is evaluated as:

$$D(t) = \begin{cases} 0, & t < \tau \\ ke^{-k(t-\tau)}, & t \geq \tau \end{cases} \quad (7)$$

$D(t)$ can then be used for the deconvolution in Equation (5) to obtain the arterial TAC at the outlet of the arterial catheter [23].

A common technique to correct for dispersion by the PE 10 tubing used in the blood counter is the model-based correction proposed by Munk et. al. [25] employed in the

popular PMod software. This model-based deconvolution is not applicable to this work because it is invalid in cases where the fraction of tracer molecules λ (defined as α in Munk's paper) interacting with the catheter wall approaches 1. This is the case for our experiments, given the small inside diameter (0.28 mm) of PE10 tubing and the slow pumping speed that was required. Fitting the measured dispersion curve with Munk's method confirmed that λ approaches 1 in our experiments. Therefore, a model-independent deconvolution was used to deconvolve the measured TAC with the dispersion function. Unconstrained deconvolution presents a number of challenges [26] due to oscillatory noise that results from small singular values that arise in the singular value decomposition of the convolution matrix. The deconvolution technique used applies a constraint on the second derivative of the solution, ensuring that the deconvolved arterial TAC is smooth.

4.2.6 Validation of Partial Volume and Spillover Correction

To validate the accuracy of the partial volume and spillover correction, six acute studies were performed using athymic nude mice injected with ^{18}F -FCH. Blood was continuously sampled from the carotid artery at a withdrawal rate of 10 $\mu\text{l}/\text{min}$ (50 $\mu\text{l}/\text{min}$ for one of the mice) using heparinized PE10 tubing to prevent blood clotting and the sampled activity was measured using a blood counter (Swisstrace Twilite Blood Sampling System) at intervals of one second. The blood sampled TACs were corrected for radioactive decay of ^{18}F , background subtracted and corrected for dispersion in the PE10 tubing line as described above. Acquisitions were no longer than 20 minutes due to the small available blood volume of mice. Concurrently, imaging was performed using the same protocol as described (vide supra). The automated algorithm described above was

used to segment the LV and the myocardium of the mouse heart. The mean values of the ROI's in each PET frame were used to construct the LV and myocardium TACs. Partial volume and spillover corrected (PVSC) curves were calculated based on the recovery and spillover coefficients calculated in the phantom study. The PVSC curves were compared to the dispersion and delay-corrected curves to determine the accuracy of the partial volume and spillover correction. A certain amount of uncorrectable physiological dispersion would be expected between the two curves, given the distance that must be traveled between the left ventricle and the blood sampling site in the carotid artery. This would result in the peak of the blood sampled TAC being broader and the peak activity underestimated compared to the LV TAC. However, the amount of tracer delivered in the first pass and subsequent recirculation phases, which is measured by the area under the TAC (AUC), should be the same. Therefore, the AUC ratio of the corrected blood sampled and PVSC image-derived curves were compared ($AUC_{\text{image-derived}} / AUC_{\text{blood sampled}}$).

4.2.7 Metabolite and Plasma Fraction Correction

To correct for radiolabeled metabolites, the correction established by Slaets et. al. [27] in studies of nude mice with ^{18}F -FCH was applied to the PVSC corrected arterial TACs. Correction (also from Slaets) for whole blood to plasma fraction was also applied to correct for the fraction of ^{18}F -FCH that was bound to red blood cells.

4.2.8 Image Registration

CT Perfusion software was used to generate blood flow (BF), blood volume (BV), permeability surface-area product (PS), and extravascular volume (V_e) maps from the CT

Perfusion study. The dynamic average CT maps were then registered to the images acquired from the last acquired PET frame (55-60 min after injection of ^{18}F -FCH). The rigid registration was performed in 3D Slicer software (<http://www.slicer.org>) [28] and the CT functional maps were resampled to the PET space using the bilinear spline algorithm in 3D Slicer.

4.2.9 Kinetic Model

Uptake of ^{18}F -FCH in tissue was analyzed with the 3-compartment model. (Figure 4.4) The governing equations of the model are as follows:

$$\frac{dC_i}{dt} = K_1 C_a(t) - (k_2 + k_3) C_i(t) + k_4 C_m(t) \quad (8)$$

$$\frac{dC_m}{dt} = k_3 C_i(t) - k_4 C_m(t) \quad (9)$$

$$Q(t) = V_b C_a(t) + C_i(t) + C_m(t) \quad (10)$$

where $C_a(t)$ is the arterial TAC, $C_i(t)$ is the interstitial concentration of free tracer, K_1 is the influx rate constant in min^{-1} , k_2 is the efflux rate constant for the return of tracer from the interstitium back into blood vessels, k_3 is the binding rate constant to choline kinase in tissue, k_4 is the dissociation rate constant from the enzyme, $C_m(t)$ is the concentration of phosphocholine (i.e. the phosphorylated ^{18}F -FCH by choline kinase), and $Q(t)$ is the tissue TAC.

A linearized solution for the 3-Compartment model was derived based on the method described by Feng and Blomqvist [15, 16]. The different linearized solutions are

outlined in Table 4.1. The hybrid PET-CT Perfusion imaging technique imputes 3-compartment model parameters from an independent CT Perfusion study as discussed below.

Table 4.1: Linearized solutions of the 3-Compartment kinetic model.

Solution	<i>LIN-K1</i>
Imputed Parameters from CT Perfusion	K_1
Estimated Parameters	k_2, k_3, k_4
Linearized Equation	$Q(t) - K_1 \int_0^t C_a(u) du = -P_1 \left[\int_0^t Q(u) du \right] - P_2 \left[\int_0^t \int_0^T Q(u) du dT \right] + P_4 \left[K_1 \int_0^t \int_0^T C_a(u) du dT \right]$
Constraints	$P_1 \geq P_4$
Coefficients	$P_1 = k_2 + k_3 + k_4$ $P_2 = k_2 k_4$ $P_4 = k_3 + k_4$
Rate Constant Equations	$k_2 = P_1 - P_4$ $k_4 = P_2 / k_2$ $k_3 = P_4 - k_4$
Solution	<i>LIN-K1K2</i>
Imputed Parameters from CT Perfusion	K_1, k_2
Estimated Parameters	k_3, k_4
Linearized Equation	$Q(t) - K_1 \int_0^t C_a(u) du + k_2 \int_0^t Q(u) du = P_1 \left[K_1 \int_0^t \int_0^T C_a(u) du dT - \int_0^t Q(u) du \right] \dots$ $-P_2 \left[k_2 \int_0^t \int_0^T Q(u) du dT \right]$
Constraints	$P_1 \geq P_2$
Coefficients	$P_1 = k_3 + k_4$ $P_2 = k_4$
Rate Constant Equations	$k_4 = P_2$ $k_3 = P_1 - k_4$

The LIN-K1 and LIN-K1k2 solutions impute functional parameters K_1 and k_2 from an independent CT Perfusion study. The K_1 parameter was calculated knowing that $K_1 = FE$, where F is the blood flow (obtained from BF maps) and E is the extraction efficiency. E was calculated from CT functional maps of BF and PS: [29]

$$E = 1 - e^{\frac{-PS}{F}} \quad (11)$$

The extraction efficiency of CT contrast agent and ^{18}F -FCH are different because diffusion is dependent on the molecular weight of the solute. Prior membrane permeability experiments by Danielli [30] showed that a cubic root relationship exists between the diffusion of a solute in water and its molecular weight. Therefore, based on the molecular weight of contrast agent (Conray 43, 809.1 Da) and FCH (157.6 Da), the extraction efficiency was scaled by a scale factor E_{sc} :

$$E_{sc} = \frac{\sqrt[3]{809.1}}{\sqrt[3]{157.6}} = 1.725 \quad (4.12)$$

The K_1 parameter in the 3-compartment model was therefore calculated as:

$$K_1 = F \cdot E \cdot E_{sc} \quad (4.13)$$

The k_2 parameter was calculated from the CT functional maps knowing that $k_2 = K_1/V_e$, where V_e is obtained from the extravascular volume map.

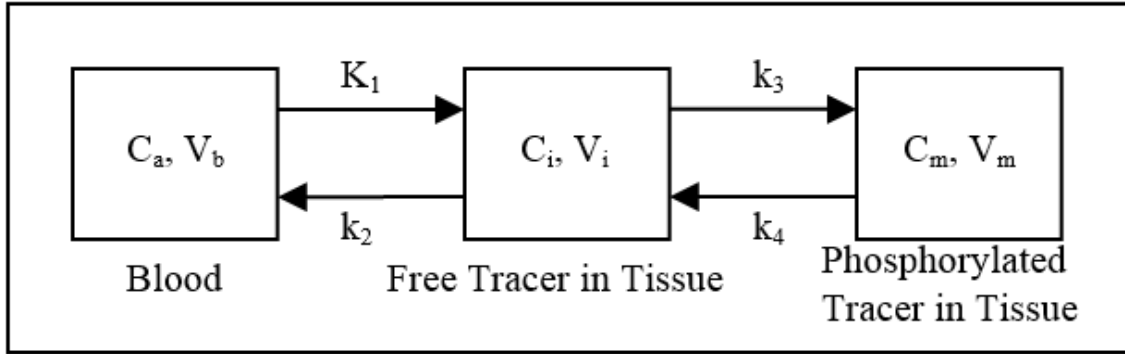


Figure 4.4: The 3-compartment kinetic model for uptake of ^{18}F -FCH in tissue.

4.2.10 Parametric Maps

The goodness of fit of both linearized solutions of the 3-compartment model to mean tumor TACs was assessed initially. The K_1 and k_2 parameters were obtained from the mean ROI values of the appropriate CT Perfusion functional maps (see above). The linearized solution that produced the best fit to the mean tissue ROI TAC was used to calculate parametric maps of the 3-compartment model parameters for all mouse PET studies.

To improve the signal-to-noise ratio (SNR) of voxel TACs for the kinetic analysis, a 3x3 box-filter was applied to the all dynamic PET images. For each voxel, a 3x3 grid is placed with the voxel as its center, and the original voxel value is replaced by the average value of all voxels within the grid. TAC noise can be quantified such as described by Logan: [31]

$$\langle f_N^Q \rangle_{N,t} = \text{avg} \left\{ \frac{\text{abs}(Q_n(t) - Q(t))}{Q(t)} \right\} \quad (4.14)$$

Where the noise factor $\langle f_N^Q \rangle_{N,t}$ is the average difference between the measured and fitted curves, averaged over all time points and curves. A noise simulation showed that with a TAC SNR = 10, the k_3 parameter can be estimated with a coefficient of variation of roughly 10% compared to approximately 25% for SNR = 4. To estimate the noise in a voxel TAC, an unpublished phantom study of our eXplore VISTA small animal PET scanner showed that the noise factor of a single voxel TAC is approximately 0.19, equivalent to an SNR of roughly 5. The study was performed with a dynamic scan of a cylindrical phantom filled with a 12 MBq/ml solution of FDG to approximate the FDG concentration in a mouse study, using the mouse imaging protocol described (vida supra) and the SNR was quantified by calculating the mean and variance of the images for each voxel TAC. It was determined using a noise simulation that averaging 9 TACs with SNR = 5 produced an averaged TAC with a SNR approximately equal to 10. Therefore, dynamic images were smoothed with a 3x3 box filter because its size was a reasonable trade-off between k_3 precision and spatial resolution.

All PET image analysis was performed with in-house software written in MATLAB 2015b (The MathWorks Inc., Natick, Massachusetts, United States). Parametric maps of k_3 and k_4 were generated by fitting dynamic TACs from the smoothed PET images with the hybrid PET-CTP technique, imputing the K_1 and k_2 parameters from the corresponding voxels of the registered CT Perfusion functional maps. Graphical analysis using the Logan Plot [32] was performed on the dynamic PET images to produce parametric maps of the distribution volume V_d . The linear range of the Logan Plot analysis was manually specified for each study according to the plot produced from the mean tumor ROI TAC. Finally,

images of the standardized uptake value (SUV) were calculated using PET frames acquired between 10-12, 28-30 and 55-60 minutes from initial injection of ^{18}F -FCH, denoted by SUV₁₂, SUV₃₀, and SUV₆₀, respectively.

Axial slices of the registered CT maps were used to manually segment tumors into 2-dimensional regions of interest (ROIs). The ROIs could then be overlaid onto the PET images for kinetic analysis. Tumor volume was calculated by multiplying the number of voxels in the ROI by the PET voxel volume.

4.2.11 Preliminary Immunohistochemistry

At the completion of all imaging studies, tumors in three mice were excised and formalin-fixed for 24 hours. Prior to excision, a needle was inserted into the tumor in the superior-inferior direction to keep track of orientation. Tumors were then embedded in paraffin and later sliced perpendicular to the needle track for immunohistochemistry analysis. The analysis was conducted using a primary polyclonal anti-choline kinase alpha (ChK α) antibody (Sigma Aldrich) stain at 1:10 dilution and without antigen retrieval because this processing condition provided sufficient signal without background saturation. Bronchial tissue was used as a positive control and the intensity of cytoplasmic and nuclear staining in the tumor cells was ranked as 1+, 2+ or 3+ for low, moderate and high intensity including nuclear staining, respectively.

4.2.12 Statistical Analysis

GraphPad Prism version 6.05 for Windows (GraphPad Software, La Jolla California USA, www.graphpad.com) was employed to examine correlations between

tumor volume and maximum ROI values: BF_{\max} , BV_{\max} , PS_{\max} , $K_{1\max}$, $k_{2\max}$, $k_{3\max}$, $k_{4\max}$, $V_{d\max}$, $SUV_{12\max}$, $SUV_{30\max}$ and $SUV_{60\max}$. Maximum values were investigated instead of mean ROI values because tumor tissue is highly heterogeneous and maxima would select the most active clone. The Shapiro-Wilk test for normality [33] indicated that the SUV variables followed a normal distribution, while the other functional parameters and tumor volume did not. The nonparametric Spearman correlation was utilized to calculate the Spearman correlation coefficient r between each functional parameter and tumor volume. Statistical significance for the correlations was set to $p < 0.05$.

The immunohistochemistry scores were compared to the $k_{3\max}$ values obtained from the tumor ROI's that were imaged prior to the excision of the tumor.

4.3 Results

4.3.1 Validation of Partial Volume and Spillover Correction

The parameters obtained for the fit to the measured blood counter TAC in response to a step change in activity were $k = 0.025 \text{ s}^{-1}$, $t_0 = 308 \text{ s}$ for the $10 \mu\text{l}/\text{min}$ case and $k = 0.1307 \text{ s}^{-1}$ for the $50 \mu\text{l}/\text{min}$ case (Figure). The partial volume and spillover coefficients calculated with the mouse heart phantom were $r_m = 0.42$, $s_{mb} = 0.18$, $r_b = 0.68$ and $s_{bm} = 0.17$, giving $\alpha = 1.64$ and $\beta = 0.70$. The dispersion-corrected blood sampled TAC of one mouse for the $10 \mu\text{l}/\text{min}$ case is shown in Figure 4.6 along with the image-derived TACs for the same mouse and the PVSC-TAC. A sample of corrected image-derived and blood sampled curves is shown in Figure 4.7.

The mean AUC ratios between the six PVSC image-derived TACs and blood sampled curves indicated that the area under the PVSC curves was roughly twice as large

as the blood sampled curves because the tail end of the PVSC curves was higher than that of the blood sample curves. (Figure 4.7) Given that the phantom partial volume and spillover correction did not yield good agreement in the AUC, an alternate approach was taken. In order to obtain experimentally derived values of α and β that implicitly corrected for the effect of partial volume, spillover, cardiac motion, and other sources of error, the LV and myocardium TACs were fitted to the dispersion corrected blood sampled TACs of the six mice using non-linear least squares regression and equation (4) as the operating equation. This technique determined the linear combination of scaled LV and myocardium TACs that would most accurately represent the blood sampled curves, which serve as the gold standard. This method resulted in values (mean \pm SD) of $\alpha = 1.46 (\pm 0.1)$ and $\beta = 0.86 (\pm 0.04)$. An example of a PVSC TAC using these values is shown in Figure 4.8. The mean AUC ratio for curves corrected with this method was 0.98 ± 0.09 (max = 1.12, min = 0.88). These mean values of α and β were used to correct the image derived LV TACs in the PET study.

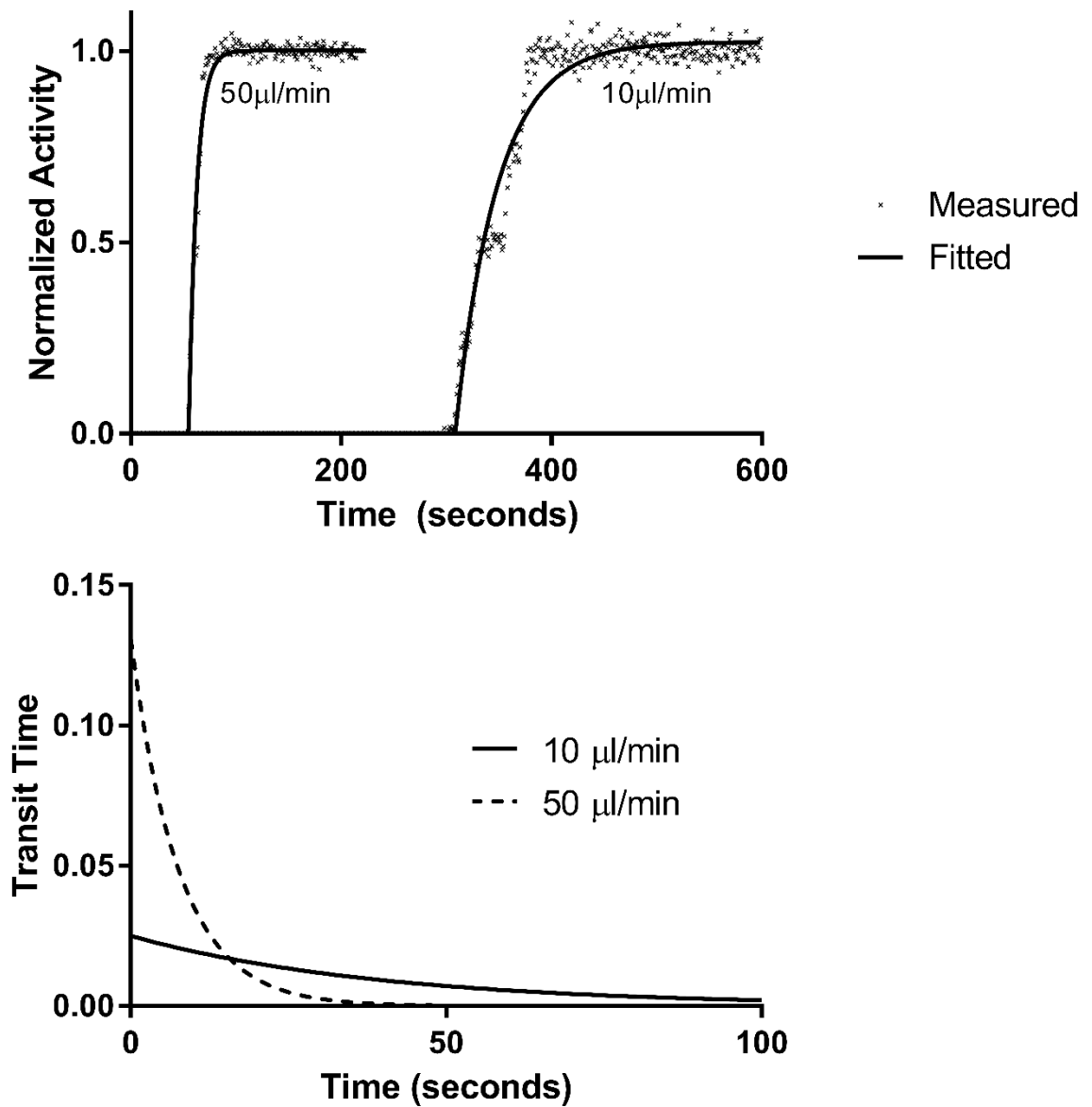


Figure 4.5: (Top) Blood counter TAC in response to a step change in activity measured at withdrawal speeds of 10 and 50 $\mu\text{l}/\text{min}$ along with the fitted exponential curves. Curves are shifted to aid visualization. (Bottom) Dispersion function $D(t)$ of

the blood counter corresponding to the measured TAC shown at top: 10 $\mu\text{l}/\text{min}$ (solid, $k = 0.025 \text{ s}^{-1}$) and 50 $\mu\text{l}/\text{min}$ (dashed, $k = 0.1307 \text{ s}^{-1}$).

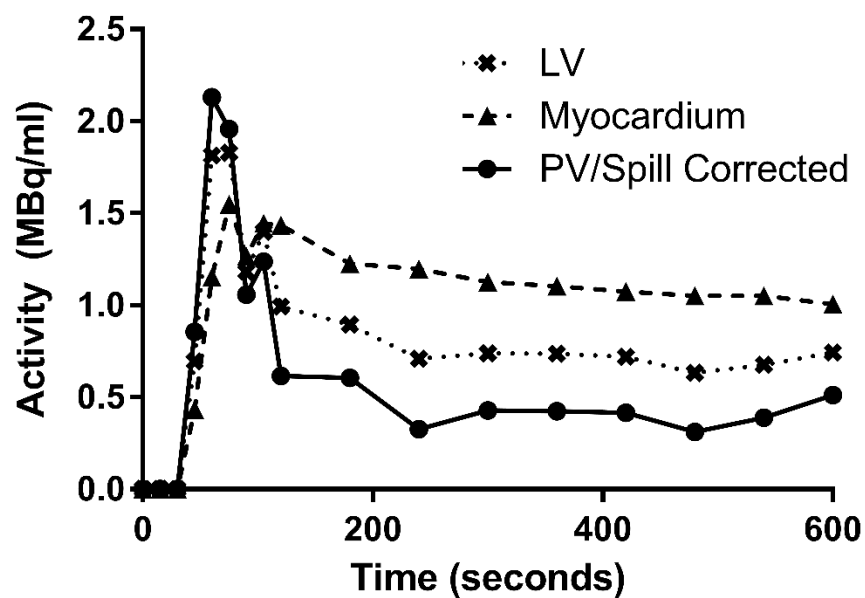
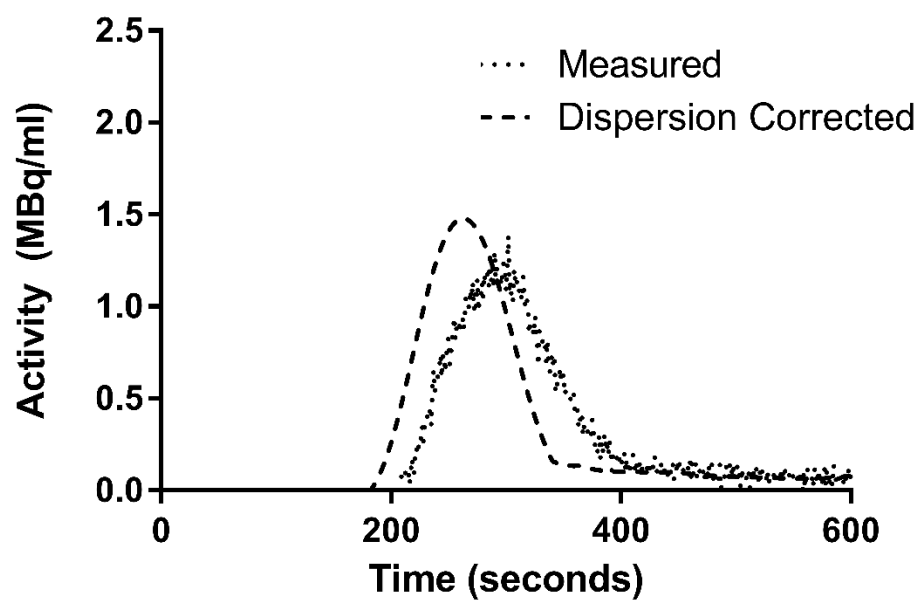


Figure 4.6: (Top) Blood-sampled arterial TAC at 10 $\mu\text{l}/\text{min}$ and dispersion corrected TAC for one mouse study. (Bottom) Image-derived TACs from LV and myocardium ROIs as well as the partial volume and spillover corrected TAC from the same mouse.

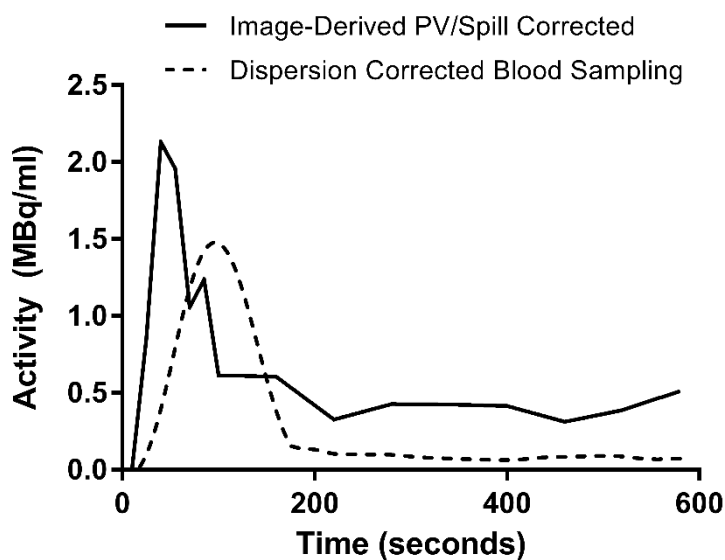


Figure 4.7: Example of image-derived, partial volume and spillover corrected arterial TAC from LV and dispersion corrected blood sampled arterial TAC from one tail artery at 10 $\mu\text{l}/\text{min}$.

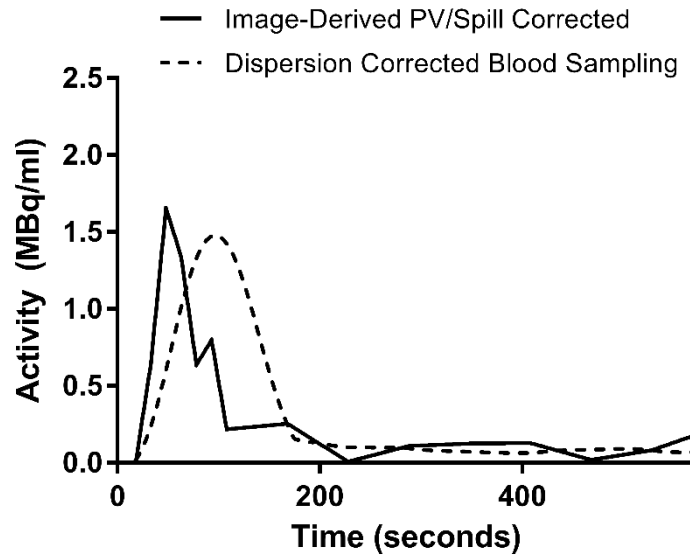


Figure 4.8: Image-derived PVSC TAC obtained using fitted values of α and β .

4.3.2 Selecting the Best Model

The PVSC arterial TAC and the mean tumor ROI TAC are shown in Figure 4.9 along with the fits from both the LIN-K1 and LIN-K1k2 model solutions. The LIN-K1k2 model did not produce a good fit since it was unable to properly fit the initial portion of the tumor TAC. An explanation for this is provided in the Discussion. The Akaike information criterion [34] confirmed that the LIN-K1 model produced a better fit. The K_1 measured by CT Perfusion was 0.09 ml/min/g and the fit produced the following parameter values: $k_2 = 0.37 \text{ min}^{-1}$, $k_3 = 0.25 \text{ min}^{-1}$, $k_4 = 0.01 \text{ min}^{-1}$.

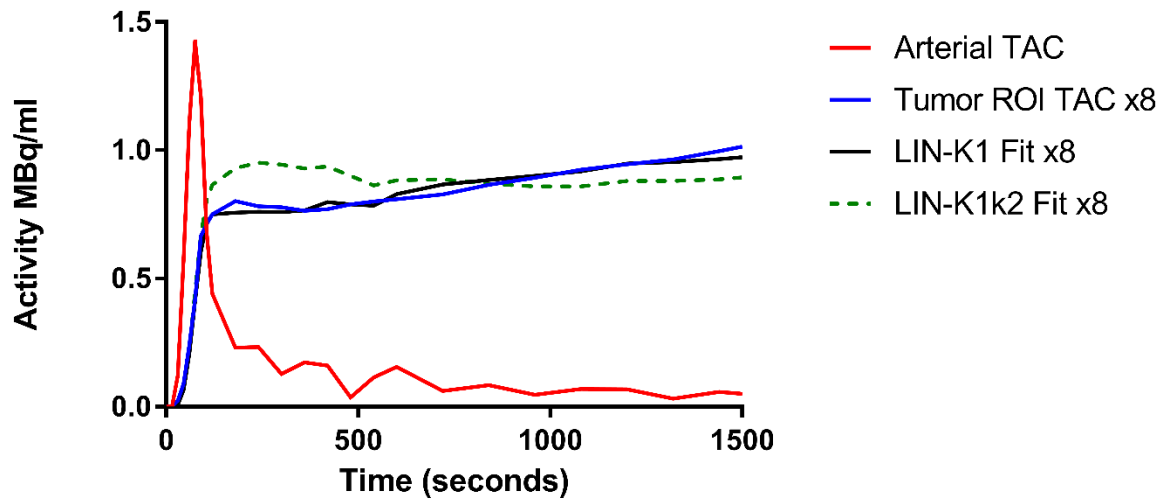


Figure 4.9: Model fits of a mean tumor ROI TAC from a PC-3 hybrid PET-CTP study, produced by both linearized model solutions. The tumor TAC and the fitted TACs are scaled up by a factor of 8 to aid visibility. The LIN-K1k2 model was unable to fit the initial portion of the tumor ROI TAC, leading to a poor fit for the entire curve. The LIN-K1 model solution produced a good fit to the data.

4.3.3 Parametric Maps

Example CT Perfusion functional maps for one mouse are shown in Figure 4.10. In this example, the tumor volumes at days 64, 69 and 94 were 0.18, 0.23 and 0.43 cc, respectively. At day 94, a hypovascular tumor core was visible, indicated by low values of BV and PS. The BF in the tumor was heterogeneous when the hypovascular core was discernible on the BV and PS maps.

The SUV_{60} and V_d parametric maps for the same slices are shown in Figure 4.11 and the 3-compartment parametric maps are shown in Figure 4.12. The SUV_{60} map showed

generally poor contrast throughout the tumor. The Logan distribution volume map was generally uniform throughout the tumor, however there were small regions with elevated V_d at days 69 and 94. The K_1 map showed elevated blood flow throughout the tumor at the earliest time point, while at later time points the elevated K_1 was located around the hypovascular core, on the tumor rim. The k_2 and k_3 parameters were generally higher on the tumor rim and low in the necrotic core. The k_4 parameter was negligible at the earliest time point, but increased at later time points. Generally, tumor features were more discernible on parametric maps compared to SUV maps, owing to the more favorable contrast in the parametric maps.

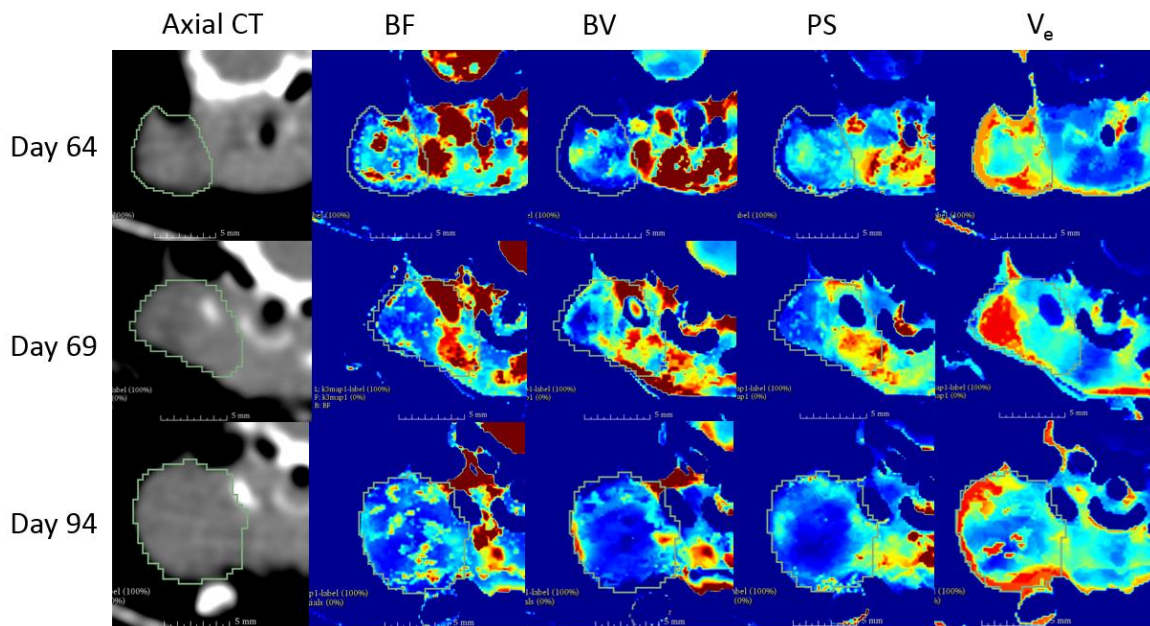


Figure 4.10: CT Perfusion functional maps of a PC-3 tumor at days 64, 69 and 94 post implantation. The tumor's necrotic core is visible on the PS map at day 94. Tumor is outlined by the green contour in axial CT images. (BF = blood flow (0-100

ml/min/100g), BV = blood volume (0-10 ml/min/100g), PS = permeability (0-60 ml/min/100g), V_e = extravascular volume (0-100 ml/min/g))

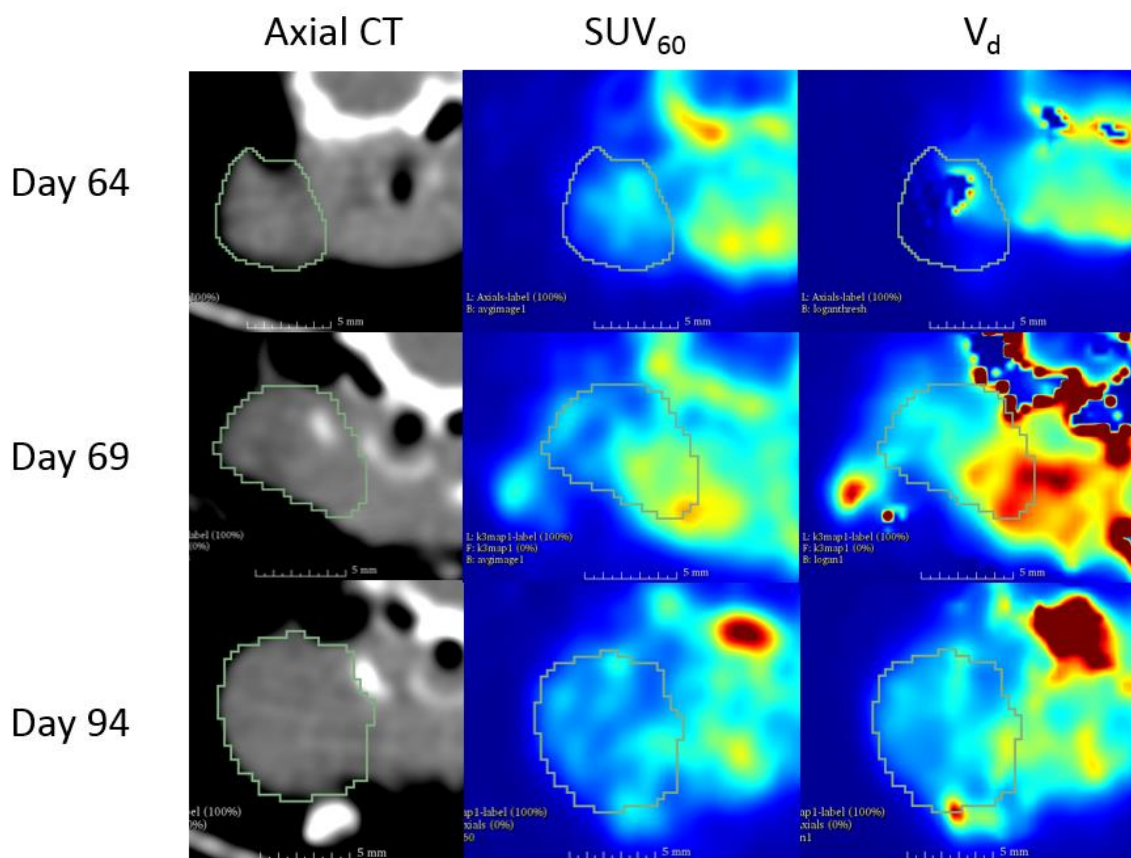


Figure 4.11: Maps showing SUV₆₀ and the distribution volume (V_d) from the Logan Plot analysis. (SUV₆₀ = standardized uptake value from 55-60 minutes (0-2), V_d (0-10 ml/g))

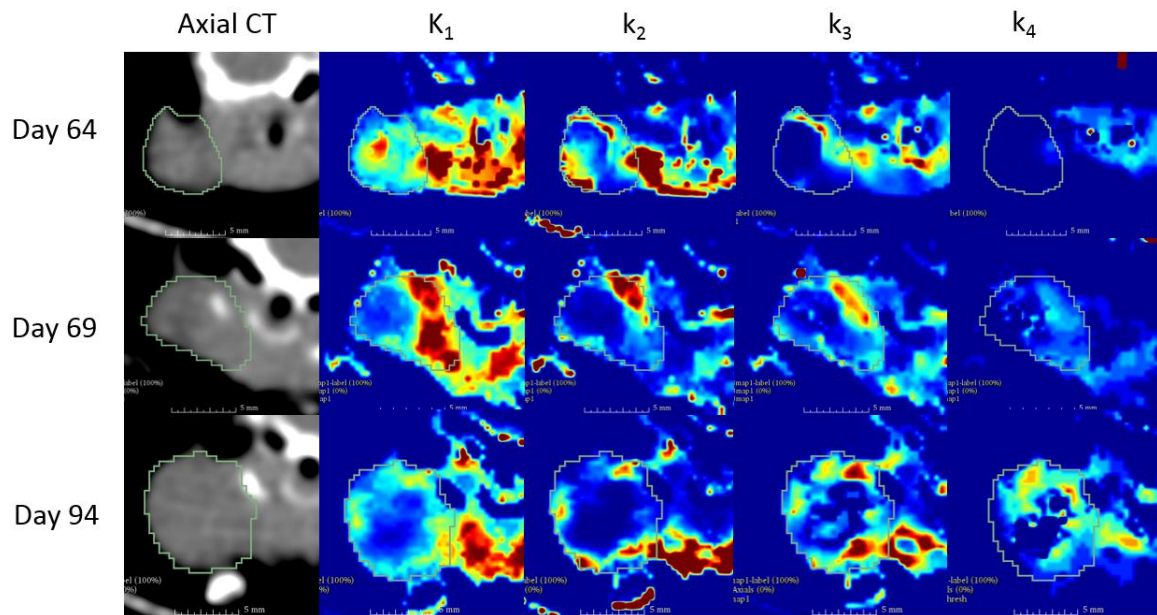


Figure 4.12: PET parametric maps of the same PC-3 mouse tumor as Figure 4.10 and Figure 4.11 at days 64, 69 and 94. The SUV_{60} and V_d parametric maps show poor tumor contrast, while the tumor core and rim are much more discernible on the rate constant maps. (K_1 (0-0.5 ml/min/g), k_2 (0-2 min⁻¹), k_3 (0-0.5 min⁻¹), k_4 (0-0.1 min⁻¹))

4.3.4 Tumor Volume Correlation

Statistical analysis with the Spearman correlation showed that out of all functional parameters, tumor volume was the most significantly correlated with k_{3max} ($r = 0.63$, $p < 0.001$). (Figure 4.13) Tumor volume was also significantly correlated with k_{2max} ($r = 0.59$, $p < 0.001$), K_{1max} ($r = 0.51$, $p < 0.01$), V_{dmax} ($r = 0.57$, $p < 0.01$), k_{4max} ($r = 0.43$, $p < 0.05$), BF_{max} ($r = 0.49$, $p < 0.01$), BV_{max} ($r = 0.43$, $p < 0.05$), and PS_{max} ($r = 0.42$, $p < 0.05$). No significant correlation was found between tumor volume and any of the SUV parameters tested. (Figure 4.13)

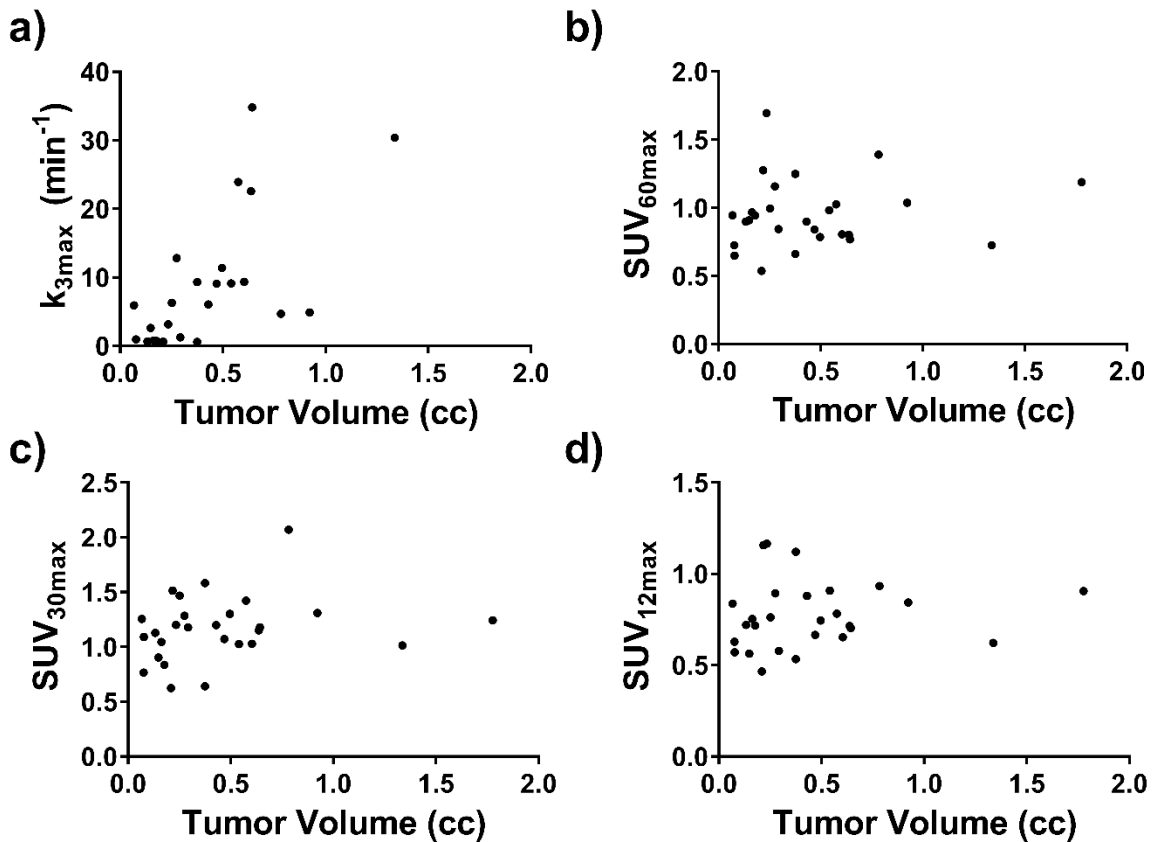


Figure 4.13: a) Plot of $k_{3\max}$ vs. tumor volume. The Spearman correlation coefficient was $r = 0.63$, $p < 0.001$. b) No significant correlation was found between tumor volume and b) $SUV_{60\max}$, c) $SUV_{30\max}$ and d) $SUV_{12\max}$.

4.3.5 Immunohistochemistry

No correlation was found between ChK α expression from immunohistochemistry and the $k_{3\max}$ parameter from parametric maps in the three samples tested. In one sample, there appeared to be a geographic correspondence between an area of higher ChK α expression and a high k_3 region of the tumor's rim as indicated on the parametric map. (Figure 4.14)

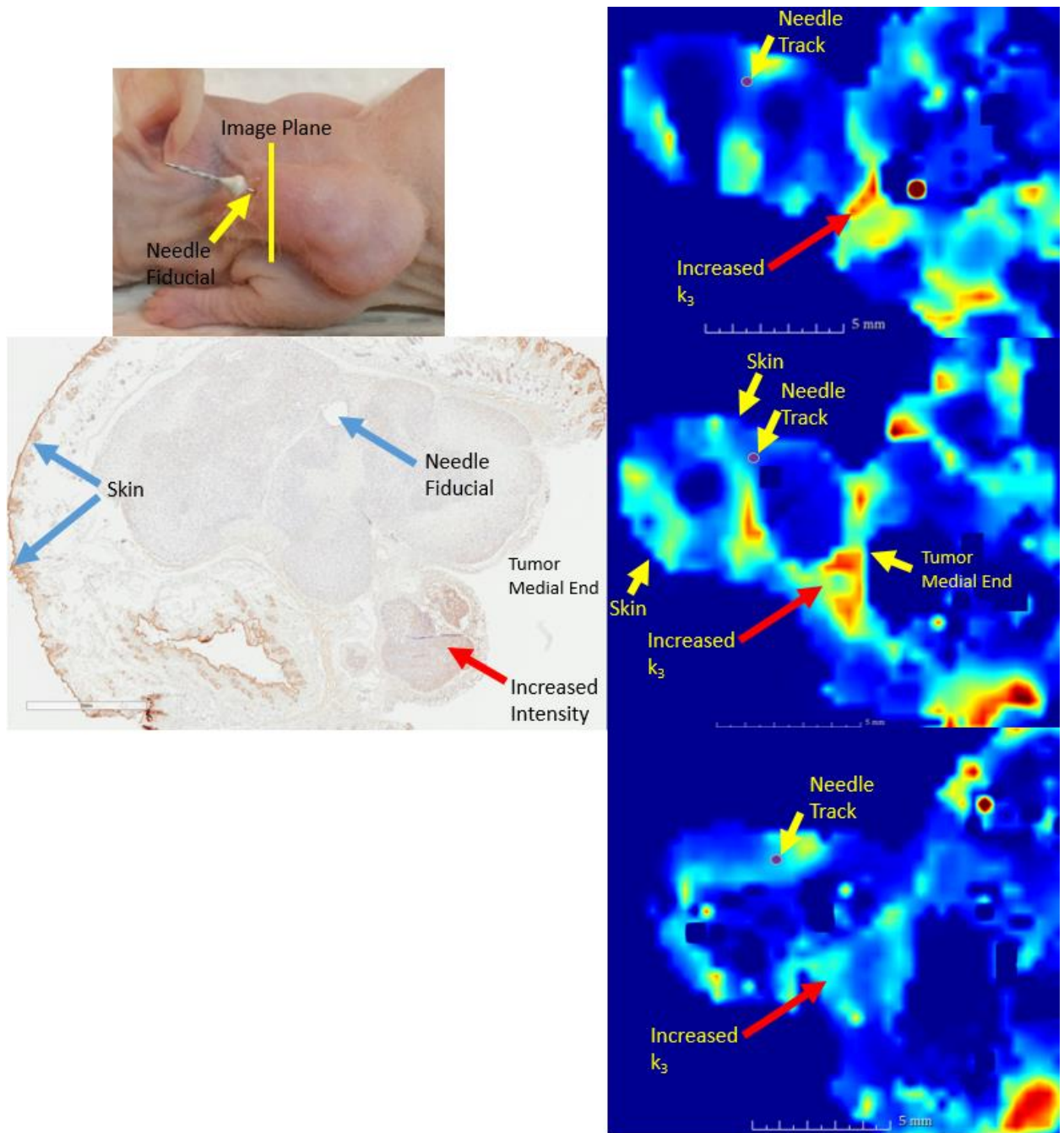


Figure 4.14: (Top left) Post-imaging, a needle (yellow arrow) was inserted into the tumor to serve as the fiducial in orienting the immunohistochemical stain with the imaging results. Both histology and image slices were cut perpendicularly to the

needle track. The image plane (yellow line) marks the approximate location of the axial slice seen in the histology image. (Left) ChK α stained slide. An arrow (blue) indicates the needle track and the red arrow indicates an area of relatively high ChK α expression on the medial side of the tumor. The skin (blue arrows) marks the outer edge of the tumor. (Right) The middle k_3 map (0-0.5 min⁻¹) corresponds to the histology slide. The red arrow indicates an area of relatively high k_3 . Superior and inferior slices are located above and below the middle slice, respectively (slice thickness = 0.8 mm). The estimated location of the needle track is indicated in the k_3 maps.

4.4 Discussion

This work demonstrates the feasibility of rapidly generating PET parametric maps from hybrid PET-CT Perfusion imaging. This technique has potential applications for the measurement of choline kinase activity with ¹⁸F-FCH PET imaging as well as for other PET tracer imaging studies in which the k_3 parameter may be of interest.

Poor agreement was observed in terms of the AUC between the image-derived phantom-based PVSC TACs and the dispersion corrected blood sampled TACs. This suggests that the phantom-based partial volume and spillover correction does not accurately represent the true effects observed in the mouse heart during a PET study. The mouse heart phantom does not account for cardiac motion, an effect that causes the myocardium to move radially in and out very rapidly. The result is that the temporal averaging over the length of time of the PET frame causes smearing of the myocardium activity in the image, leading to an overestimated myocardium thickness and hence a

smaller observed LV diameter compared to those measured *ex-vivo* with calipers. Given that the phantom did not account for cardiac motion, a new approach was used. This effect was accounted for by fitting equation (4) to the data and obtaining estimates of α and β . This technique represents an experimentally derived way to implicitly account for the effects of partial volume, spillover, cardiac motion, and any other sources of error that might be present. For this method, the AUC ratio between the corrected image-derived curves and blood sampled curves was close to unity, suggesting that this technique holds promise for obtaining image-derived arterial TACs in studies of mice. However, the dispersion corrected blood sampled TAC is still wider than the image-derived PVSC TAC suggesting there is still additional dispersion or other sources of error that are not corrected for. These unaccounted factors include: 1) physiological dispersion that occurs between the LV and arterial blood sampling site (carotid artery), 2) the shorter PET acquisition frames in the first phase of the image-derived curves are noisy, reducing the accuracy of these measurements, and 3) the myocardium chamber in the phantom surrounds a cylindrical LV chamber, while a real LV more closely approximates an ellipsoid.

We sampled arterial blood at a withdrawal speed of 10 $\mu\text{l}/\text{min}$ given the small blood volume available in a mouse. The dispersion experiment with the blood counter at this slow withdrawal speed resulted in a TAC which was not monotonically increasing as expected, but rather had three flat sections where the measured activity remained the same for a short time (see Figure 4.15). This was due to the slow pumping speed in combination with the design of the detector insert of the blood counter in which the tubing looped back around three times within the insert. While the straight portions of the loops are within the field of

view (FOV) of the detector, the curvilinear part of the loops are outside as shown in Figure 4.15. When activity reaches each of these curvilinear portions of the loop, it will exit from the field of the detector and result in a short equilibrium (plateau) in the TAC. The cause of this effect was confirmed by running the experiment with a faster withdrawal speed of 50 $\mu\text{l}/\text{min}$, in which the bolus rounded the three curvilinear portions of the loop fast enough to produce a smooth monotonically increasing TAC (Figure 4.5).

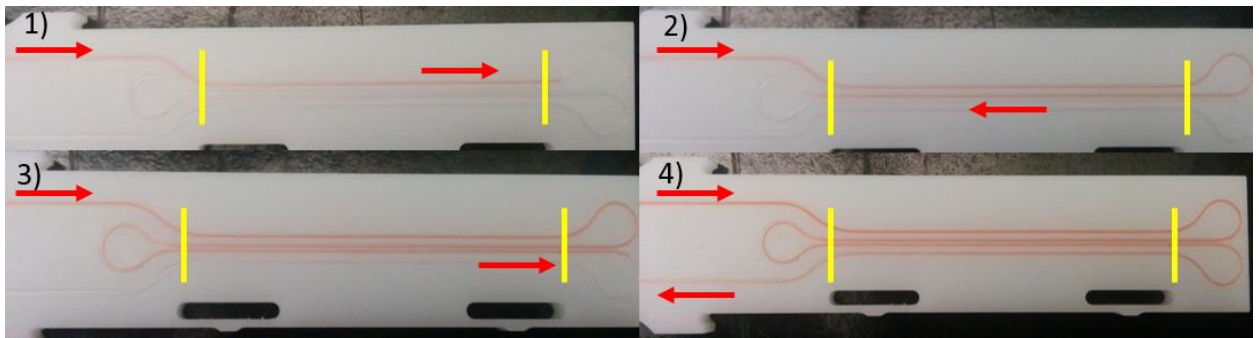


Figure 4.15: The progression of blood flow through PE10 tubing in the blood counter insert, ordered from steps 1 to 4. Red arrows indicate the direction of flow and the yellow lines indicate a rough estimate of the edge of the FOV of the blood counter detector. The number of counts increases as more blood enters the detection area. The number of counts detected by the counter reaches a plateau when the front end of the flow passes beyond the yellow line and into the curvilinear portion of the tubing. The number of counts in the TAC begins to increase again when the front end of the flow passes beyond the curvilinear portion and back into the detector range.

The kinetic models investigated here did not include a blood volume term, since previous work as well as work by other investigators have found that blood volume in FCH

imaging of tumors is small enough for its influence on the model fit to be negligible. [27] This is not likely due to an actual lack of blood volume in tissue, but rather because the averaging of activity over the length of a typical first-phase acquisition frame (10-15 seconds) causes underestimation of the peak activity of the bolus. This was confirmed by generating an instantaneous TAC with the 3-compartment model with a small blood volume ($V_b = 0.05$ ml/g) and then simulating the effect of the frame averaging on the model's estimate of blood volume. It was found that the frame averaging reduced the estimated blood volume to zero in the majority of cases. Nevertheless, the correlation results in this work (Figure 4.13) were re-run with parametric maps calculated with a blood volume term, and it was found that there was no discernable difference in the results.

The LIN-K1 model solution was used to produce parametric maps because the LIN-K1k2 was unable to produce a good fit to the tumor ROI tissue curve. The K_1 and k_2 parameters govern the shape of the initial part of the tissue TAC, while the k_3 and k_4 parameters affect the later phase of the TAC. (Figure 4.16) The LIN-K1k2 could not produce a good fit because of a discrepancy between the K_1 and k_2 parameters measured by the Johnson-Wilson model from a CT Perfusion study and the ones measured by the PET compartmental model. This discrepancy is due to a difference in the impulse residue functions (IRF) of the Johnson-Wilson model and the compartment model. The difference is that the Johnson-Wilson model accounts for mean transit time through the capillary bed, while the compartment model assumes that this transit is instantaneous. This effect can be seen in Figure 4.17.

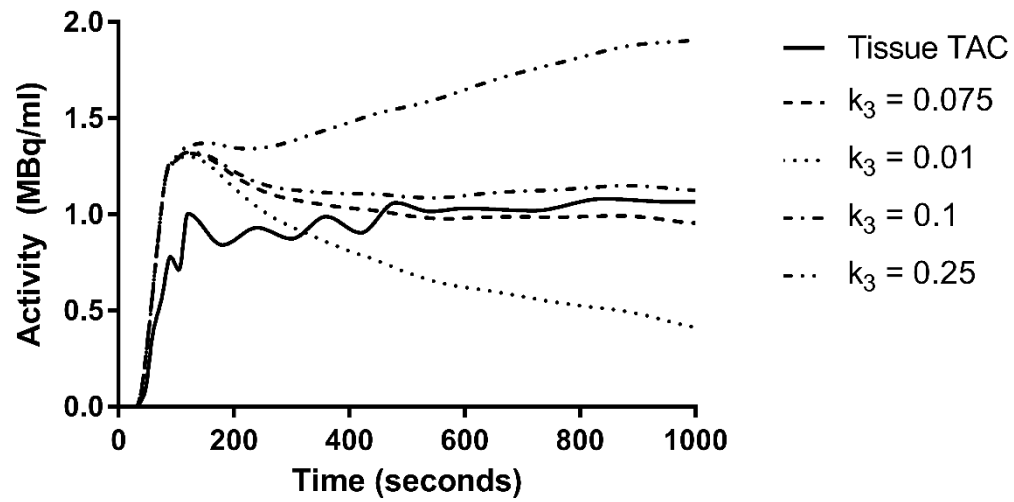


Figure 4.16: A tissue TAC measured with PET. The dashed curves use K_1 and k_2 parameters (scaled to account for differences in extraction efficiency) measured with the Johnson-Wilson model from an independent CT Perfusion study, and show the effect of varying k_3 . With K_1 and k_2 held fixed, a good fit cannot be achieved because the k_3 parameter only affects the later part of the curve. (k_3 is in min^{-1})

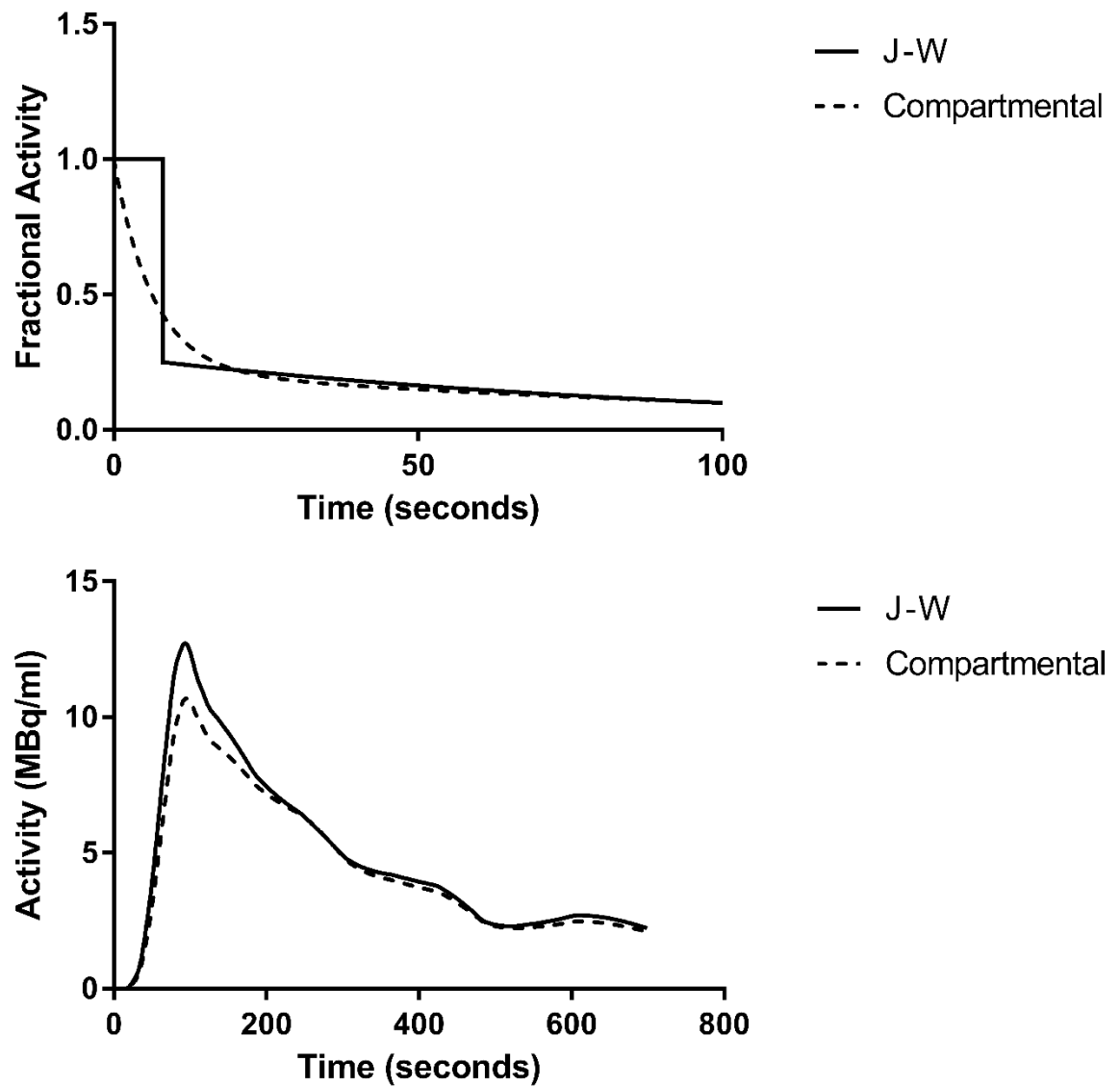


Figure 4.17: (Top) Impulse residue functions for the Johnson-Wilson and compartment models. The Johnson-Wilson model accounts for mean transit time through the capillary bed, while the compartment model assumes instantaneous passage. (Bottom) Resulting tissue curves using the same parameters with different

models. The Johnson-Wilson model results in a higher peak activity in the tissue curve.

Previous studies on the detection of PCa with FCH PET have shown poor contrast between malignant and benign or healthy prostate tissues. [11-13] These findings are consistent with the results of our work. SUV maps of PC-3 human prostate tumors in mice showed poor contrast between tumor core and rim as well as with surrounding tissue. Parametric maps of the PET parameters showed more tumor contrast than the SUV maps. In addition, the lack of any observed significant correlation between the SUV and tumor size adds further strength to the suggestion that SUV may not be useful in this application. Results of this work show that parametric maps show more tumor details and that there was a significant correlation between the $k_{3\max}$ parameter and tumor volume. This suggests that quantitative analysis may prove more useful for detection of PCa with ^{18}F -FCH PET. In addition, the hybrid PET-CT Perfusion imaging technique shows promise for providing more accurate targeting for biopsy and radiation dose escalation.

The Logan Plot distribution volume was also significantly correlated with tumor volume, though the correlation was not as strong as with $k_{3\max}$. This is not surprising, since by definition, V_d depends on all rate constants K_1 through k_4 . [35] Graphical analysis with the Logan Plot may be useful for quantitative analysis of ^{18}F -FCH PET studies on PCa, particularly in centers which are not equipped with the ability to perform CT Perfusion scans. Further investigations are warranted to determine the sensitivity and specificity of this analysis *in vivo*.

Previous studies investigating radiolabeled choline tracers have assumed irreversible binding ($k_4 = 0$) and have performed analysis with the Patlak Plot. [27, 36, 37] While the influx constant K_i from the Patlak Plot has been found to be correlated with SUV, [37] our results show that for larger tumor volumes, k_4 was non-zero and in some instances was as high as 0.1 min^{-1} in PC-3 tumors. This signifies that FCH may undergo reversible binding in larger prostate tumors and that the Logan Plot is likely more appropriate since it is intended for reversible tracers (while the Patlak Plot is for irreversible tracers). In addition, it may be important to include the k_4 parameter in the kinetic model when the goal is to quantify k_3 . Failure to do so when k_4 is non-negligible would result in bias in the estimates of other model parameters due to the inability of the model to accurately describe the measured data.

Preliminary immunohistochemistry results were mixed. In the three samples tested, there was no correlation between the $k_{3\text{max}}$ parameter in the tumor ROI and ChK α expression. However, in one sample there appeared to be a correspondence between these two variables in the medial portion of the tumor's rim. This may indicate that ChK α is overexpressed in localized regions of the tumor rim. No firm conclusions can be drawn due to the small sample size, and further investigation is required to determine if the k_3 parameter is an accurate measure of choline kinase activity.

4.5 Conclusions

This work presents a novel implementation of kinetic modeling with hybrid PET-CT Perfusion imaging. Image-derived arterial time activity curves can be measured using partial volume and spillover coefficients measured with a mouse phantom and these curves

show good agreement with blood sampled curves. The hybrid imaging technique enables fast generation of PET parametric maps, which can be used to improve tumor contrast and has the potential for differentiating malignant from benign or healthy prostate tissue. Further investigation is required to determine whether the k_3 parameter is an accurate measure of choline kinase activity. This PET-CT Perfusion hybrid imaging technique has many other potential applications other than PCa imaging, specifically for measuring the binding rate constant k_3 for other PET tracers in a variety of pathologies.

4.6 References

1. Bauman, G., et al., *18F-fluorocholine for prostate cancer imaging: a systematic review of the literature*. Prostate Cancer Prostatic Dis, 2012. **15**(1): p. 45-55.
2. Kirienko, M., et al., *Applications of PET imaging with radiolabelled choline (11C/18F-choline)*. Q J Nucl Med Mol Imaging, 2015. **59**(1): p. 83-94.
3. Rontein, D., et al., *Plants synthesize ethanolamine by direct decarboxylation of serine using a pyridoxal phosphate enzyme*. J Biol Chem, 2001. **276**(38): p. 35523-9.
4. Li, Z. and D.E. Vance, *Thematic Review Series: Glycerolipids. Phosphatidylcholine and choline homeostasis*. Journal of Lipid Research, 2008. **49**(6): p. 1187-1194.
5. Glunde, K., M.A. Jacobs, and Z.M. Bhujwalla, *Choline metabolism in cancer: implications for diagnosis and therapy*. Expert Rev Mol Diagn, 2006. **6**(6): p. 821-9.
6. Challapalli, A., et al., *Exploiting altered patterns of choline kinase- α expression on human prostate tissue to prognosticate prostate cancer*. J Clin Pathol, 2015. **68**(9): p. 703-9.

7. Swanson, M.G., et al., *Quantification of choline- and ethanolamine-containing metabolites in human prostate tissues using 1H HR-MAS total correlation spectroscopy*. Magnetic Resonance in Medicine, 2008. **60**(1): p. 33-40.
8. Beauregard, J.M., et al., *Pilot comparison of F-fluorocholine and F-fluorodeoxyglucose PET/CT with conventional imaging in prostate cancer*. Journal of medical imaging and radiation oncology, 2010. **54**(4): p. 325-332.
9. Husarik, D.B., et al., *Evaluation of [(18)F]-choline PET/CT for staging and restaging of prostate cancer*. Eur J Nucl Med Mol Imaging, 2008. **35**(2): p. 253-63.
10. Heinisch, M., et al., *Positron emission tomography/computed tomography with F-18-fluorocholine for restaging of prostate cancer patients: meaningful at PSA < 5 ng/ml?* Mol Imaging Biol, 2006. **8**(1): p. 43-8.
11. Schmid, D.T., et al., *Fluorocholine PET/CT in Patients with Prostate Cancer: Initial Experience*. Radiology, 2005. **235**(2): p. 623-628.
12. Igerc, I., et al., *The value of 18F-Choline PET/CT in patients with elevated PSA-level and negative prostate needle biopsy for localisation of prostate cancer*. European Journal of Nuclear Medicine & Molecular Imaging, 2008. **35**(5): p. 976-983.
13. Cimitan, M., et al., *[18F]fluorocholine PET/CT imaging for the detection of recurrent prostate cancer at PSA relapse: experience in 100 consecutive patients*. Eur J Nucl Med Mol Imaging, 2006. **33**(12): p. 1387-98.
14. Muzi, M., et al., *Kinetic analysis of 3'-deoxy-3'-18F-fluorothymidine in patients with gliomas*. J Nucl Med, 2006. **47**(10): p. 1612-21.
15. Feng, D., et al., *An unbiased parametric imaging algorithm for nonuniformly sampled biomedical system parameter estimation*. IEEE Trans Med Imaging, 1996. **15**(4): p. 512-8.
16. Blomqvist, G., *On the construction of functional maps in positron emission tomography*. J Cereb Blood Flow Metab, 1984. **4**(4): p. 629-32.

17. Blais, A.R., et al., *Quantitative Functional Imaging with Hybrid PET-CT Via Improved Kinetics Modeling: Application to 18F-Fluorocholine PET Imaging of Prostate Cancer*, in *World Congress on Medical Physics and Biomedical Engineering, June 7-12, 2015, Toronto, Canada*, A.D. Jaffray, Editor. 2015, Springer International Publishing: Cham. p. 154-157.
18. Breeuwsma, A.J., et al., *In vivo uptake of [11C]choline does not correlate with cell proliferation in human prostate cancer*. *European journal of nuclear medicine and molecular imaging*, 2005. **32**(6): p. 668-673.
19. Cenic, A., et al., *Dynamic CT Measurement of Cerebral Blood Flow: A Validation Study*. *American Journal of Neuroradiology*, 1999. **20**(1): p. 63-73.
20. Wang, Z., H. Shi, and H. Wang, *Functional M(3) muscarinic acetylcholine receptors in mammalian hearts*. *British Journal of Pharmacology*, 2004. **142**(3): p. 395-408.
21. Evans, R., *The Atomic Nucleus*. 1972, New York: McGraw-Hill.
22. Shoghi, K.I., et al. *Characterization of Spillover and Recovery Coefficients in the Gated Mouse Heart for Non-Invasive Extraction of Input Function in microPET Studies: Feasibility and Sensitivity Analysis*. in *Nuclear Science Symposium Conference Record, 2006. IEEE*. 2006.
23. Iida, H., et al., *Error analysis of a quantitative cerebral blood flow measurement using H₂(15)O autoradiography and positron emission tomography, with respect to the dispersion of the input function*. *J Cereb Blood Flow Metab*, 1986. **6**(5): p. 536-45.
24. Convert, L., et al., *A new tool for molecular imaging: the microvolumetric beta blood counter*. *J Nucl Med*, 2007. **48**(7): p. 1197-206.
25. Munk, O.L., S. Keiding, and L. Bass, *A method to estimate dispersion in sampling catheters and to calculate dispersion-free blood time-activity curves*. *Medical Physics*, 2008. **35**(8): p. 3471-3481.
26. Gamel, J., et al., *Pitfalls in Digital Computation of the Impulse Response of Vascular Beds from Indicator-Dilution Curves*. *Circulation Research*, 1973. **32**(4): p. 516-523.

27. Slaets, D. and F. De Vos, *Comparison between kinetic modelling and graphical analysis for the quantification of [18F]fluoromethylcholine uptake in mice*. EJNMMI Res, 2013. **3**(1): p. 66.
28. Fedorov, A., et al., *3D Slicer as an image computing platform for the Quantitative Imaging Network*. Magn Reson Imaging, 2012. **30**(9): p. 1323-41.
29. Lee, T.Y., T.G. Purdie, and E. Stewart, *CT imaging of angiogenesis*. Q J Nucl Med, 2003. **47**(3): p. 171-87.
30. Danielli, J.F., *Theory of penetration of a thin membrane, Appendix A*, in *The Permeability of Natural Membranes (Theory of penetration of a thin membrane, Appendix A)*. 1952, University Press: Cambridge.
31. Logan, J., et al., *A strategy for removing the bias in the graphical analysis method*. J Cereb Blood Flow Metab, 2001. **21**(3): p. 307-20.
32. Logan, J., *Graphical analysis of PET data applied to reversible and irreversible tracers*. Nucl Med Biol, 2000. **27**(7): p. 661-70.
33. Shapiro, S.S. and M.B. Wilk, *An analysis of variance test for normality (complete samples)*. Biometrika, 1965. **52**(3-4): p. 591-611.
34. Glatting, G., et al., *Choosing the optimal fit function: Comparison of the Akaike information criterion and the F-test*. Medical Physics, 2007. **34**(11): p. 4285-4292.
35. Innis, R.B., et al., *Consensus nomenclature for in vivo imaging of reversibly binding radioligands*. J Cereb Blood Flow Metab, 2007. **27**(9): p. 1533-9.
36. Kristian, A., et al., *Positron emission tomography and pharmacokinetics of 2-[18F]-fluoroethyl choline for metabolic studies in breast cancer xenografts*. Acta Oncol, 2014. **53**(8): p. 1086-92.
37. Sutinen, E., et al., *Kinetics of [(11)C]choline uptake in prostate cancer: a PET study*. Eur J Nucl Med Mol Imaging, 2004. **31**(3): p. 317-24.

Chapter 5

5 Conclusions and Future Work

5.1 Summary

The primary goals of this thesis were to investigate the effect of venous dispersion on the distribution volume measurement with the Logan Plot, and to simulate and implement a hybrid PET-CT Perfusion (CTP) imaging technique with a linearized solution of the 3-compartment model in an effort to accurately quantify the binding rate constant k_3 and generate parametric maps in a timely manner. In the case of ^{18}F -FCH PET, the k_3 parameter is related to the activity of choline kinase or the phosphorylation rate of choline that leads to incorporation of choline into the cell membrane.

This chapter will outline the main findings of this thesis and discuss the clinical implications of its results. In addition, it will include a discussion of future work required to determine the utility of these techniques in a clinical setting.

5.2 Venous TACs for the Logan Plot

Results from Chapter 2 showed that venous dispersion does not have a significant effect on ^{18}F -FCH distribution volume measurements with the Logan Plot. While these were simulated results and must be validated *in vivo*, they show promise for the use of venous TACs for graphical analysis of *in vivo* ^{18}F -FCH PET studies. In addition, the results would likely be similar for PET tracers that have a similar extraction efficiency, such as tracers with a similar molecular weight like ^{18}F -FCH. This would improve patient comfort

in quantitative PET studies in which there is no viable reference region or large arteries available in the images.

Results show that the distribution volume measured with the Logan Plot was also correlated with PC-3 tumor volume in mice. This warrants further investigation in patient imaging studies of prostate cancer (PCa) because it may be useful in centers that are not equipped to do CTP scans.

Previous investigations of ^{18}F -FCH PET imaging of PCa have employed graphical analysis with the Patlak Plot under the assumption that the dissociation constant k_4 is negligible. [1-3] In Chapter 4, PET-CT Perfusion parametric maps were generated with the LIN-K1 model. Maps of the k_4 parameter showed that this parameter was low in small tumours and higher in larger tumours. This finding suggests that the assumption of irreversible binding of ^{18}F -FCH may be invalid for larger tumours. The Logan Plot is a graphical analysis that is applicable to reversibly bound tracers and thus may be more appropriate for this application. The potential mechanism for this phenomenon may involve prostatic acidic phosphatase, an enzyme that catalyzes the dephosphorylation of choline phosphate. Like PSA today, plasma levels of this enzyme were previously of interest as a blood marker for prostate cancer. [4] More recently, there has been interest in reviving the prostatic acidic phosphatase test with the goal of identifying patients with intermediate to high risk prostate cancer. [5] The results of this thesis indicated that k_4 was non-zero and that $k_{4\text{max}}$ was significantly correlated with tumour volume, possibly due to increased acidic phosphatase activity in larger tumours. This is an interesting finding and builds a strong case for the investigation of the hybrid PET-CT Perfusion imaging

technique developed in this thesis, as it may be useful to obtain an independent, precise estimate of the k_4 parameter as a biomarker for prostatic acidic phosphatase activity.

5.3 Robust Measurement of the Binding Rate Constant

Historically, it has been very challenging to obtain accurate estimates of the binding rate constant k_3 using compartment models. Parameter estimates have shown high variability [1] and the covariance between model parameters has proven to be a significant barrier to robust parameter estimation. [6] The results in Chapter 3 confirm that k_3 parameter estimates are subject to high variability when derived from PET scans alone. This thesis demonstrates that robust and accurate measurements of the k_3 parameter can be obtained with PET-CTP imaging by imputing functional parameters from CTP as a priori parameters in the PET compartment model.

5.4 Hybrid PET-CTP Imaging for Prostate Cancer

Previous clinical studies of ^{18}F -FCH PET for the detection of PCa have shown disappointing results when using the SUV. [7-12] Specifically, the SUV has generally shown poor contrast between malignant and benign prostate tissue. This thesis confirms that the SUV from ^{18}F -FCH PET is not correlated with PC-3 tumor volume in mice and that there is generally poor contrast both for features within the tumor as well as in surrounding tissue. Hybrid PET-CTP imaging may be useful for detecting dominant prostatic lesions in patients by providing a more accurate measure of the choline kinase activity. Further study is warranted to determine the sensitivity and specificity of this

technique. Specifically, the use of the $k_{3\max}$ parameter may be useful for assisting targeting for TRUS-guided biopsy and radiation dose escalation, as evidenced by the significant correlation with tumor volume that was observed.

5.5 Future Work

This thesis serves as a foundation for future investigations of hybrid PET-CT imaging. The following sections outline potential research avenues and novel hypotheses that have been generated by this work.

5.5.1 Mean Transit Time in Compartment Models

Chapter 4 examined the use of two different model solutions: the LIN-K1 model solution incorporates the K_1 parameter calculated from CTP blood flow and permeability maps, while the LIN-K1k2 also incorporates the k_2 parameter calculated using blood flow, permeability and extravascular volume functional maps. In Chapter 3, it was found that the LIN-K1k2 solution produced the k_3 estimate with lower bias and variation compared to the solution that does not impute parameters from CT Perfusion. However, in Chapter 4, the LIN-K1k2 model could not produce a good fit to the tumor tissue curves. This was because the Johnson-Wilson model, used in CTP, accounts for the mean transit time (W) between the arterial and venous ends of the capillary bed, while the compartment model assumes instantaneous transfer across the capillary bed. These differences are evident in the impulse residue functions (IRF) for both models, where W causes a flat step in the initial phase of the Johnson-Wilson IRF. This difference causes the initial bolus phase of the PET tissue TAC to conform poorly to the one generated with CTP parameters. This is an interesting

finding because the assumption of instantaneous transfer is implicit in the compartment models described in the literature. This lack of delay could be accounted for by deriving a linearized solution of the 3-compartment model that accounts for the mean transit time W . Future investigations will examine the feasibility and usefulness of this implementation. This approach may require a brute force search over the W domain to determine the best fit, which would increase computation time and negate a portion of the speed benefit that was gained from the use of the linearized model solution.

5.5.2 Choline Kinase Expression in Prostate Cancer

Chapter 4 found that the binding rate constant k_3 is correlated with PC-3 human PCa tumor volume in mice. Conversely, the SUV was not correlated with tumor volume. This indicates that the transfer of choline from the interstitial space into cells is an important biomarker for the localisation of malignant PCa. The most likely mechanism for this uptake in cells is phosphorylation of choline via the choline kinase enzyme that is the first step toward the incorporation of phosphorylated choline into the cell membrane. [13]

Results of immunohistochemistry with a choline kinase α (ChK α) antibody did not correlate with the $k_{3\max}$ parameter in the three samples tested, however there was a geographical correlation between a region of high antibody expression and high k_3 on parametric maps located on the tumor rim. This finding suggests that elevated choline kinase activity may be isolated to certain regions of the tumor rim. It also suggests that mean comparisons of the entire tumour are not meaningful because of tumour heterogeneity. Future studies should focus on the correlation between the maximum k_3 and

the maximum histological staining intensity and determine whether there is a spatial correlation between the k_3 parameter and the ChK α activity in a larger sample of tumours.

In Chapter 4, a single fiducial needle was inserted into the tumour post-imaging in order to find the axial image slice that corresponded to the histology slice. The limitation to this approach is that the needle spans more than one axial image slice, hence it is difficult to find the axial slice of the k_3 maps that corresponds to the histology slice. In future studies, this limitation can be rectified by the insertion of a second needle at an angle that is oblique to the first one. Thus, the distance between the needle tracks in each axial slice would be unique, therefore this distance could be used to determine the precise axial location of the histological slice in the image space. An additional CT scan can be performed immediately following the CT Perfusion scan, with the needles inserted in the tumour, and this scan could be registered to the CT Perfusion study. This would allow the needles to be rendered in three dimensions on the k_3 maps, which would further assist selection of the histological slice that corresponds to the image slice.

5.5.3 Effect of *In Vivo* Signal to Noise Ratio on k_3

The accuracy and variability of the k_3 measurement with *in vivo* PET-CTP imaging is subject to the noise in the time activity curves (TAC). In Chapter 4, a 3x3 pixel box-filter was employed on the mouse PET images in order to improve the signal to noise ratio (SNR) of the individual voxel TAC's. Clinical PET scanners have poorer resolution (~5 mm) compared to small animal PET scanners (~1 mm) due to the larger crystal and bore size and the increased detection of scatter events resulting from the larger volume of the subject being imaged. Therefore, the use of a box filter on images from a clinical scanner will

result in a larger extent of spatial smoothing relative to animal studies, which will increase the minimum size of lesion that can be localized.

Future work will focus on determining the ideal combination of PET sampling interval length and image smoothing techniques to produce a reliable estimate of k_3 *in vivo* while preserving the ability to accurately detect dominant prostatic lesions. A covariance matrix analysis using realistic model parameters from *in vivo* PET studies can be performed to determine the PET sampling protocol that increases the precision of the k_3 estimate.

5.5.4 Correlation of k_3 from *In Vivo* PET-CTP with Histopathology

Patient studies are currently underway which aim to correlate functional imaging parameters from PET, CT Perfusion, and MR studies with co-registered histopathology of prostate specimens obtained via radical prostatectomy. After the prostate is removed, *ex-vivo* MR images are obtained and are registered to the histology slices using a deformable registration and the aid of fiducial markers [14]. The *ex-vivo* MR images serve as a reference for the registration of PET, CT Perfusion and MR images. The histology slides are Gleason graded and the label maps of the different grades can be superimposed on the registered *ex-vivo* MR, *in-vivo* MR, PET and CT Perfusion images so that geographical agreement between regions of malignancy and functional parameters can be assessed.

This registration pipeline offers the opportunity to investigate whether k_3 measurements from hybrid PET-CTP imaging offer a viable way to differentiate malignant from benign prostate tissue *in-vivo* and to examine the use of the $k_{3\max}$ parameter as a tool to improve the targeting accuracy of dominant prostatic lesions for the purposes of biopsy and radiation dose escalation.

5.5.5 Clinical Applications

Presently, the detection of dominant prostatic lesions is performed via Gleason scoring of pathological samples obtained from biopsy. However, prostate cancer is a multifocal disease characterized by the presence of smaller intra-prostatic lesions in addition to the dominant lesion. This thesis shows that functional and molecular imaging with ^{18}F -fluorocholine PET-CTP imaging may assist in the localization of dominant lesions by assessing multiple characteristics of the tumour microenvironment. Hybrid imaging allows for more accurate and precise estimates of individual compartmental model parameters, which may serve as markers of hypoxia, proliferative activity, and other surrogate markers of advanced disease. This information may assist in assessing multifocal prostate cancer, which would lead to more accurate stratification of patients into various risk groups. This would result in more aggressive treatments for patients that require them and would help spare patients with low-risk disease from undergoing invasive and ultimately unnecessary procedures.

The potential applications of the hybrid PET-CTP imaging technique are not limited to ^{18}F -FCH PET imaging of PCa, but indeed any quantitative radiopharmaceutical PET study where the binding rate constant k_3 from the 3-compartment model would be of interest. This opens the door to a plethora of potential applications of hybrid PET-CTP imaging with the use of linearized solutions of the 3-compartment model. In addition, the technique has the potential to improve upon applications where previous results have shown that the SUV has little diagnostic value.

5.6 References

1. Slaets, D. and F. De Vos, *Comparison between kinetic modelling and graphical analysis for the quantification of [18F]fluoromethylcholine uptake in mice*. EJNMMI Res, 2013. **3**(1): p. 66.
2. Kristian, A., et al., *Positron emission tomography and pharmacokinetics of 2-[18F]-fluoroethyl choline for metabolic studies in breast cancer xenografts*. Acta Oncol, 2014. **53**(8): p. 1086-92.
3. Sutinen, E., et al., *Kinetics of [(11)C]choline uptake in prostate cancer: a PET study*. Eur J Nucl Med Mol Imaging, 2004. **31**(3): p. 317-24.
4. Seamonds, B., et al., *Evaluation of prostate-specific antigen and prostatic acid phosphatase as prostate cancer markers*. Urology, 1986. **28**(6): p. 472-9.
5. Taira, A., et al., *Reviving the acid phosphatase test for prostate cancer*. Oncology (Williston Park), 2007. **21**(8): p. 1003-10.
6. Muzi, M., et al., *Kinetic analysis of 3'-deoxy-3'-18F-fluorothymidine in patients with gliomas*. J Nucl Med, 2006. **47**(10): p. 1612-21.
7. Beauregard, J.M., et al., *Pilot comparison of F-fluorocholine and F-fluorodeoxyglucose PET/CT with conventional imaging in prostate cancer*. Journal of medical imaging and radiation oncology, 2010. **54**(4): p. 325-332.
8. Husarik, D.B., et al., *Evaluation of [(18)F]-choline PET/CT for staging and restaging of prostate cancer*. Eur J Nucl Med Mol Imaging, 2008. **35**(2): p. 253-63.
9. Heinisch, M., et al., *Positron emission tomography/computed tomography with F-18-fluorocholine for restaging of prostate cancer patients: meaningful at PSA < 5 ng/ml?* Mol Imaging Biol, 2006. **8**(1): p. 43-8.
10. Schmid, D.T., et al., *Fluorocholine PET/CT in Patients with Prostate Cancer: Initial Experience*. Radiology, 2005. **235**(2): p. 623-628.
11. Igerc, I., et al., *The value of 18F-Choline PET/CT in patients with elevated PSA-level and negative prostate needle biopsy for localisation of prostate cancer*.

- European Journal of Nuclear Medicine & Molecular Imaging, 2008. **35**(5): p. 976-983.
12. Cimitan, M., et al., *[18F]fluorocholine PET/CT imaging for the detection of recurrent prostate cancer at PSA relapse: experience in 100 consecutive patients*. Eur J Nucl Med Mol Imaging, 2006. **33**(12): p. 1387-98.
 13. Gibellini, F. and T.K. Smith, *The Kennedy pathway--De novo synthesis of phosphatidylethanolamine and phosphatidylcholine*. IUBMB Life, 2010. **62**(6): p. 414-28.
 14. Gibson, E., et al., *Registration of prostate histology images to ex vivo MR images via strand-shaped fiducials*. Journal of Magnetic Resonance Imaging, 2012. **36**(6): p. 1402-1412.
 15. Baxter, L.T. and R.K. Jain, *Transport of fluid and macromolecules in tumors. I. Role of interstitial pressure and convection*. Microvasc Res, 1989. **37**(1): p. 77-104.

Appendix A: Coefficients in the 3-Compartment Model

$$\alpha = \frac{k_2 + k_3 + k_4 + \sqrt{(k_2 + k_3 + k_4)^2 - 4k_2k_4}}{2}$$

$$\beta = \frac{k_2 + k_3 + k_4 - \sqrt{(k_2 + k_3 + k_4)^2 - 4k_2k_4}}{2}$$

$$G = K_1 \frac{(k_3 + k_4 - \alpha)}{(\beta - \alpha)}$$

$$H = K_1 \frac{(\beta - k_3 - k_4)}{(\beta - \alpha)}$$

Appendix B: Partial Derivatives of $Q(t)$

The partial derivatives of the tissue time activity curve $Q(t)$ with respect to the parameters of the 3-Compartment model are:

$$\frac{\delta Q(t)}{\delta V_b} = C_a(t)$$

$$\frac{\delta Q(t)}{\delta K_1} = \left[\frac{k_3 + k_4 - \alpha}{\beta - \alpha} \right] C_a(t) * e^{-\alpha t} + \left[\frac{\beta - k_3 - k_4}{\beta - \alpha} \right] C_a(t) * e^{-\beta t}$$

$$\begin{aligned} \frac{\delta Q(t)}{\delta k_2} &= \frac{\delta G}{\delta k_2} [C_a(t) * e^{-\alpha t}] - G \left[C_a(t) * \frac{\delta \alpha}{\delta k_2} t e^{-\alpha t} \right] \\ &\quad + \frac{\delta H}{\delta k_2} [C_a(t) * e^{-\beta t}] - H \left[C_a(t) * \frac{\delta \beta}{\delta k_2} t e^{-\beta t} \right] \end{aligned}$$

$$\begin{aligned} \frac{\delta Q(t)}{\delta k_3} &= \frac{\delta G}{\delta k_3} [C_a(t) * e^{-\alpha t}] - G \left[C_a(t) * \frac{\delta \alpha}{\delta k_3} t e^{-\alpha t} \right] \\ &\quad + \frac{\delta H}{\delta k_3} [C_a(t) * e^{-\beta t}] - H \left[C_a(t) * \frac{\delta \beta}{\delta k_3} t e^{-\beta t} \right] \end{aligned}$$

$$\begin{aligned} \frac{\delta Q(t)}{\delta k_4} &= \frac{\delta G}{\delta k_4} [C_a(t) * e^{-\alpha t}] - G \left[C_a(t) * \frac{\delta \alpha}{\delta k_4} t e^{-\alpha t} \right] \\ &\quad + \frac{\delta H}{\delta k_4} [C_a(t) * e^{-\beta t}] - H \left[C_a(t) * \frac{\delta \beta}{\delta k_4} t e^{-\beta t} \right] \end{aligned}$$

Where $*$ denotes the convolution operator and where

$$\frac{\delta G}{\delta k_2} = K_1 \left[\frac{-\frac{\delta \alpha}{\delta k_2} (\beta - \alpha) - (k_3 + k_4 - \alpha) \left(\frac{\delta \beta}{\delta k_2} - \frac{\delta \alpha}{\delta k_2} \right)}{(\beta - \alpha)^2} \right]$$

$$\frac{\delta H}{\delta k_2} = K_1 \left[\frac{-\frac{\delta \beta}{\delta k_2}(\beta - \alpha) - (\beta - k_3 - k_4) \left(\frac{\delta \beta}{\delta k_2} - \frac{\delta \alpha}{\delta k_2} \right)}{(\beta - \alpha)^2} \right]$$

$$\frac{\delta \alpha}{\delta k_2} = \frac{1}{2} \left[1 - \frac{k_2 + k_3 - k_4}{\sqrt{(k_2 + k_3 + k_4)^2 - 4k_2k_4}} \right]$$

$$\frac{\delta \beta}{\delta k_2} = \frac{1}{2} \left[1 + \frac{k_2 + k_3 - k_4}{\sqrt{(k_2 + k_3 + k_4)^2 - 4k_2k_4}} \right]$$

$$\frac{\delta G}{\delta k_3} = K_1 \left[\frac{\left(1 - \frac{\delta \alpha}{\delta k_3} \right) (\beta - \alpha) - (k_3 + k_4 - \alpha) \left(\frac{\delta \beta}{\delta k_3} - \frac{\delta \alpha}{\delta k_3} \right)}{(\beta - \alpha)^2} \right]$$

$$\frac{\delta H}{\delta k_3} = K_1 \left[\frac{\left(\frac{\delta \beta}{\delta k_3} - 1 \right) (\beta - \alpha) - (\beta - k_3 - k_4) \left(\frac{\delta \beta}{\delta k_3} - \frac{\delta \alpha}{\delta k_3} \right)}{(\beta - \alpha)^2} \right]$$

$$\frac{\delta \alpha}{\delta k_3} = \frac{1}{2} \left[1 - \frac{k_2 + k_3 + k_4}{\sqrt{(k_2 + k_3 + k_4)^2 - 4k_2k_4}} \right]$$

$$\frac{\delta \beta}{\delta k_3} = \frac{1}{2} \left[1 + \frac{k_2 + k_3 + k_4}{\sqrt{(k_2 + k_3 + k_4)^2 - 4k_2k_4}} \right]$$

$$\frac{\delta G}{\delta k_4} = K_1 \left[\frac{\left(1 - \frac{\delta \alpha}{\delta k_4} \right) (\beta - \alpha) - (k_3 + k_4 - \alpha) \left(\frac{\delta \beta}{\delta k_4} - \frac{\delta \alpha}{\delta k_4} \right)}{(\beta - \alpha)^2} \right]$$

$$\frac{\delta H}{\delta k_4} = K_1 \left[\frac{\left(\frac{\delta \beta}{\delta k_4} - 1 \right) (\beta - \alpha) - (\beta - k_3 - k_4) \left(\frac{\delta \beta}{\delta k_4} - \frac{\delta \alpha}{\delta k_4} \right)}{(\beta - \alpha)^2} \right]$$

$$\frac{\delta \alpha}{\delta k_4} = \frac{1}{2} \left[1 - \frac{-k_2 + k_3 + k_4}{\sqrt{(k_2 + k_3 + k_4)^2 - 4k_2k_4}} \right]$$

$$\frac{\delta\beta}{\delta k_4} = \frac{1}{2} \left[1 + \frac{-k_2 + k_3 + k_4}{\sqrt{(k_2 + k_3 + k_4)^2 - 4k_2k_4}} \right]$$

Appendix C: Animal Ethics Approval for the work contained in Chapter 4 entitled “A quantitative hybrid PET-CT Perfusion technique for measuring the binding rate constant of ^{18}F -Fluorocholine in a mouse model of prostate cancer”

From: eSiriusWebServer [mailto:
Sent: December 4, 2013 3:27 PM
To:
Cc:
Subject: eSirius Notification - New Protocol Modification Has Been APPROVED2009-013::5



AUP Number: 2009-013
PI Name: Lee, Ting Y
AUP Title: Monitoring tumor growth of PC-3 Human Prostate Cancer cells in a Nude Mice Model with Computed tomography and small animal PET Imaging.

Official Notification of AUS Approval: A MODIFICATION to Animal Use Protocol 2009-013 has been approved.

The holder of this Animal Use Protocol is responsible to ensure that all associated safety components (biosafety, radiation safety, general laboratory safety) comply with institutional safety standards and have received all necessary approvals. Please consult directly with your institutional safety officers.

Submitted by: Kinchlea, Will D
on behalf of the Animal Use Subcommittee

Appendix D: Copyright Agreements

Adam Richard Blais, Ting-Yim Lee, "Simulating the effect of venous dispersion on distribution volume measurements from the Logan plot," Biomedical Physics and Engineering Express, 1(4), 2015.

(http://iopublishing.org/wp-content/uploads/2016/01/Author_Rights.pdf)

AUTHOR RIGHTS

Named Authors of subscription access Articles who submitted an Assignment of copyright and publication agreement (the Agreement) linking to this document after 1st June 2014 are granted, in addition to those rights set out in the Agreement, the following additional rights:

- The right to include the Accepted Manuscript on their personal website, immediately upon publication.
- Following the Embargo Period, the right to include the Accepted Manuscript, accompanied by a statement of provenance, on the website of their institution or employer.
- Following the Embargo Period, the right to include the Accepted Manuscript, accompanied by a statement of provenance, on non-commercial third party websites but not on the websites of other publishers.

Copyright agreement for Figure 1.1:

Dear Adam,

Thank you for contacting me about using a Canadian Cancer Society graphic and for noting that you will include a citation. We request that the citation includes citing the full name of the Canadian Cancer Society, the title and URL of the web page, and the date on which the information was captured. (Read more: <http://www.cancer.ca/en/about-our-site/terms-and-conditions/?region=on#ixzz2z9gfpnEy>)

The order of the elements included doesn't really matter – you can present them according to the style that you follow as long as all elements are included.

If you need the graphic in a dpi format suitable for print, please contact Jaime Erz (cc'd above).

Please don't hesitate to come back to me with any questions.

Best regards



Jennifer Moorcroft

Editor, Information

Canadian Cancer Society, National Office

Copyright agreement for Figure 1.2 :**NATURE PUBLISHING GROUP LICENSE
TERMS AND CONDITIONS**

May 18, 2016

This is a License Agreement between Adam Blais ("You") and Nature Publishing Group ("Nature Publishing Group") provided by Copyright Clearance Center ("CCC"). The license consists of your order details, the terms and conditions provided by Nature Publishing Group, and the payment terms and conditions.

All payments must be made in full to CCC. For payment instructions, please see information listed at the bottom of this form.

License Number	3872061029556
License date	May 18, 2016
Licensed content publisher	Nature Publishing Group
Licensed content publication	Modern Pathology
Licensed content title	Gleason grading and prognostic factors in carcinoma of the prostate
Licensed content author	Peter A Humphrey
Licensed content date	Feb 13, 2004
Volume number	17
Issue number	3
Type of Use	reuse in a dissertation / thesis
Requestor type	academic/educational
Format	print and electronic
Portion	figures/tables/illustrations
Number of figures/tables/illustrations	1

High-res required	no
Figures	Figure 1
Author of this NPG article	no
Your reference number	None
Title of your thesis / dissertation	Quantitative PET-CT Perfusion imaging of prostate cancer
Expected completion date	Jun 2016
Estimated size (number of pages)	170
Total	0.00 CAD

Terms and Conditions

Terms and Conditions for Permissions

Nature Publishing Group hereby grants you a non-exclusive license to reproduce this material for this purpose, and for no other use, subject to the conditions below:

1. NPG warrants that it has, to the best of its knowledge, the rights to license reuse of this material. However, you should ensure that the material you are requesting is original to Nature Publishing Group and does not carry the copyright of another entity (as credited in the published version). If the credit line on any part of the material you have requested indicates that it was reprinted or adapted by NPG with permission from another source, then you should also seek permission from that source to reuse the material.
2. Permission granted free of charge for material in print is also usually granted for any electronic version of that work, provided that the material is incidental to the work as a whole and that the electronic version is essentially equivalent to, or substitutes for, the print version. Where print permission has been granted for a fee, separate permission must be obtained for any additional, electronic re-use (unless, as in the case of a full paper, this has already been accounted for during your initial request in the calculation of a print run). NB: In all cases, web-based use of full-text articles must be authorized separately through the 'Use on a Web Site' option when requesting permission.
3. Permission granted for a first edition does not apply to second and subsequent editions and for editions in other languages (except for signatories to the STM Permissions Guidelines, or where the first edition permission was granted for free).
4. Nature Publishing Group's permission must be acknowledged next to the figure, table or abstract in print. In electronic form, this acknowledgement must be visible at the same time as the figure/table/abstract, and must be hyperlinked to the journal's homepage.

5. The credit line should read:
 Reprinted by permission from Macmillan Publishers Ltd: [JOURNAL NAME] (reference citation), copyright (year of publication)
 For AOP papers, the credit line should read:
 Reprinted by permission from Macmillan Publishers Ltd: [JOURNAL NAME], advance online publication, day month year (doi: 10.1038/sj.[JOURNAL ACRONYM].XXXXX)

Note: For republication from the *British Journal of Cancer*, the following credit lines apply.

Reprinted by permission from Macmillan Publishers Ltd on behalf of Cancer Research UK: [JOURNAL NAME] (reference citation), copyright (year of publication)
 For AOP papers, the credit line should read:
 Reprinted by permission from Macmillan Publishers Ltd on behalf of Cancer Research UK: [JOURNAL NAME], advance online publication, day month year (doi: 10.1038/sj.[JOURNAL ACRONYM].XXXXX)

6. Adaptations of single figures do not require NPG approval. However, the adaptation should be credited as follows:

Adapted by permission from Macmillan Publishers Ltd: [JOURNAL NAME] (reference citation), copyright (year of publication)

Note: For adaptation from the *British Journal of Cancer*, the following credit line applies.

Adapted by permission from Macmillan Publishers Ltd on behalf of Cancer Research UK: [JOURNAL NAME] (reference citation), copyright (year of publication)

7. Translations of 401 words up to a whole article require NPG approval. Please visit <http://www.macmillanmedicalcommunications.com> for more information. Translations of up to a 400 words do not require NPG approval. The translation should be credited as follows:

Translated by permission from Macmillan Publishers Ltd: [JOURNAL NAME] (reference citation), copyright (year of publication).

Note: For translation from the *British Journal of Cancer*, the following credit line applies.

Translated by permission from Macmillan Publishers Ltd on behalf of Cancer Research UK: [JOURNAL NAME] (reference citation), copyright (year of publication)

We are certain that all parties will benefit from this agreement and wish you the best in the use of this material. Thank you.

Copyright agreement for Figure 1.6:

Dear Adam Blais,

Thank you for your request to reproduce IOP Publishing material in your thesis.

Regarding:

Figure 8 (Phys. Med. Biol. 50 (2005) 2209–2224)

We are happy to grant permission for the use you request on the terms set out below.

Conditions

Non-exclusive, non-transferrable, revocable, worldwide, permission to use the material in print and electronic form will be granted **subject to the following conditions:**

- Permission will be cancelled without notice if you fail to fulfil any of the conditions of this letter.
- You will make reasonable efforts to contact the author(s) to seek consent for your intended use. Contacting one author acting expressly as authorised agent for their co-authors is acceptable.
- You will reproduce the following prominently alongside the material:
 - the source of the material, including author, article title, title of journal, volume number, issue number (if relevant), page range (or first page if this is the only information available) and date of first publication. This information can be contained in a footnote or reference note; or
 - a link back to the article (via DOI); and
 - if practical and IN ALL CASES for works published under any of the Creative Commons licences the words "© Institute of Physics and Engineering in Medicine. Reproduced by permission of IOP Publishing. All rights reserved."
- The material will not, without the express permission of the author(s), be used in any way which, in the opinion of IOP Publishing, could distort or alter the author(s)' original intention(s) and meaning, be prejudicial to the honour or reputation of the author(s) and/or imply endorsement by the author(s) and/or IOP Publishing.
- Payment of £0 is received in full by IOP Publishing prior to use.

This permission does not apply to any material/figure which is credited to another source in our publication or has been obtained from a third party. Express permission for such materials/figures must be obtained from the copyright owner.

If you have any questions, please feel free to contact our Permissions team at

I should be grateful if you would acknowledge receipt of this email.

Kind regards,

Kathryn Shaw

Copyright & Permissions Team

Gemma Alaway – Rights & Permissions Adviser
Kathryn Shaw - Editorial Assistant

Contact Details

E-mail:

For further information:

Please note: We do not provide signed permission forms as a separate attachment. Please print this email and provide it to your publisher as proof of permission.

Curriculum Vitae

CONTINUING EDUCATION

- 2010 – 2016** *Ph.D. in Medical Biophysics (CAMPEP Accredited Radiation Therapy Stream)*
Western University, London, ON, Canada
- Thesis title: Quantitative Positron Emission Tomography and Dynamic Contrast-Enhanced Computed Tomography for the Detection of Prostate Cancer
 - Supervisor: Dr. Ting-Yim Lee

EDUCATION

- 2008 – 2010** *M.Sc. in Physics*
Laurentian University, Sudbury, ON, Canada
- Thesis title: Static and Rotational IMRT Treatment Plans for the Prostate: A Dosimetric and Risk Comparison Study
 - Supervisor: Dr. Konrad Leszczynski
- 2004 – 2008** *B.Sc. (Honours) in Applied Physics*
Laurentian University, Sudbury, ON, Canada
- Undergraduate thesis title: Design and Construction of a Phantom for Quality Control and Calibration of a Dual-Energy X-Ray Absorptiometry Imaging System

PUBLICATIONS

Adam Richard Blais, Ting-Yim Lee, "Simulating the effect of venous dispersion on distribution volume measurements from the Logan plot," *Biomedical Physics and Engineering Express*, 1(4), 2015.

Adam Richard Blais, Ernst Lederer, Michael Oliver, Konrad Leszczynski, "Static and Rotational Step-and-Shoot IMRT Treatment Plans for the Prostate: A Risk Comparison Study," *Medical Physics*, **39** (2), 1069-1078 (2012).

CONFERENCE AWARDS

- Mar, 2015** *2nd Place Poster Award – OICR Smarter Imaging Program Consortium 13th Imaging Network Ontario Symposium*
London, ON, Canada
 Title: Quantitative Functional Imaging of Prostate Cancer with Improved Kinetics Modeling of Hybrid ¹⁸F-Fluorocholine PET-CT Imaging

- Nov, 2014** ***Best Poster Award***
7th Annual OICR/CIHR Prostate Cancer Imaging Workshop
 London, ON, Canada
 Title: Quantitative Functional Imaging with Hybrid PET-CT Scanning via Improved Kinetics Modeling: Application to ¹⁸F-Fluorocholine PET Imaging of Prostate Cancer
- July, 2014** ***Most Popular Poster on Twitter***
& COMP Student Council Travel Award
Canadian Organization of Medical Physicists, 60th Annual Scientific Meeting
 Banff, AB, Canada
 Title: Linearization of Compartmental Models for Robust Estimates of Regional Hemodynamic, Metabolic and Functional Parameters using DCE-CT/PET Imaging
- May, 2014** ***Travel Award***
Institute of Circulatory and Respiratory Health - Young Investigator Forum
 Edmonton, AB, Canada
 Title: Venous Time Activity Curves are Suitable for Graphical Analysis of PET Studies with the Logan Plot
- Nov, 2013** ***Best Poster Award***
6th Annual OICR/CIHR Prostate Cancer Imaging Workshop
 London, ON, Canada
 Title: Simulating the Effect of Venous Dispersion on the Graphical Analysis of PET Studies

ACADEMIC AWARDS

- 2014** ***Ontario Graduate Scholarship***
 ➤ Department Nomination
- 2011 - 2014** ***Western Graduate Research Scholarship***
The University of Western Ontario, London, ON, Canada
- 2008 - 2009** ***Lloyd Reed Graduate Physics Research Award***
Laurentian University, Sudbury, ON, Canada
 ➤ In recognition of high academic standing in the Department of Physics
- 2004 – 2008** ***Vale Inco Reserved Scholarship Recipient***
 ➤ Four-year scholarship, awarded for overall proficiency in academics and extracurricular activities

2004 – 2005 *Laurentian University Entrance Scholarship*
Laurentian University, Sudbury, ON, Canada

CONFERENCE PROCEEDINGS

Adam Richard Blais, Mark Dekaban, Jennifer Hadway, Ting-Yim Lee, “Quantitative Functional Imaging with Hybrid PET-CT Via Improved Kinetics Modeling: Application to ^{18}F -Fluorocholine PET Imaging of Prostate Cancer,” *IFMBE Proceedings*, **51**, 154-157, (2015).

WORK EXPERIENCE

- | | |
|-------------------------|--|
| Jan-Apr
2014 | <i>Quality Assurance Technician</i>
London Regional Cancer Program, London, ON <ul style="list-style-type: none"> ➤ Responsible for weekly, bi-weekly, and monthly QA protocols for two Varian linear accelerators |
| May-Aug
2008 | <i>Research Assistant (Harold E. Johns Summer Studentship)</i>
Regional Cancer Program, Sudbury Regional Hospital, Sudbury, ON <ul style="list-style-type: none"> ➤ Investigated a new type of radiochromic film and its advantages and disadvantages compared with standard radiographic film ➤ Supervisor: Dr. Konrad Leszczynski |
| May-Aug
2007 | <i>Research Assistant</i>
Enriched Xenon Observatory for Neutrinoless Double Beta Decay, Sudbury, ON <ul style="list-style-type: none"> ➤ Conducted Monte Carlo simulations of a gas-phase Xenon detector for detection of neutrinoless double beta decay ➤ Supervisor: Dr. Jacques Farine |

RELEVANT TRAINING

- | | |
|-------------|--|
| 2015 | American Association of Physicists in Medicine online courses <ul style="list-style-type: none"> ➤ <i>Professionalism in Everyday Practice</i> |
|-------------|--|

VOLUNTEER WORK

- | | |
|-------------|--|
| 2015 | World Congress on Medical Physics and Biomedical Engineering
Toronto, ON, Canada. June 7-12, 2015. |
|-------------|--|

CONFERENCE PRESENTATIONS

Adam Blais, Mark Dekaban, Jennifer Hadway, Ting-Yim Lee, “Quantitative Hybrid DCE-CT Fluorocholine PET Imaging for the Localization of Prostate Cancer,” *CIHR Strategic*

Training Program: Oncology Research & Education Day, London, ON, Canada, June 26, 2015, **poster presentation**.

Adam Richard Blais, Mark Dekaban, Jennifer Hadway, Ting-Yim Lee, "Quantitative Functional Imaging with Hybrid PET-CT Via Improved Kinetics Modeling: Application to ^{18}F -Fluorocholine PET Imaging of Prostate Cancer," *World Congress of Medical Physics and Biomedical Engineering*, Toronto, ON, Canada, June 7-12, 2015, **oral presentation**.

Adam Blais, Mark Dekaban, Eli Gibson, Jennifer Hadway, Ting-Yim Lee, " Quantitative Functional Imaging of Prostate Cancer with Improved Kinetics Modeling of Hybrid ^{18}F -Fluorocholine PET-CT Imaging," *Imaging Network of Ontario 13th Annual Meeting*, London, ON, March, 2015, **oral & poster presentation (poster award)**.

Adam Blais, Mark Dekaban, Eli Gibson, Jennifer Hadway, Ting-Yim Lee, " Quantitative Functional Imaging with Hybrid PET-CT Scanning via Improved Kinetics Modeling: Application to ^{18}F -Fluorocholine PET Imaging of Prostate Cancer," *CIHR Team Grant & OICR Smarter Imaging Program (SIP) - Prostate Workshop*, London, ON, November 21, 2014, **poster presentation (poster award)**.

Adam Blais, Mark Dekaban, Eli Gibson, Jennifer Hadway, Ting-Yim Lee, "Linearization of Compartmental Models for More Robust Estimates of Regional Hemodynamic, Metabolic and Functional Parameters using DCE-CT/PET Imaging," *Canadian Organization of Medical Physicists, 60th Annual Scientific Meeting*, Banff, AB, July 9-12, 2014, **poster presentation (most popular poster on Twitter)**.

Adam Blais, Ting-Yim Lee, "Venous Time Activity Curves are Suitable for Graphical Analysis of PET Studies with the Logan Plot," *ICRH Young Investigator Forum*, Edmonton, AB, May 26-28, 2014, **poster presentation**.

Adam Blais, Ting-Yim Lee, "The Effect of Venous Dispersion on Distribution Volume Measurements with the Logan Plot," *Imaging Network of Ontario 12th Annual Meeting*, Toronto, ON, March, 2014, **poster presentation**.

Adam Blais, Ting-Yim Lee, "Simulating the Effect of Venous Dispersion on the Graphical Analysis of PET Studies," *CIHR Team Grant & OICR Smarter Imaging Program (SIP) - Prostate Workshop*, London, ON, November 15, 2013, **poster presentation (poster award)**.

Adam Richard Blais, Ting-Yim Lee, "Kinetic Modeling of ^{18}F -Fluorocholine PET of Prostate Cancer," *Canadian Organization of Medical Physicists, 58th Annual Scientific Meeting*, Halifax, NS, Canada, July 11-14, 2012, **oral presentation**.

Adam Richard Blais, Ting-Yim Lee, "Feasibility of Estimating Choline Kinase Activity Using Kinetic Modeling of ^{18}F -Fluorocholine PET for Prostate Cancer," *London Imaging Discovery Forum*, July 27, 2012, London, ON, Canada **poster presentation**.

Adam Richard Blais, Ting-Yim Lee, "Feasibility of Estimating Choline Kinase Activity Using Kinetic Modeling of ^{18}F -Fluorocholine PET for Prostate Cancer," *Oncology Research and Education Day*, July 22, 2012, London, ON, Canada, **poster presentation**.

Adam Richard Blais, Ting-Yim Lee, "Feasibility of Estimating Choline Kinase Activity with Kinetic Modeling of DCE-CT and ^{18}F -Fluorocholine PET Imaging of Prostate Cancer," *Imaging Network of Ontario 10th Annual Meeting*, February 13-14, 2012, Toronto, ON, Canada **oral presentation**.

Adam Blais, Konrad Leszczynski, Ernst Lederer. "A Dosimetric and Risk Comparison Study of Static and Rotational IMRT Treatment Plans for the Prostate," *Canadian Organization of Medical Physicists, 56th Annual Scientific Meeting*, Ottawa, ON, Canada, June 16-19, 2010, **poster presentation**.

Adam Blais, Jacques Farine, "Monte Carlo Simulations of a Gas Phase Xenon Detector for EXO," *Canadian Undergraduate Physics Conference, 43rd Annual Meeting*, Vancouver, BC, Canada, October 11-15, 2007, **oral presentation**.

TEACHING EXPERIENCE

2008 – 2010 *Graduate Teaching Assistant*

2006 – 2008 *Undergraduate Teaching Assistant*

Laurentian University, Sudbury, ON, Canada

- Corrected lab reports, assignments, midterms and exams for 1st year Introductory Physics and 2nd year Electricity and Electronics
- Supervised laboratory sessions for 1st year Introductory Physics and 2nd year Electricity and Electronics
- Taught 4 separate first year physics tutorials in both English and French

MISC. PRESENTATIONS

Adam Blais, Ting-Yim Lee, "2 Methods for Correcting Spillover and Partial Volume Effects in Image-Derived Input Curves for PET Imaging of Rodents," March 13, 2012, Western University, Journal Club presentation, Robarts Research Institute, Dr. Ting-Yim Lee's research group, oral presentation.

Adam Blais, Ting-Yim Lee, "Feasibility of Estimating Choline Kinase Activity with Kinetic Modeling of DCE-CT and ^{18}F -Fluorocholine PET Imaging of Prostate Cancer," February 2, 2012, Western University, London, ON, Medical Biophysics Graduate Seminar Series, oral presentation.

Joe H. Chang, *et. al.*, "Histopathological correlation of ^{11}C -choline PET scans for target volume definition in radical prostate radiotherapy," July 19th, 2011, Journal Club presentation, Robarts Research Institute, Dr. Ting-Yim Lee's research group, oral presentation.

Adam Blais, Ting-Yim Lee, "Simulation of kinetic modeling: an introduction and tutorial on JSim," May 10th, 2011, Journal Club presentation, Robarts Research Institute, Dr. Ting-Yim Lee's research group, oral presentation.

Adam Blais, Ting-Yim Lee, "¹⁸F-Fluorocholine Imaging of Prostate Cancer: Kinetic Modeling Considerations for PET," March 17th, 2011, The University of Western Ontario, London, ON, Medical Biophysics Graduate Seminar Series, oral presentation.

Mark Muzi, *et. al.*, "Kinetic Analysis of 3'-Deoxy-3'¹⁸F-Fluorothymidine in Patients with Gliomas," January 4th, 2011, Journal Club presentation, Robarts Research Institute, Dr. Ting-Yim Lee's research group, oral presentation.

Adam Blais, Konrad Leszczynski, Ernst Lederer, "An Approximation to Volumetric Modulated Arc Therapy Designed for a Siemens Primus Linear Accelerator," Regional Cancer Program, Sudbury Regional Hospital, Sudbury, ON, June 4, 2010, Medical Physics department oral presentation.

Adam Blais, "Magnetic Hysteresis," Laboratory presentation for 3rd year Advanced Laboratory undergraduate course, Laurentian University, Sudbury, ON, November 26, 2006.